Doctral Dissertation
Study of Neutrino Oscillation with the Off-Axis Neutrino Beam in T2K Experiment

Graduate School of Science
Kobe University

Takatomi Yano

July 2011

The Tokai-to-Kamioka (T2K) long baseline neutrino oscillation experiment has successfully started physics data taking at January 2010. Neutrinos corresponding to 1.431×10^{20} proton on target (POT) at J-PARC proton accelerator were delivered to Super-Kamiokande far detector at Kamioka during Jan. 2010 to Mar. 2011.

Near detector complex ND280 was newly assembled in a pit 280m far from neutrino target. We constructed the Side Muon Range Detector(SMRD), one of the ND280 during Mar.-July 2009. SMRD is commissioned with beam and cosmic runs, and joined to the T2K neutrino beam data taking. SMRD run during the beam run with 99% efficiency and showed a good performace as a neutrino monitor, which can measure the stability of beam intensity at $\pm$ 2%.

We also carried ν_μ disapperance analysis with these beam data. We acquired the ratio of data and MC as $R_{data/NEUTMC,reweighted} = 1.033 \pm 0.023(stat.)^{+0.044}_{-0.037}(det.sys.) \pm 0.038(phys.model)$ at ND280 with early 2010 beam data. Then we extrapolated the ratio to Super-Kamiokande where 31 ν_μ events were recorded during all beam period. Finally, we acquired the best fit point at ($\sin^2\theta$,Δm^2) = $(0.99, 2.6 \times 10^{-3}\mathrm{eV}^2)$. The probability of the null oscillation is order of 10^{-10}.

Contents

Chapter 1

Introduction

1.1 Neutrino

Neutrinos are elementary particles with neutral charge and spin 1/2. Neutrinos are classified to three kinds of lepton flavors, ν_e, ν_μ and ν_τ. Each of them are corresponds to charged leptons, e, μ and τ, respectively. Neutrinos interact through only the weak interaction.
Though neutrinos had been considered to be massless in the standard model of elemental particle physics, the evidence of their mass existence was found in neutrino oscillation. Direct mass measurements had been performed through the study of the end point of energy spectrum of β decay of Tritium, pion decay and tauon decay. But these measurements give only upper limit for these masses[1]. The current upper limits of neutrino masses are shown in Table 1.1.

Table. 1.1 Mass limit of neutrinos evaluated by Particle Data Group

Neutrino	Mass limit	Reference
ν_e	< 2 eV	^{3}H β decay, KRAUS,LOBASHEV
ν_μ	< 0.19 MeV (90%,C.L.)	π decay, ASSAMAGAN
ν_τ	< 18.2 MeV (95%,C.L.)	τ decay, BARATE

1.2 Neutrino Oscillation

Neutrino oscillation is a phenomenon that a kind of neutrino changes to others in the time evolution. The oscillation arises naturally from a neutrino mixing model, which describes the relation between three mass eigenstats and flavor eigenstats (eq. 1.1). The mixing is defined by a unitary 3×3 Maki-Nakagawa-Sakata (MNS) matrix[2] with three neutrino mixing angles (θ_{12}, θ_{23}, θ_{13}) and a complex phase (δ) as in the Cabibbo-Kobayashi-Maskawa matrix[3] (eq. 1.2).

In the neutrino mixing model, the flavor eigenstates $|\nu_\alpha\rangle$ ($\alpha = e, \mu, \tau$) are expressed by the superposition of the mass eigentates $|\nu_i\rangle$(i = 1, 2, 3) as follows.

$$|\nu_\alpha\rangle = \sum_i U_{\alpha i} |\nu_i\rangle \tag{1.1}$$

$U_{\alpha i}$ is a unitary mixing matrix. The MNS mixing matrix is expressed as follows.

$$\begin{aligned} U_{\alpha i} &= \begin{pmatrix} 1 & 0 & 0 \\ 0 & c_{23} & s_{23} \\ 0 & -s_{23} & c_{23} \end{pmatrix} \begin{pmatrix} c_{13} & 0 & s_{13}e^{-i\delta} \\ 0 & 1 & 0 \\ -s_{13}e^{i\delta} & 0 & c_{13} \end{pmatrix} \begin{pmatrix} c_{12} & s_{12} & 0 \\ -s_{12} & c_{12} & 0 \\ 0 & 0 & 1 \end{pmatrix} \\ &= \begin{pmatrix} c_{12}c_{13} & s_{12}c_{13} & s_{13}e^{-i\delta} \\ -s_{12}c_{23} - c_{12}s_{23}s_{13}e^{i\delta} & c_{12}c_{23} - s_{12}s_{23}s_{13}e^{i\delta} & s_{23}c_{13} \\ s_{12}c_{23} - c_{12}s_{23}s_{13}e^{i\delta} & -c_{12}s_{23} - s_{12}c_{23}s_{13}e^{i\delta} & c_{23}c_{13} \end{pmatrix} \end{aligned} \tag{1.2}$$

Here, s_{ij} and c_{ij} (i,j=1,2,3) express $\sin\theta_{ij}$ and $\cos\theta_{ij}$ respectively. θ_{ij} and δ are the mixing angle and the CP violation phase.

The mass eigenstate $|\nu_i\rangle$ with a finite mass m_i, momentum p and energy $E_i = \sqrt{p^2 + m_i^2}$ satisfies the following time evolution equation:

$$\begin{pmatrix} \nu_1(t) \\ \nu_2(t) \\ \nu_3(t) \end{pmatrix} = \begin{pmatrix} e^{-iE_1 t} & 0 & 0 \\ 0 & e^{-iE_2 t} & 0 \\ 0 & 0 & e^{-iE_3 t} \end{pmatrix} \begin{pmatrix} \nu_1(0) \\ \nu_2(0) \\ \nu_3(0) \end{pmatrix} \tag{1.3}$$

The states of $|\nu_i\rangle$ have common momentum p. Thus, the time evolution of the flavor eigenstate is written as:

$$\begin{pmatrix} \nu_e(t) \\ \nu_\mu(t) \\ \nu_\tau(t) \end{pmatrix} = U \begin{pmatrix} e^{-iE_1 t} & 0 & 0 \\ 0 & e^{-iE_2 t} & 0 \\ 0 & 0 & e^{-iE_3 t} \end{pmatrix} U^{-1} \begin{pmatrix} \nu_e(0) \\ \nu_\mu(0) \\ \nu_\tau(0) \end{pmatrix} \tag{1.4}$$

Using the relativistic approximation $E_i \simeq p + m_i^2/2p$, the oscillation probability after the flight of distance L can be calculated as :

$$\begin{aligned} P(\nu_\beta \to \nu_\alpha) &= |\langle \nu_\alpha(t) \,|\, \nu_\beta(0) \rangle|^2 \\ &= \delta_{\alpha\beta} - Re \sum_{j,k} U_{\alpha j} U^*_{\beta j} U^*_{\alpha k} U_{\beta k} \left\{ 1 - \exp\left(-i \frac{(m_j^2 - m_k^2) \cdot L}{2p} \right) \right\} \\ &= \delta_{\alpha\beta} - 4 \sum_{j<k} U_{\alpha j} U^*_{\beta j} U^*_{\alpha k} U_{\beta k} \sin^2 \left(\frac{\Delta m^2_{jk} L}{4p} \right) \end{aligned} \tag{1.5}$$

Here, $\Delta m^2_{ij} \equiv m_i^2 - m_j^2$. Note the speed of neutrino is assumed to be c. For most of neutrino experiments, the mass energy of neutrinos is negligible. So we can see the oscillation probability is expressed as a function of L/E, with $E \sim p$ approximation.

In the simplest case, where only two of the mass states dominate the oscillations, neutrino mixing, appearance and disappearance oscillation probability can be written as:

$$\begin{pmatrix} \nu_\alpha \\ \nu_\beta \end{pmatrix} = \begin{pmatrix} \cos\theta & \sin\theta \\ -\sin\theta & \cos\theta \end{pmatrix} \begin{pmatrix} \nu_1 \\ \nu_2 \end{pmatrix} \tag{1.6}$$

$$P(\nu_\beta \to \nu_\alpha) = \sin^2 2\theta \sin^2 \left(\frac{1.27 \times \Delta m^2 [eV^2] L[km]}{E_\nu [GeV]} \right) \tag{1.7}$$

$$P(\nu_\alpha \to \nu_\alpha) = 1 - \sin^2 2\theta \sin^2 \left(\frac{1.27 \times \Delta m^2 [eV^2] L[km]}{E_\nu [GeV]} \right) \tag{1.8}$$

In case of oscillation experiment like T2K (Tokai-to-Kamioka experiment, see Sec1.4), with L =hundreds km and E_ν =hundreds MeV to few GeV, two flavor oscillation probability function (eq.1.9) can describe ν_μ disappearance quite well.

$$P(\nu_\mu \to \nu_\tau) = \sin^2 2\theta_{23} \sin^2 \left(\frac{1.27 \times \Delta m^2_{23} [eV^2] L[km]}{E_\nu [GeV]} \right) \tag{1.9}$$

This is coming from ~ 100 times difference between Δm^2_{23} and Δm^2_{12}. Because of this difference, direct $\nu_\mu \to \nu_e$ oscillation can be considered as negligible for ν_μ disappearance.
For describing ν_e appearance, we have to write down the probability with full three flavors. In this

oscillation case, $\nu_\mu \to \nu_\tau \to \nu_e$ is most dominant:

$$\begin{aligned}
P(\nu_\mu \to \nu_e) &= 4c_{13}^2 s_{13}^2 s_{23}^2 \sin^2\left(\frac{\Delta m_{31}^2 L}{4E}\right) \times \left\{1 + \frac{2a}{\Delta m_{31}^2}(1-2s_{13}^2)\right\} \\
&+ 8c_{13}^2 s_{12}s_{13}s_{23}(c_{12}c_{23}\cos\delta - s_{12}s_{13}s_{23}) \cos\left(\frac{\Delta m_{32}^2 L}{4E}\right) \sin\left(\frac{\Delta m_{31}^2 L}{4E}\right) \sin\left(\frac{\Delta m_{21}^2 L}{4E}\right) \\
&- 8c_{13}^2 c_{12}c_{23}s_{12}s_{13}s_{23}\sin\delta \dot{\sin}\left(\frac{\Delta m_{32}^2 L}{4E}\right) \sin\left(\frac{\Delta m_{31}^2 L}{4E}\right) \sin\left(\frac{\Delta m_{21}^2 L}{4E}\right) \\
&+ 4s_{12}^2 c_{13}^2 (c_{12}^2 c_{23}^2 + s_{12}^2 s_{23}^2 s_{13}^2 - 2c_{12}c_{23}s_{12}s_{23}s_{13}\cos\delta) \sin^2\left(\frac{\Delta m_{21}^2 L}{4E}\right) \\
&+ 8c_{13}^2 s_{13}^2 s_{23}^2 (1-2s_{13}^2)\frac{aL}{4E} \cos\left(\frac{\Delta m_{32}^2 L}{4E}\right) \sin\left(\frac{\Delta m_{31}^2 L}{4E}\right)
\end{aligned} \tag{1.10}$$

Here, definition of s_{ij} and c_{ij} follows that of e.q. 1.2. a means the matter effect parameter. This equation can become somewhat simpler for T2K experiment:

$$\begin{aligned}
P(\nu_\mu \to \nu_e) &\approx \sin^2\theta_{23} \sin^2 2\theta_{13} \sin^2\left(\frac{\Delta m_{32}^2 L}{4E}\right) \\
&\pm \frac{\Delta m_{21}^2}{\Delta m_{31}^2} \sin 2\theta_{13} \sin\delta \cos\theta_{13} \sin 2\theta_{12} \sin 2\theta_{23} \sin^3\left(\frac{\Delta m_{32}^2 L}{4E}\right) \\
&- \frac{\Delta m_{21}^2}{\Delta m_{31}^2} \sin 2\theta_{13} \cos\delta \cos\theta_{13} \sin 2\theta_{12} \sin 2\theta_{23} \cos\left(\frac{\Delta m_{32}^2 L}{4E}\right) \sin 2\left(\frac{\Delta m_{32}^2 L}{4E}\right) \\
&+ \left(\frac{\Delta m_{21}^2}{\Delta m_{32}^2}\right)^2 \cos^2\theta_{23} \sin^2 2\theta_{12} \sin\left(\frac{\Delta m_{32}^2 L}{4E}\right)
\end{aligned} \tag{1.11}$$

Here, $\Delta m_{32}^2 = \Delta m_{31}^2 - \Delta m_{21}^2 \sim \Delta m_{31}^2$ is assumed. The matter effect parameter a is set to zero. The last term doesn't contain θ_{13}, but the term depends on $(\Delta m_{21}^2/\Delta m_{31}^2)^2$. Because of the mass ratio term, the last term is unobservable in T2K. The dominant term is the first term, $P(\nu_\mu \to \nu_e) \approx \sin^2\theta_{23}\sin^2 2\theta_{13}\sin^2\left(\frac{\Delta m_{31}^2 L}{4E}\right)$. Direct $\nu_\mu \to \nu_e$ oscillation is a background of the oscilltion signal in T2K.

1.3 Neutrino Oscillation Experiment

In this section, the neutrino oscillation experiments and the present knowledge about oscillation parameter measurements are summarized.

1.3.1 Solar neutrino experiment

The representative method of solar neutrino experiment is to measure electron neutrino flux and energy, which is produced by nuclear reaction in the sun. The energy range of solar neutrinos is ~ 100 keV to 15 MeV and distance between the sun and the earth is 1.5×10^8 km. Thus, the disappearance of ν_e is sensitive to θ_{12} and Δm_{12}^2 through $\nu_e \to \nu_\mu$ oscillation. Current limit of solar neutrino oscillation parameters are given by global analysis[15] with KamLAND[7], Homestake,[11], SAGE+GNO/GALLEX[12][13][14], Borexino[8], Super-Kamiokande-I[9] and SNO experiments[15] (fig. 1.1):

$$\begin{aligned}
\Delta m_{21}^2 &= 7.59^{+0.19}_{-0.21} \times 10^{-5}[eV^2], \\
\sin^2 2\theta_{12} &= 0.87 \pm 0.03\,(90\%, C.L.)
\end{aligned} \tag{1.12}$$

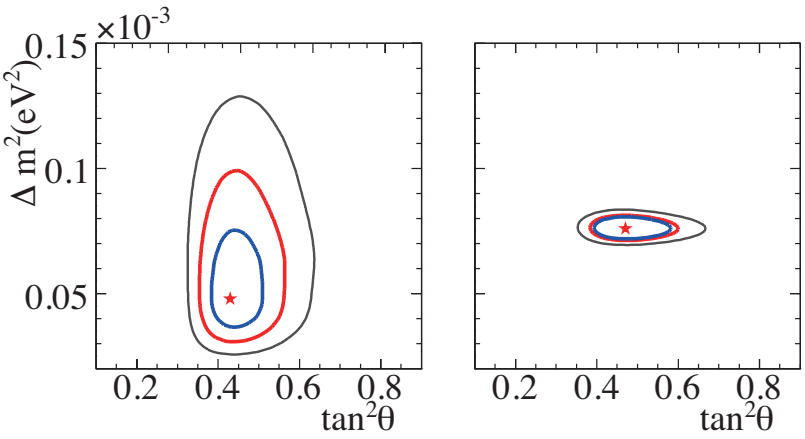

Fig. 1.1 68%, 95%, and 99.73% confidence level allowed parameter regions as well as the best-fit points are shown for (left) global solar neutrino data analysis and (right) global solar neutrino + KamLAND data analysis[15].

1.3.2 Atmospheric neutrino experiment

Atmospheric neutrinos consist of ν_μ and ν_e produced by decay of pions and kaons , which are generated from primary cosmic ray interaction in upper atmosphere. The energy of atmospheric neutrino has peak at $\sim$ 1GeV and extends to hundreds GeV. The length of neutrino flight varies $\sim$ 15 km to 13,000 km, corresponding to neutrinos generated in the atmosphere above the detector and in opposite atmosphere of the earth.
Atmospheric experiment measure the flux and energy of upper-going and under-going neutrinos. These quantities are sensitive to mainly $\nu_\mu \rightarrow \nu_\tau$ oscillation mode, which depends on θ_{23} and Δm^2_{23}. Current arrowed region of θ_{23} and Δm^2_{23} in atmosphere experiments are given by Super-Kamiokande[5][6].

$$1.9 \times 10^{-3} < \Delta\, m\,^2_{23} < 3.0 \times 10^{-3} [eV^2], \tag{1.13}$$

$$\sin^2 2\theta_{23} > 0.92\,(90\%, C.L.) \tag{1.14}$$

1.3.3 Reactor neutrino experiment

Reactor neutrinos consist of ν_e and $\bar{\nu}_e$, generated from nuclear fissions of ^{235}U, ^{238}U, ^{239}Pu and ^{241}Pu in nuclear reactors. The mean energy of reactor neutrino is $\sim$ 3MeV, and the detectors are placed at distance of $\sim$ 100 m to 1 km. $\nu_e \rightarrow \nu_\tau$ is dominant in $\sim$ 1 km baseline experiment and represents as disappearance of ν_e. This oscillation sector is sensitive to oscillation parameter Δm^2_{13} and θ_{13}. Current limit of θ_{13} is given by CHOOZ[16] experiment:

$$\sin^2 2\theta_{reactor} < 0.15\,(90\%, C.L.) \tag{1.15}$$

1.3.4 Accelerator neutrino experiment

Accelerator neutrinos are provided by the decay of pions, which are generated from the collision of beam protons and beam target. The main component of accelerator neutrino is ν_μ. The energy of neutrinos is optimized for the purpose of each experiments. In most case, near and far detectors are placed at

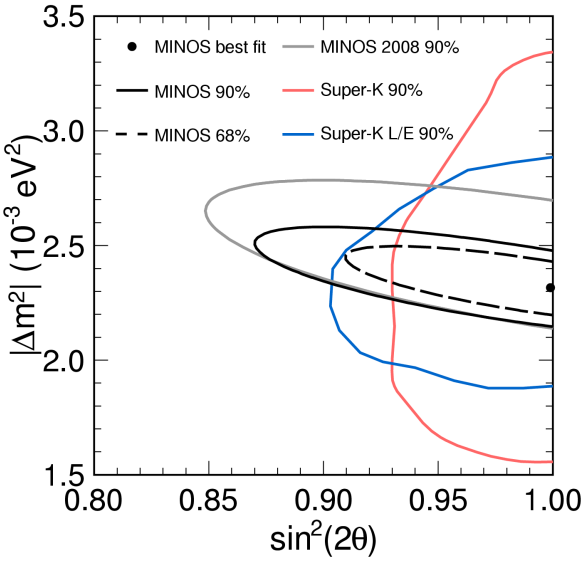

Fig. 1.2 Allowed region for the ν_μ to ν_τ oscillation parameters form the MINOS results published in 2011[18]. Super-K atmospheric allowed region is also shown.

a few hundreds meter and at hundreds km to measure the flux and energy distribution of neutrinos. These quantities are sensitive to $\nu_\mu \rightarrow \nu_\tau$ oscillation, which depends on θ_{23} and Δm^2_{23}.
MINOS experiment[18] uses neutrinos with the energy of ∼1-3 GeV and ∼ 735 km baseline for measurement of θ_{23} and Δm^2_{23}.
OPERA experiment, which was designed to detect the ν_τ appearance from ν_μ, uses neutrinos with the energy of ∼17 GeV and ∼ 732 km baseline. They observed the first ν_τ event successfully in 2010[19].
Arrowed region is given by MINOS experiment(Fig. 1.2):

$$|\Delta m^2_{23}| = 2.32^{+0.12}_{-0.08} \times 10^{-3}[eV^2] \tag{1.16}$$

$$\sin^2 2\theta_{23} > 0.90(90\%, \text{C.L.}) \tag{1.17}$$

1.4 T2K Long Baseline Neutrino Oscillation Experiment

From the first evidence of neutrino oscillation presented by Super-Kamiokande collaboration, several experiments have been proposed and carried out for measurement of neutrino oscillation parameters. Today, 2 mixing angles and 2 mass differences are already measured and their upper and lower limits are determined. Third mass difference Δm^2_{13} also can be assumed to be nearly equal to Δm^2_{23}, because of the relation $\Delta m^2_{12} \ll \Delta m^2_{23}$. Despite of these several efforts, only the upper limit is given for θ_{13}. The measurement of last mixing angle θ_{13}, and lepton CP violation phase δ_{CP} remain the highest demand on our neutrino physics.

T2K is a second generation long baseline neutrino oscillation experiment designed to probe the mixing of the muon neutrino with other species. The primal T2K's physics goal is the measurement of θ_{13} through the search for $\nu_\mu \rightarrow \nu_e$ appearance. The sensitivity of θ_{13} in T2K is a factor of about 20 higher compared to the current best limit on θ_{13} from the CHOOZ experiment, $\sin^2 2\theta_{13} > 0.006$. Here, $\Delta m^2_{23} = 2.4 \sim 2.6 \times 10^{-3}$eV and CP violating phase $\delta = 0$ is assumed, the statictics is $\sim 8 \times 10^{21}$ POT (protons on target) for proposed T2K 5 years. The another essential T2K's goal is the precision measurement of the $\nu_\mu \rightarrow \nu_\tau$ oscillation parameters through ν_μ disappearance. The precision of the

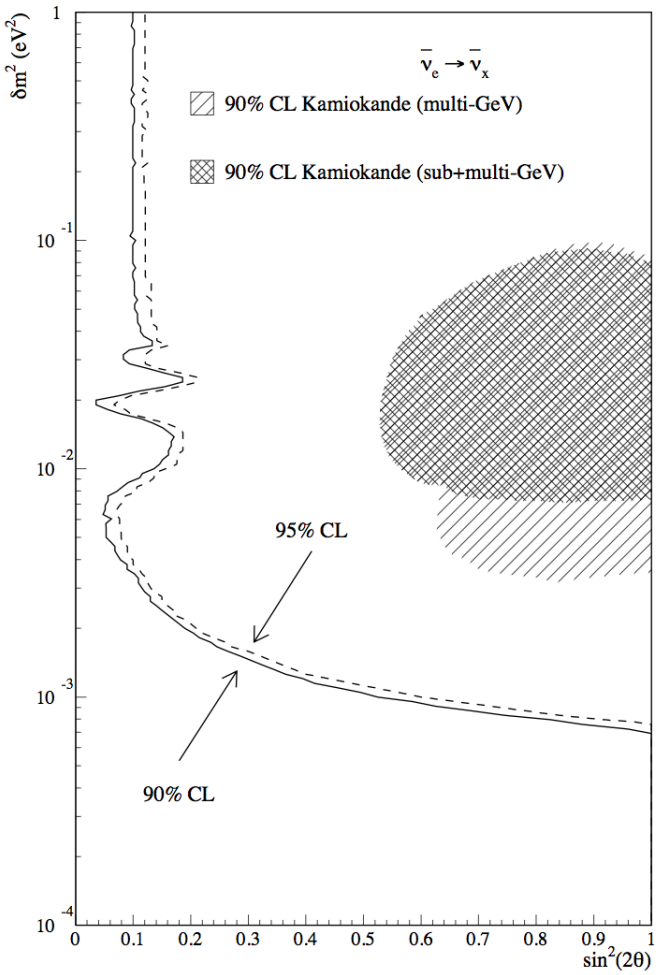

Fig. 1.3 CHOOZ exclusion plot for the oscillation parameters Δm^2_{13} and $\sin^2 2\theta_{13}$[16].

measurement is $\delta(\Delta m^2_{23}) \sim 10^{-4}\text{eV}^2$ and $\delta(\sin^2 2\theta_{23}) \sim 0.01$ with T2K 5 years data, $\sim 8 \times 10^{21}$ POT.

1.4.1 Off-Axis Beam

T2K is the world-first long baseline neutrino oscillation experiment with the key technology, Off-Axis beam method. The method enable us to gain the neutrinos at ~600 MeV, where ν_μ oscillation is maximum of T2K. At same time, we can reduce > 1GeV component of ν_μ beam, which is source of ν_e detection background at SK. Since the energy distribution and flux of the Off-Axis beam is strongly depends on its direction, we measure the direction and other characteristics of our beam continuously. (Details will be described at "Setup" chapter.)

1.4.2 The first result of T2K ν_e appearance

We, T2K group reported our first result of ν_e appearance at 2011 with 1.43×10^{20} POT beam data[20]. We found six ν_e candidate events in Super-K, where 1.5 ± 0.3 background events were predicted with $\sin^2 2\theta_{13} = 0$. We concluded a confidence interval, $0.03(0.04) < \sin^2 2\theta_{13} < 0.28(0.34)$ at 90% C.L. for $\sin^2 2\theta_{23} = 1.0$ for normal (inverted) neutrino mass hierarchy ($|\Delta m^2_{23}| = 2.4 \times 10^{-3}, \delta_{CP} = 0$ is assumed). The best fit points are 0.11(0.14) with same assumptions, respectively.

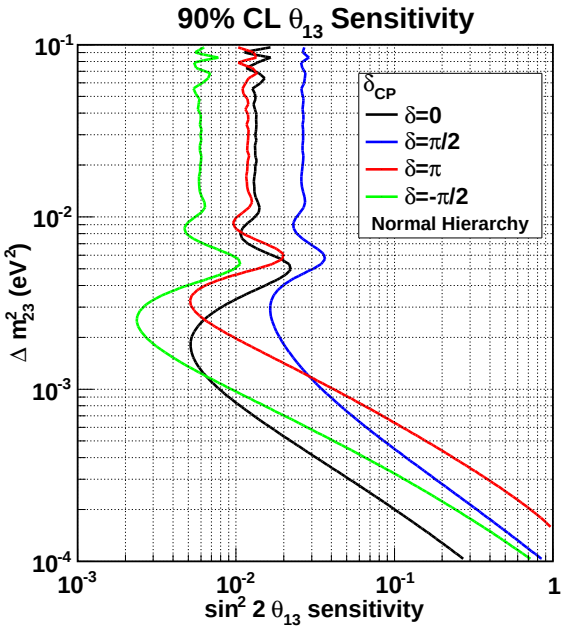

Fig. 1.4 T2K sensitivity to θ_{13} at the 90% confidence level as a function of Δm^2_{23}. Beam is assumed to be running at 750kW for 5 years, using the 22.5 kton fiducial volume SK detector. 5%, 10% and 20% systematic error fractions are plotted. The yellow region has already been excluded to 90% confidence level by the Chooz reactor experiment. The following oscillation parameters are assumed: $\sin^2 2\theta_{12} = 0.8704$, $\sin^2 2\theta_{23} = 1.0$, $\delta m^2_{12} = 7.6 \times 10^{-5}\mathrm{eV}^2$, $\delta_{CP} = 0$, normal hierarchy.

1.5 Motivation of this thesis

Side Muon Range Detector(SMRD), one of the our off-axis detector, is newly constructed for T2K experiment on the baseline to Super-Kamiokande. SMRD is most massive detector on the baseline and has a unique capability of continuous ν intensity measurement ν in the off-axis detectors. In this thesis, we report the continuous measurement result of Off-Axis beam stability during our beamrun at 2010 and 2011 with SMRD at first. Then, measurement of neutrino oscillation parameters, θ_{23} and Δm^2_{23} through ν_μ disappearance analysis is carried out using off-axis detectors and Super-Kamiokande, with T2K 1.43×10^{20} POT data during Jan. 2010 - Mar. 2011. Needless to say, the measurement of these parameters itself is valuable for the neutrino physics. In addition, these parameters appears in the first order of ν_e appearance probability formalization: $P(\nu_\mu \rightarrow \nu_e) = \sin^2\theta_{23} \sin^2 2\theta_{13} \sin\left(\Delta m^2_{23} L/E\right)$. So this analysis is also motivated by the sight of θ_{13} analysis in future. These neutrino mixing angles and mass difference cannot be predicted by the standard model. They are expected to give handholds for the incoming physics theories.

Chapter 2

Experimental Setup

2.1 Overview of T2K

T2K[21] is a second generation long baseline accelerator neutrino oscillation experiment for probing the neutrino oscillations, ν_e appearance ($\nu_\mu \rightarrow \nu_e$) and ν_μ disappearance ($\nu_\mu \rightarrow \nu_\tau$). T2K baseline is 295 km length between J-PARC accelerator facility at Tokai and Super-Kamiokande[22] far detector at Kamioka, similarly to the K2K experiment. The near detector ND280 is constructed at 280 m downstream from beam target at J-PARC, for measuring the characteristics of unoscillated neutrino beam. T2K will discover ν_e appearance by searching ν_e candidate events at Super-Kamiokande. The oscillation parameters $\sin^2 2\theta_{23}$ and Δm^2_{23} are also measured by analyzing ν_μ disappearance, a decrease of ν_μ flux and E_ν distortion between ND280 and Super-Kamiokande.
T2K neutrino beam line at J-PARC and the near detector ND280 is newly constructed. The energy distribution of T2K neutrino beam is optimized for ν_e appearance and ν_μ disappearance studies with Off-Axis beam method, which is firstly applied to neutrino experiment in the world. Super-Kamiokande was restored with new-photomultiplier tubes and upgraded with new DAQ system(Super-Kamiokande IV)(Fig. 2.1).

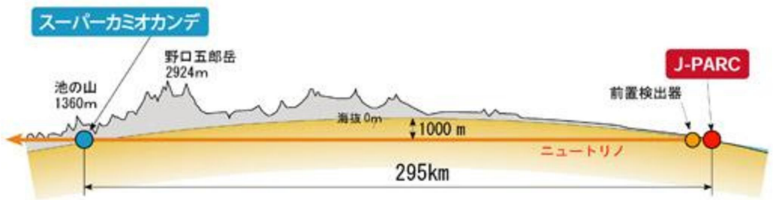

Fig. 2.1 A schematic figure of the T2K neutrino baseline, from the beamline at J-PARC through the near detectors and then 295 km underneath the main island of Japan to Super-Kamiokande.

2.2 Neutrino Beam Line

The T2K neutrino beam is generated using the new high intensity proton synchrotron at J-PARC. The neutrino beam are centered 2.5° off-axis respect to the Super-Kamiokande/J-PARC baseline direction, with the optimized peak neutrino energy at Super-Kamiokande[23]. Each component of the beam line is described in this section.

2.2.1 Off-Axis Beam

Recent results from the SK, K2K, and MINOS experiments point at $\Delta m^2_{23} = 2 \sim 3 \times 10^{-3}$ eV^2. At this parameter, the oscillation maximum is at around the neutrino energy of 500 $\sim$ 700 MeV at the SK; i.e.,

295 km away from the source. In addition, the high energy neutrinos ($\gtrsim$ 1GeV) do not only contribute to the measurement of the oscillation but become background sources for low energy neutrinos via the neutral current interaction or the inelastic scattering. As these physics condition prefers the high intensity narrow band low energy neutrino beam, we use the Off-Axis scheme as a solutions to meet the requirement.

In on-axis beam, the neutrino detector is placed on the same axis as the one to which proton beam, the target, the electromagnetic horn and the decay volume are aligned. In this case we get broad neutrino energy spectrum as is used in the K2K experiment. The detector is placed at a few degree (Off-Axis angle) off from the beam axis in the off-axis beam as shown in Fig. 2.2. The kinematics of pion decay for the on-axis and the off-axis beam is illustrated in Fig. 2.3.

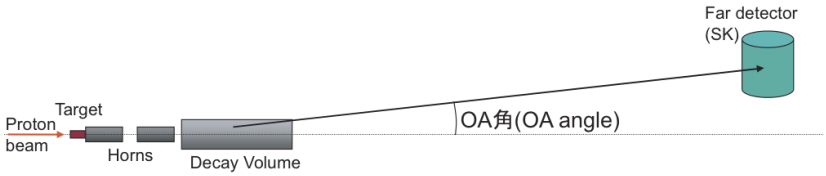

Fig. 2.2 Schematic of the Off-axis beam

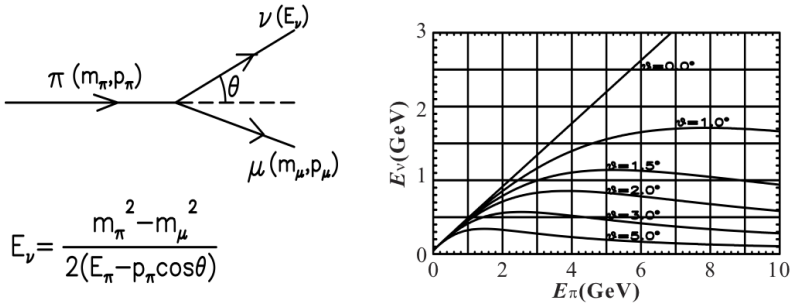

Fig. 2.3 Kinematics of the Off-axis beam

The neutrino energy is proportional to the energy of the parent π meson when the off-axis angle is 0 (wide band beam), while it is almost independent of the π meson energy with non-zero off-axis angle. Since pions in a wide momentum range contribute to narrow energy range of neutrino, a narrow intense neutrino beam is obtained.

Expected neutrino properties are estimated with the MC simulation in which the geometry of neutrino production equipments are coded. The expected number of total and CC interactions in 22.5 kton fiducial volume of SK is 2,300 events/yr and 1,700events/ys, respectively, at 2.5degree off-axis in the case of no oscillation with 30 GeV, 0.75 MW, 3000 hr/yr operation. Expected energy spectra at SK are plotted in Fig. 2.4. Peaks of the energy spectra are at 780 MeV and 600 MeV for 2 and 2.5 degree off-axis, respectively. Contamination of ν_e in the ν_μ beam is $\sim 0.4\%$ at the peak energy of ν_μ spectrum.

2.2.2 J-PARC 30GeV Proton Synchrotron

J-PARC (Japan Proton Accelerator Research Complex) consists of three accelerators [24]: a linear accelerator (LINAC), a rapid-cycling synchrotron (RCS) and a slow-cycling synchrotron (the main ring, or MR). An H^- beam is accelerated up to 400 MeV (181 MeV at present) by LINAC, and is converted to an H^+ beam by change-stripping foils at the RCS injection. The beam is accelerated up to 3 GeV by the RCS with a 25Hz cycle. The harmonic number of the RCS is two, and there are two bunched in a cycle. About 4-5% of these bunches are supplied to the MR. The rest of the bunches are supplied to the muon and neutron beamline in the Material and Life Science Facility. The proton beam injected

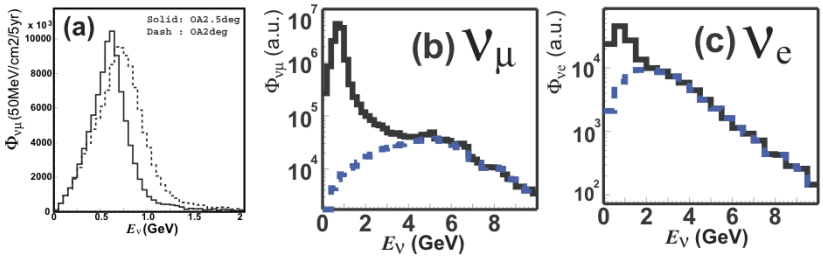

Fig. 2.4 Expected neutrino spectra. (a) Energy spectra of ν_μ fluxes for different off-axis angle with 30 GeV, 0.75 MW, 3,000 hr/yr oepration. (b) ν_μ flux. Solid is total and dashed line is contribution from Kaon decay. (c) ν_e flux. Solid and dashed lines are total and contribution from Kaon, respectively.

Table. 2.1 Design parameters of the fast extracted proton beam.

Beam power	750kW
Beam kinetic energy	30GeV
Beam intensity	3.3×10^{14} p/spill
Spill cycle	0.3 Hz
Number of bunches	8/spill
Bunch interval	581 ns
Bunch width	58 ns

to the MR is accelerated up the 30 GeV with 0.3Hz. The harmonic number of the MR is nine, and the number of bunches in the MR is eight (six until June 2010). There are two extraction points in the MR: slow extraction for the hadron beamline and fast extraction for the neutrino beamline.

Each spill consists of a number of proton bunches extracted from the MR to the T2K neutrino beamline, which produces the neutrino beam. The parameters of the extracted proton beam are listed in Tab.1.

The neutrino beam line is composed of two sections: the primary and secondary beamlines. In the primary beamline, the extracted proton beam is transported to point toward Super-K. In the secondary beam line, the proton beam impinges on a target to produce secondary pions, which are focused by magnetic horns and decay into neutrinos. An overviews of the neutrino beam line is shown in Fig. 2.5.

2.2.3 Primary Proton Beam Transport Line

The primary beam line consists of the preparation section (54m long), are section (147 m) and final focusing section (37 m). In the preparation section, the extracted proton beam is tunes with a series of 11 normal conducting magnets (four steering, two dipole and five quadrupole magnets) so that the beam can be accepted by the arc section. In the arc section, the beam is bent toward the direction of Super-K by 80.7 degrees, with a 104, radius of curvature, using 14 doublets of super-conduction combined function magnets (SCFMs)[25][26][27]. At intervals of SCFMs, three pair of horizontal and vertical superconducting steering magnets are installed to correct the beam orbit. In the final focusing section, ten normal conducting magnets (four steering, two dipole and four quadrupole magnets) guide and focus the beam on to the target, while directing the beam downward by 3.637 degrees. The beam duct, inside of the primary beam line, is kept at high vacuum using ion pumps. A well-tuned proton beam is essential for stable neutrino beam production, and to minimize beam loss in order to achieve high-power beam operation. Therefore, the intensity, position, profile and loss of the proton beam in the primary sections are precisely monitored by five current transformers(CTs),21 electrostatic monitors (ESMs), 19 segmented secondary emission monitors (SSEMs) and 50 beam loss monitors (BLMs), respectively.

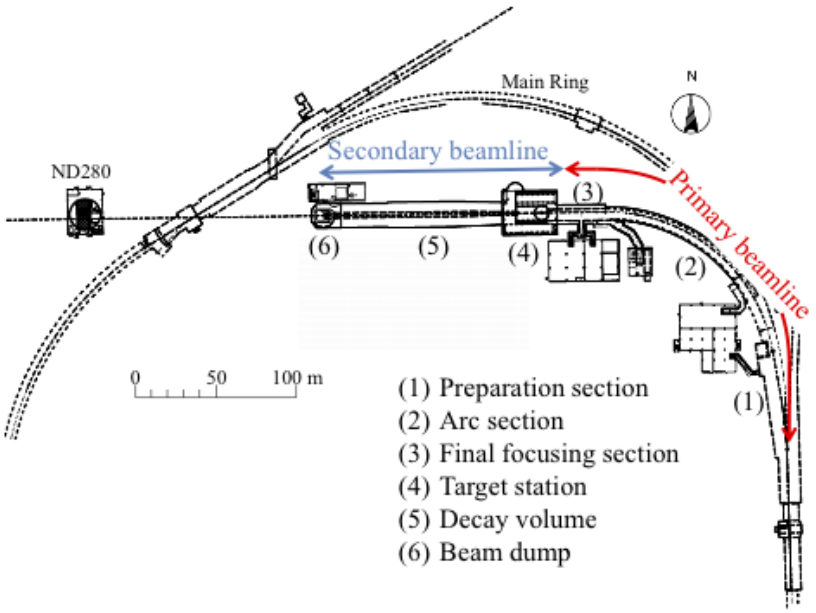

Fig. 2.5 Overview of the T2K neutrino beam line.

Photographs of the monitors are shown in Fig. 2.6, while the monitor locations are shown in Fig. 2.7. Polyimide cables and ceramic feedthroughs are used for the beam monitors, because of their radiation tolerance. The most downstream ESM and SSEM are installed in the 5 m tall monitor stack located in the 70 cm thick wall at the end of the primary beam line. Because of the high radiation levels, the monitor stack is equipped with a remote-handling system for the monitors.

2.2.3.1 Normal conducting magnet

The normal conducting magnets are designed to be tolerant of radiation and to be easy to maintain in the high radiation environment. For the four most upstream magnets in the preparation section, a mineral insulation coil is used for its radiation tolerance. To minimize workers' exposure to radiation, remote maintenance systems are installed such as twist lock slings, alignment dowel pins, and quick connectors for cooling pipes and power lines. For the quadrupole magnets, flower-shaped beam ducts whose surface is made in a shape of the magnetic pole surface is adopted to maximize their apertures.

2.2.3.2 Super conducting combined function magnet (SCFM)

There are 28 SCFMs [28] [29] [30] [31] in total and each SCFM provides a dipole field of 2.6 T combined with a quadrupole field of 18.6T/m in a coil aperture of 173.4 mm at nominal current of 7345 A. The combined field is generated with a left-right asymmetric single layer coil made of the Rutherford type NbTi/Cu. Two SCFMs are set in one cryostat in forward and backward directions to constitute a defocus-focus doublet, while each dipole field is kept in the same direction. In series, all the SCFMs are cooled with supercritical helium at 4.5K and are excited with a power supply(8kA,10V).

2.2.4 Neutrino Beam Line (Secondary beam line)

The secondary beamline consists of three sections: the target station, decay volume and beam dump. (Fig. 2.8) The secondary beamline is filled with helium gas (1 atm) to reduce pion absorption and to suppress tritium and NO_x production by the beam. The target station contains a titanium-alloy beam window to separate the primary beamline vacuum and the target station heliumL a baffle which is a collimator to protect the magnetic horns and optical transition radiation monitor (OTR) to monitor the proton beam profile just upstream of the target; the target to generate secondary pions; and three

Fig. 2.6 Photographs of the primary beam line monitors. Upper left: CT. Upper right: ESM. Lower left: SSEM Lower right:BLM.

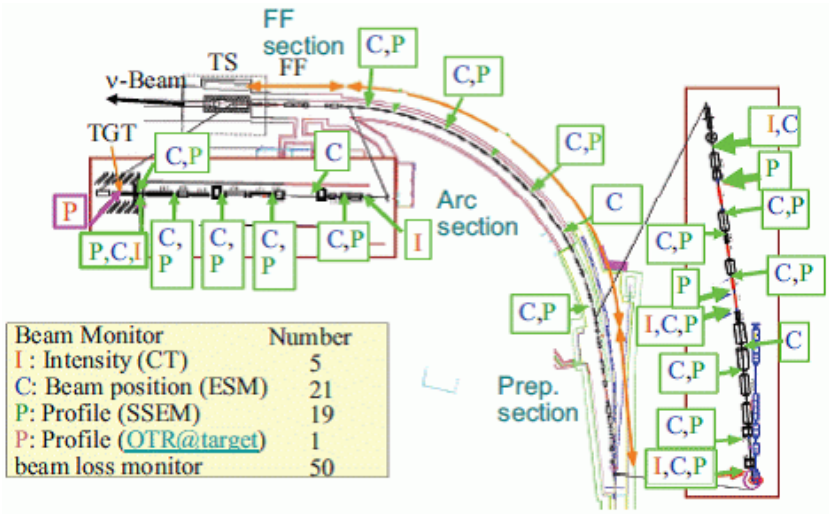

Fig. 2.7 Location of the primary beam line monitors.

magnetic horns excited by a 320 kA (250 kA until June 2010) current pulse to focus the pions. The pions enter the 96 m long decay volume and decay mainly into muons and muon neutrinos. All the remnants of the decayed pions and other hadrons are stopped by the beam dump.

2.2.5 Beam Monitors in beam line

2.2.5.1 Beam intensity monitor (CT)

The five current transformers (CTs) are toroidal coils; each consisting of 50 turns of a copper wire around a ferromagnetic core. To achieve a wide dynamic range of the response linearity for the short-pulsed bunches, CTs use a FINEMET (nanocrystalline Fe-based soft magnetic material) core, which has high saturation flux density, high relative permeability and low core loss over a wide frequency range. The

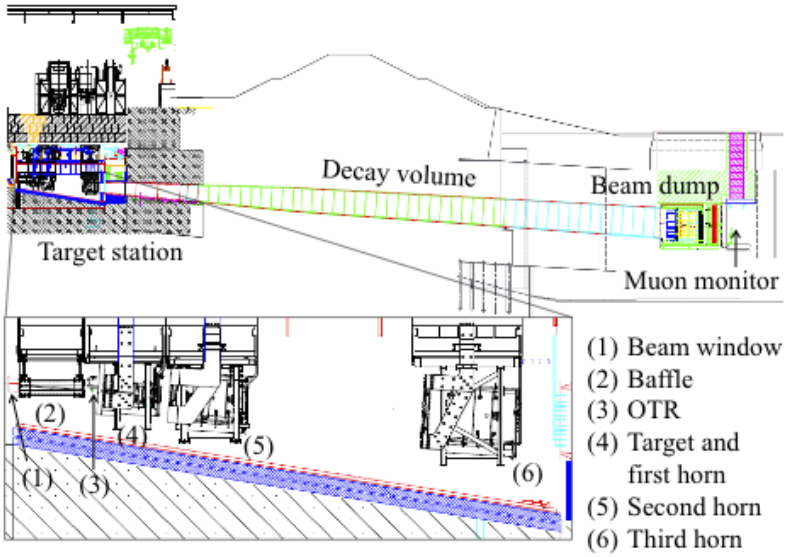

Fig. 2.8 Side view of the secondary beamline.

core's inner diameter is 260 mm and it weighs 7 kg. It is impregnated with epoxy resin. Between the core and the copper wire, radiation tolerant insulators are used: polyimide and alumina fiber tapes. Each CT is covered by an iron shield, to block electromagnetic noise. A CT's signal is read by a 160 MHz FADC[39]. The CT is calibrated using another coil around the core, to which a beam-like pulse current from a pulse generator is applied. The CT measures the absolute proton beam intensity with a 2% uncertainty and the relative intensity with a 0.5% fluctuation. It also measures the beam timing with a fluctuation of 5 ns in RMS.

2.2.5.2 Beam position monitor (ESM)

Each ESM has four rectangular electrodes surrounding the proton beam orbit (80-degree coverage per electrode). By measuring top-bottom and left-right asymmetry of the beam-induced current on the electrodes, it monitors the proton beam center position nondestructively (without direct interaction with the beam). The measurement precision of the beam position is less than 450 μm (20-40 μm for the measurement fluctuation, 100-400μm for the alignment precision and 200 μm for the systematic uncertainty other than the alignment), while the requirement is 500 μm. The longitudinal length of an ESM is 125 mm for the 15 ESMs in the preparation and final focusing sections, 210 mm for the five ESMs in the arc section and 160 mm for the ESM in the monitor stack. The ESM signal is read by a 160 MHz FADC[39].

2.2.5.3 Beam profile monitor (SSEM)

Each SSEM has two thin (5μm, 10^{-5} interaction lengths) titanium foils stripped horizontally and vertically, and an anode HV foil between them. The strips are hit by the proton beam and emit secondary electrons in proportion to the beam intensity. The electrons drift along the electric field and induce currents on the strips. The induced signals are transmitted to 65 MHz FADCs through twisted pair cables. The signal distribution is reconstructed as the proton beam profile. The systematic uncertainty of the beam width measurements is 200 μm while the requirements is 700 μm. Optics parameters of the proton beam (Twist parameters and emittance) are reconstructed from the profiles measured by the SSEMs, and are used to estimate the profile center,width and divergence at the target. SInce an SSEM cause a beam loss (0.005% loss), they are remotely inserted into the beam line only when the beam profile needs to be measured.

2.2.5.4 Beam loss monitor (BLM)

To monitor the beam loss, 19 and 10 BLMs are installed near the beam duct in the preparation and final focusing section respectively, while 21 BLMs are positioned near the SCFMs in the arc section. Each BRM is a wire proportional chamber filled with an Ar-CO_2 mixture. [32] The signal is integrated during the spill and if it exceeds a threshold, abeam abort signal is fired. Ten raw signal before integration is read by the FADC with 30 MHz sampling for the software monitoring. By comparing the beam loss with and without the SSEMs in the beam line, it was shown that the BLM has sensitivity down to a 16 mW beam loss. In the commissioning run, it was confirmed that residual dose and BLM data integrated during the period have good proportionality. This means that residual dose can be controlled by watching the BLM data.

2.2.5.5 Optical Transition Radiation Monitor (OTR)

The OTR has a thin titanium-alloy foil, which is placed at 45 degrees to the incident proton beam. As the beam passes through the foil, visible light (transition radiation) is produced. Some amounts of light reflected backward at 90 degrees to the beam are directed away from the target area; the light is transported in a dogleg path through the iron and concrete shielding by four aluminum 90-degree off-axis parabolic mirrors to an area with lower radiation levels. It is then collected by a CCD camera to produce an image of the proton beam profile. The OTR has an eight-position carousel holding four titanium-alloy foils, an aluminum foil, a fluorescent ceramic foil of 100 μm thick, a calibration foil and an empty disk. (Fig. 2.9)

A stepping motor is used to rotate the carousel from one foil to the next. The aluminum and ceramic foils are used for the middle and low intensity beam respectively, because they reflect more intense light than the titanium foil. The calibration foil has precisely machined fiducial holes, of which an image can be taken using back-lighting from lasers and filament lights. It is used for monitoring the alignment of the OTR system. The empty disk is used for back-lighting the mirror system.

2.2.5.6 Target

The target core is a graphite rod which is 2.6 cm in diameter and 91.4 cm long, with a density of 1.8 g/cm^3, which corresponds to 1.9 radiation length. The core is surrounded by a graphite tube, and they are both contained within a titanium case. The target is inserted in the first horn. The target is cooled by 1.6 atm helium gas. The gas flows at 250 m/s through the gaps between the core and tube and between the tube and case. When the 750 kW proton beam hits the target, the temperature at the center reaches 700°. A target core constructed of any other dense material would be melted away by the beam heating effect. The dose due to the radio-activation of the target is estimated at a few Sv/h after one year's irradiation by the 750kW[33].

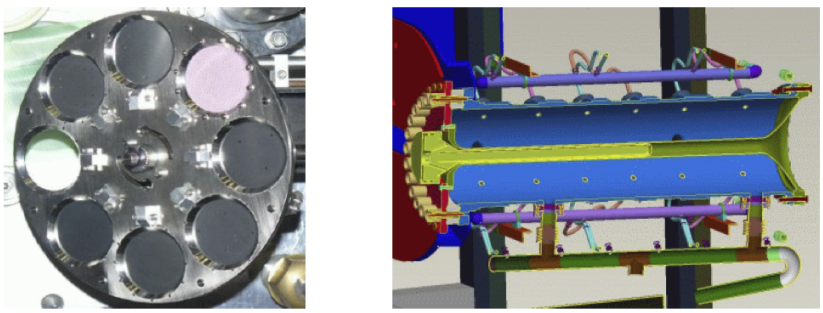

Fig. 2.9 Left: Photograph of the OTR. Right: Cross section of the first horn and target.

2.2.5.7 Magnetic horn

Each magnetic horn consists of two coaxial (inner and outer) conductors which encompass a closed volume [34] [35]. A toroidal magnetic field is generated in that volume. The field varies as 1/r, where r is the distance from the horn axis. The maximum field is 2.1 T. T2K adopts the three-horn configuration. The first horn collects the pions; the second and third horns focus them. The horn conductors is made of aluminum ally (6061-T6). Its dimensions (minimum inside diameter, inner conductor thickness, outside diameter and length are) are 54 mm , 3mm, 400 mm, and 1.5 m for the first horn, 80 mm, 3mm, 1000 mm and 2m for the second horn, and 140 mm, 3mm, 1400 mm and 2.5 m for the third horn, respectively. They are optimized to maximize the neutrino flux; the inside diameter is as small as possible to achieve the maximum magnetic field, and the conductor is as thin as possible to minimize pion absorption while still being tolerant of the Lorents force from the 320kA current and the thermal shock from the beam. The horns operated at 320 kA increase the neutrino flux at Super-K by approximately by a factor of 16 at the spectrum peak energy (0. GeV) the inside diameter is as small as possible to achieve the maximum magnetic field, and the conductor is as thin as possible to minimize pion absorption while still being tolerant of the Lorents force from the 320kA current and the thermal shock from the beam. The horns operated at 320 kA increase the neutrino flux at Super-K by approximately by a factor of 16 at the spectrum peak energy (0.6 GeV). The horns are connected in series by four pairs of aluminum bus-bars, through which the pulsed current (a few ms wide) is loaded. The currents on the bus-bars are monitored by four Rogowski coils per horn with the 200kHz FADC. The measurement uncertainty of the absolute current is less than 2THe horn magnetic field was measured with a hall prove before the installation, and the uncertainty is approximately 2% for the first horn and less than 1% for the second and third horns.

2.2.5.8 Decay volume

The decay volume is a 96 m long steel tunnel. THe cross section is 1.5 m wide and 1.7 m high at the entrance, and 3.0 m wide and 5.0 m high at the end. The decay volume is surrounded by 6 m thick reinforced concrete shielding. Along the beam axis, 40 plate coils are welded on the steel wall to cool the wall and concrete to below 100°C using water.

2.2.5.9 Beam dump

THe beam dump sits at the end of the decay volume. Its core is made of 75 ton graphite *1.7g/cm^3), and is 3.174 m long, 1.94 m wide and 4.69 m high. It is contained in the helium vessel. Two and 15 iron plates in and outside the vessel, respectively, are placed at the downstream end of the graphite core. The total iron thickness is 2.40 m. Only muons above 5 GeV/c can go through the beam dump to reach the downstream muon pit. The core is sandwiched on the both sides by aluminum cooling modules which contain water channels. The temperature in the center is kept at around 150°C for the 750 kW beam.

2.2.6 Muon Monitor

The muon monitor[36][37] is located just behind the beam dump, where the distance from the target is 118 m. It measures the bunch-by-bunch intensity and profile of muons, which are mainly produced along with neutrino from the pion two-body decay. SInce the muon beam is correlated with the neutrino beam, the muon monitor can monitor the neutrino beam intensity and direction in real time by measuring the muon beam. The neutrino beam direction is measured as a direction from the target to the center of the muon profile. The muon monitor is required to measure the neutrino beam direction with a precision better than 0.25 mrad, which corresponds to a 3 cm precision of the muon profile center. It is also required to monitor the stability of the neutrino beam intensity with a precision better than 3%.

2.2.6.1 Characteristics of the muon flux

The intensity and profile of the muon flux for 3.3 $\times$ 10^{14} protons/spill and 320 kA horn currents are estimated by using a beam line simulation code JNUBEAM as follows: 1 $\times 10^7$ charged-particles/cm^2/bunch (muons are around 87% and δ-rays make up the remaining percentage), a Gaussian-like profile around the beam center and approximately 1m width.

2.2.6.2 Muon monitor detectors

The muon monitor consists of two types of detector arrays: ionization chambers and silicon PIN photodiodes. (Fig. 2.10) Each array holds 49 sensors at 25 cm intervals and covers a 150 $\times$ 150 cm^2 area. The collected charge on each sensor is read by the 65 MHz FADC. The 2D muon profile is reconstructed in each array from the distribution of the sensors' charge. The arrays are fixed on a support enclosure, which is covered by double aluminum panels for thermal insulation. The temperature inside the enclosure is kept at around 34°C (within $\pm$ 0.7°C variation) with a sheathed heater for the benefit of the ionization chamber gas. An absorbed dose at the muon monitor is estimated at about 100 kGy for a 100-day operation at 750 kW. Therefore, every component in the muon pit is made of radiation-tolerant and low-activation material such as polyimide, ceramic, or aluminum.

2.2.6.3 Ionization chamber

There are seven ionization chambers, each of which contains seven sensors in a 150 $\times$ 50 $\times$ 1956 mm^3 aluminum gas tube. The 75 $\times$ 75 $\times$ 3 mm^3 active volume of each sensor is made by two parallel plane electrodes on alumina-ceramic plates. Between the electrodes, 200 V is applied. Two kinds of gas are used for the ionization chambers according to the beam intensity: Ar with 2% N_2 for low intensity and He with 1% N_2 for high intensity. The gas is fed in at approximately 100 cc/min. THe gas temperature, pressure and oxygen contamination are kept at around 34°C with a 1.5°C gradient and $\pm$0.2°C variation, at 130 $\pm$ 0.2 kPa (absolute), and below 2ppm,respectively.

2.2.6.4 Silicon PIN photodiode

Each silicon PIN photodiode (HAMAMATSU S3590-08) has an active area of 10$\times$ mm^2 and a depletion layer thickness of 300 μm. To fully deplete the silicon layer, 80 V is applied. The intrinsic resolution of the muon monitor is less than 0.1% for the intensity and less than 0.3 cm for the profile center.

2.2.7 Beamline Online System

For the stable and safe operation of the beamline, the online system collects information on the beamline equipment and the beam measured by the beam monitors, and feed it back to the operators. It also provides Super-K with the spill information for event synchronization by means of the GPS (Global Positioning System).

2.2.7.1 Event synchronization

At both the J-PARC and Super-K sites, the event timing is measured by using one pps (pulse per second) from two GPS receivers (for redundancy) and a 100 MHz clock from a rubidium clock with a precision of approximately 10 ns. When the timing signal synchronized with the MR extraction is received, the time is recorded to a local time clock (LTC) module at J-PARC. The LTC module counts the accumulated number of the received signals as the spill number. This time information and the spill number are sent to Super-K through L2-VPN, and are returned from Super-K to check consistency. The LTC module also provides the beam trigger for the beam monitors.

2.2.7.2 Beam Line DAQ System

The signals of the beam monitors are gathered into five buildings and are read by each readout system on a pill-by-spill basis. For the SSEM, BLM, horn current monitor and muon monitor, the COPPER/FINESSE system is utilized[38]. At each building, the signals are build into a sub-event. The

Fig. 2.10 Photograph of the muon monitor inside the support enclosure. The silicon PIN photodiode array is on the right side and the ionization chamber array is on the left side. The muon beam enters from the right side.

sub-events from all the buildings are sent to MIDAS[40], which controls the overall DAQ system, and are built into an event. The data size of an event is approximately 1.8 MB including the GPS data. The data processed by MIDAS is sent to an event distributor, which then distributes the data to online monitoring programs so that every spill is monitored in real time. The data is also recorded on disk in ROOT format.

2.3 Super-Kamiokande Detector

2.3.1 Super-K Detector features

The geometry of the Super-K detector consists of two major compartments, an inner and an outer detector which are separated by a cylindrical stainless steel structure. Fig. 2.11 gives a schematic of the Super-K detector geometry. The inner detector (ID) is a cylindrical space 33.8 m in diameter and 36.2 m in height which currently houses along its inner walls 11,129 inward-facing 50 cm diameter PMTs. Enclosing the ID is the inward-facing 50 cm diameter PMTs. Enclosing the ID is the outer detector (OD) which is a cylindrical space about 2 m thick radially and on the axis at both ends. The OD contains along its inner walls 1,885 outward-facing 20 cm diameter PMTs. The ID and OD boundaries are defined by as cylindrical structure about 50 cm wide. This structure consists of a stainless steel scaffold covered by plastic sheets which serve to optically separate the ID and OD. The wall facing int o the ID is lined with a black sheet of plastic meant to absorb light and minimize the number of photons which scatter off of the ID wall and pass between the two detector segments. The walls facing the OD, however, are lined with the highly reflective material Tyvek, in order to compensate for the OD's sparse instrumentation. With the Tyvek, photons reflect off of the surface of the OD walls and have a higher chance of finding their way to one of the OD PMTs. Finally, within the stainless steel scaffold there is a 50 cm d̈ead space; which combines with the ID and OD to make Super-K a total of 39 m in diameter and 42 m in height. THe ID is well instrumented, with 40% PMT cathode surface coverage, so that their sufficient spatial resolution to infer a number of physical quantities from the imaged neutrino interactions. The ID is linedwith Hamamatsu R3600 hemispherical PMTs, which feature a

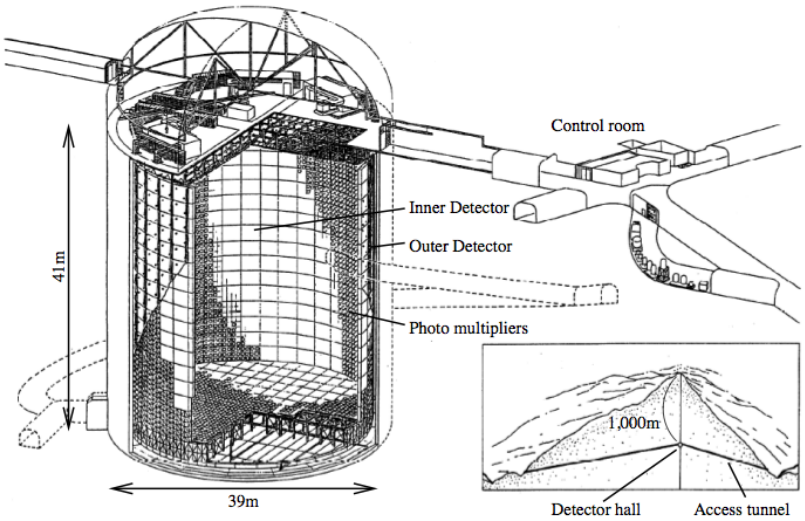

Fig. 2.11 Diagram of the Super Kamiokande Detector. The detector is mainly comprised of two segments, the inner and outer detectors. The boundary between the two segments is defined by a cylindrical scaffold used to mount photomultiplier tubes and optically separate the segments. The figure comes from [63].

combined quantum and collection efficiency of about 20%. Neutrino interaction often produce charge particles which, if above an energy threshold, produce a cone of Cherenkov photons as they traverse the water. When the photons reach the PMTs on the detector walls they produce a ring-shaped hit pattern which is used to extract the interaction's parameters such as the vertex position and particle directions. The primary strategy to measure the flavor composition of the T2K neutrino beam at Super-K, and thereby observe the oscillation of ν_ν to either ν_e or ν_τ, is to count CCQE interactions for muon and electron neutrinos both of which produce leptons of their respective flavor. Muons, counted to measure ν_μ disappearance ,are resilient to changes in their momentum due to their relatively large mass. As a result, muons that travel through the detector produce a well-defined cone of Cherenkov radiation which leads to a clear, sharp ring of PMT hits seen on the detector wall. In contrast, electrons, used to search for ν_e appearance, have a smaller mass and almost always induce electromagnetic showers. The resulting f̈uzzyr̈ing that an electron produces can be thought of as the result of may overlapping Cherenkov light cones. The routines in the Super-K event reconstruction software, sketched out in Section , use this difference between sharp and fuzzy to designate whether the rings imaged in the detector derived from muon-like or electron-like particles.

In contrast to the ID, the OD is only sparsely instrumented due to its original purpose as an active veto of cosmic ray muons and other backgrounds. The PMT array in the OD, made of 611 Hamamatsu R1408 PMTs and 1,274 R5912 PMTs, is capable of an almost 100% rejection efficiency of cosmic ray muon backgrounds. However, by selecting events in coincidence with the T2K beam, neutrino-induced events that illuminate the OD can be chosen from background events efficiently. From volume considerations alone, the number of OD events is expected to roughly equal the number of events in the ID. However, because of the OD's narrow geometry and sparse instrumentation, the OD lacks spatial and temporal resolution, which prevents detailed event reconstruction in the OD and, therefore, any ability to infer energy or particle identity. Nonetheless, the OD provides a sample of events which can be categorized into three types: events that produced light only in the OD; events where both detector segments are illuminated and the particles seem to originate from an interaction vertex inside the ID; and events where both segments are illuminated but the particles seem to originate from an interaction vertex outside of the ID.

2.3.2 Super-K Electronics

In 2008, the Super-K collaboration completed an upgrade to the detector's readout electronics[64][65] between the Super-K data-taking periods SK-III and SK-IV. This upgrade introduced a new schema in the acquisition of hits from the detector's 13015 PMTs. In the old system, once the total number of PMT hits within a 200 ns window exceeded a threshold, a hardware trigger would fire and direct the readout electronics to record data over a specified time window. However, the old front-end's data throughput was too low to accommodate a number of neutrino searches at low threshold, in particular those for solar neutrinos, because the trigger rate at the required threshold level would overload the front-end electronics. THe new upgraded electronics, therefore, includes a new front-end capable of a higher data processing rate. Furthermore, it improves upon the triggering method of the old system. In the new system, the arrival time and charge of each PMT hits in sent to a cluster of PCs that organizes the hit data and searches for event candidates based on programmable software triggers. The new electronics' combination of higher throughput and flexible triggers, along with other improvements such as better impedance matching and a larger front-end dynamic range, improved Super-K's stability to better accommodate a larger range of neutrino studies that not only require a lower threshold but also a more complicated delayed-coincidence trigger (e.g. supernova relic neutrino searches) and a coincident trigger with a beam as in the case of the T2K experiment.

The new front-end boards are named QBEE which stand for QTC Based Electronics with Ethernet. The name describes the units at the start and end of the boards' signal processing chain. The QTC, which stands for Charge to Time Converter, is a custom ASIC (Application Specific Integrated Circuit) that responds to input PMT pulses by producing a square-wave pulse[66]. THe front edfe of the QTC's output coincides with the arrival time of the PMT signal and the length is proportional to the integrated charge of the PMT pulse. The output of the QTC is then fed to a TDC (Time to Digital Converter) that digitizes the QTC pulses' times and lengths. Finally, the digitized data from the TDCs is sent to online PCs using Ethernet technology which provides the needed high rate of data transfer. Custom-made network interface cards, which transfer the data, consist of a TCP/IP firmware, called SiTCP[67], and other interface logic routines that are installed on an FPGA chip. The whole circuit on the QBEE board is able to transfer 11.8 MB/s of data according to a test where analog pulses are sent through the QBEE. This throughput corresponds to an input pulse rate of 85 kHz/channel and is an order of magnitude improvement over the old system which had a maximum hit rate of 1.4 kHz/channel. Each QBEE has eight QTC chips, and the whole DAQ system employs 550 QBEE boards which together readout Super-K's 13,015 PMTs and send their hit information to a cluster of online PCs.

The online PCs' role in the DAQ system is to organize the PMT hit information from the QBEEs and produce data files of candidate events which later undergo more offline analysis. The PCs fall into two groups based on their job. The first group of PCs, called M̈ergers, make a time-ordered list of all of the PMT hits. SOftware triggers then find event candidates from these lists. For each candidate event, a window is defined around the time of the event trigger and all the information for hits falling within that window is sent to one of the second set of PCs, called Örganizers. The Organized PCs merge the data for each candidate event and write it to disk for later offline analysis. There are ten Merger PCs, which each collect data from 30 QBEE boards. A single Organizer PC writes the candidate event date to disk. During a typical period of detector operation, about 470 MB/s of data flows form the Super-K PMTs through to the Merger PCs. That stream of hit information results in a software trigger rate of 2.6 kHz and eventually 9 MB/s worth of candidate event information being written to disk.

For the T2K experiment, the DAQ system was extended to trigger in time with the beam spills produced by the J-PARC accelerator. Each beam spill is given a GPS timestamp that is passed to the online Super-K PCs. Each timestamp is used to define an additional software trigger that records all the hit information in a 1 millisecond window around the T2K spill time. These spill events are then collected and written to disk. Later the events are fed into offline processing which applies the usual Super-K software triggers used to search for neutrino events, and any candidate events found are extracted for further T2K data analysis. Fig.24 displays a schematic of the DAQ setup.

2.4 Near Neutrino Detectors

The near detector site at 280 m from the target houses on-axis and off-axis detectors. The on-axis detector, composed of an array of iron/scintillator sandwiches, measures the neutrino beam direction and profile (INGRID). A modestly sized fine grained off-axis detector measures the muon neutrino flux and energy spectrum, and electron neutrino contamination in the direction of the far detector, along with measuring rates for exclusive neutrino reactions. These measurements are essential to characterize signals and background that are observed in the Super-Kamiokande far detector. The off-axis detector is composed of a water-scintillator detector optimized to identify π^0's (the P0D) follwoed by a time projection chamber and fine grained detector (TPC-FGD) sandwich, which are surrounded by an electromagnetic calorimeter (ECal). The whole off-axis detector is placed in a 0.2 T magnetic field provided by the recycled UA1 magnet, which also serves as part of a side muon range detector (SMRD[49]).

The complete chain of accelerator and neutrino beamline was successfully commissioned during 2009, and the T2K experiment began engineering runs on 23 December 2009, with neutrino data running from 23 January 2010 until 24 June 2010. In this period, we achieved a continuous beam power of 50kW, demonstrated, albeit briefly, a maximum power of 100 kW, and collected a total of 3.36×10^{19} protons on target for use in physics analysis.

Primary ND280 detector construction was completed in 2009 with the full installation of the INGRID, the central ND280 off-axis detectors (P0D, FGD,TPC and Downstream ECal) and the SMRD. The ND280 detector began stable operation in February 2010 and has recorded more than 95% of the delivered beam.

2.4.1 Neutrino Beam Monitors

As started earlier, the T2K experiment studies oscillations of an off-axis muon neutrino beam between the J-PARC accelerator complex and the Super-Kamiokande detector, with special emphasis on measuring the unknown mixing angle $theta_{13}$ by observing the subdominant $\nu_\mu \rightarrow \nu_e$ oscillation. The neutrino energy spectrum, flavor content and interaction rates of the unoscillated beam are measured by a set of detectors located 280 from the neutrino production target, and are used to predict the neutrino interaction at Super-Kamiokande.

The primary detector at the 280 m site is a magnetized off-axis tracking detector. The off-axis detector elements are contained inside the magnet recycled from the UA1 experiment at CERN. Inside the upstream end of this magnet sits a Pi-Zero Detector (P0D) consisting of tracking planes of scintillating bars alternating with lead foil. Downstream of the P0D three time projection chambers (TPCs), together with two fine grained detectors(FGDs) containing of layers of finely segmented scintillating bars, are optimized to measure charged current interactions. The P0D, TPCs, and FGDs are all surrounded by an electromagnetic calorimeter for detecting γ-rays that do not convert in the inner detectors, while the side of the magnet are instrumented with scintillator to measure the ranges of muons that exit the side of the off-axis detector. In addition to the off-axis detector, a separate array of iron/scintillator detectors called INGRID measures the on-axis neutrino beam profile at the 280 m site, while a set of muon monitor detectors located downstream of the beam dump monitors the beam direction and profile by detecting high energy muons from pion decay.

These detectors are housed in a pit inside the ND280 hall.

The pit has a diameter of 19 m and a depth of 37 m, and has three floors. THe B1 floor, about 24 m deep from the surface, houses the off-axis detector, which is early located on the line between the target point and the SK position. The B2 floor, about 33m deep, houses the horizontal modules of the INGRID detector. THe B3 floor, about 37 m deep houses the bottom modules of the vertical INGRID detector. The current off-axis angle is 2.5 degrees and the on-axis beam line passes at about 4m above the B2 floor. This facility design can accommodate the off-axis angles in the range of between 2.0 and 2.5 degrees with the condition that the on-axis detector covers the 4 m area.

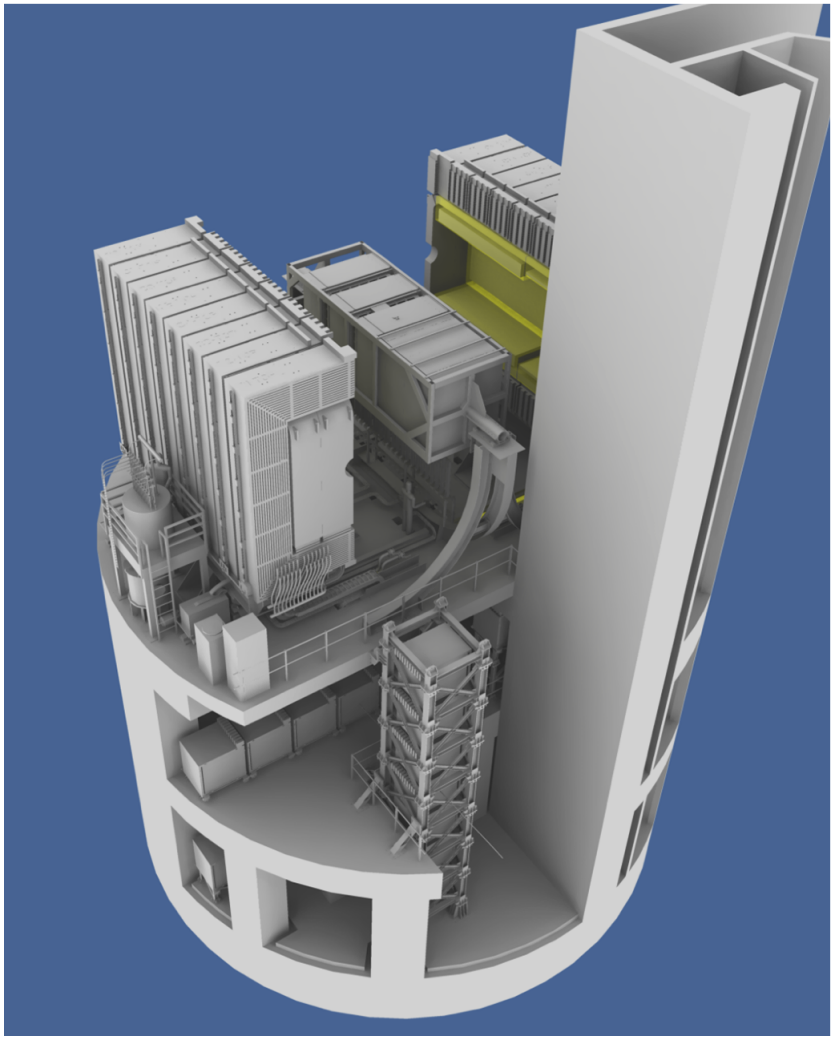

Fig. 2.12 ND280 detector complex. The off-axis detector and the magnet are located at the upper level, and the vertical and horizontal INGRID modules are locate at the bottom level.

2.4.2 INGRID

INGRID (Interactive Neutrino GRID) is a neutrino detector located on the neutrino beam axis. This on-axis detector was designed to monitor directly the neutrino beam direction and intensity by means of neutrino interaction in iron, with sufficient statistics to provide daily measurements at nominal beam intensity. Using the number of observed neutrino events is each module, the beam center is measured to a precision at the near detector pit, 280 meters downstream from the beam origin. The INGRID detector consists of 14 identical modules arranged as a cross of two identical groups along the horizontal and vertical axis, and 2 additional separate modules located off-axis directions outside the main cross, as shown in Fig. 2.13.

The detector samples the neutrino beam in a trans verse section of 10 m $\times$ 10 m. The center of the INGRID cross, with two overlapping modules, corresponds to the neutrino beam venter, defined as zero degrees with respect to the direction of the primary proton beamline. The purpose of the two off-axis modules is to check the cylindrical symmetry of the neutrino beam. The entire 16 modules are installed in the near detector pit with a positioning accuracy of 2 mm in directions perpendicular to the neutrino beam. The INGRID modules consist of a sandwich structure of nine iron plates and 11

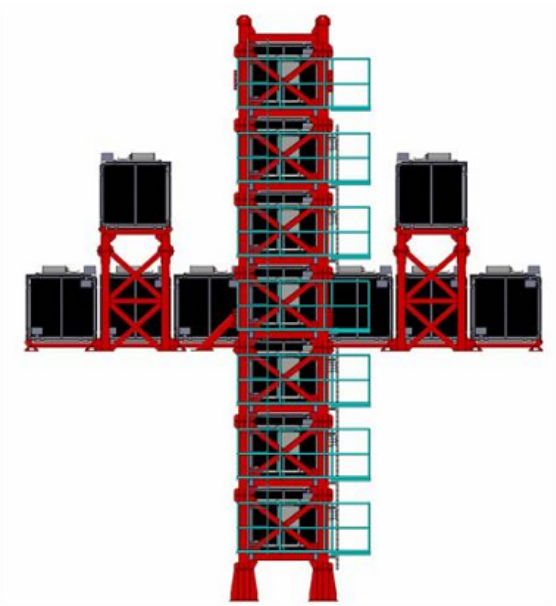

Fig. 2.13 INGRID on-axis detector.

tracking scintillator planes surrounded by veto scintillator planes as shown in Fig.11. The dimensions

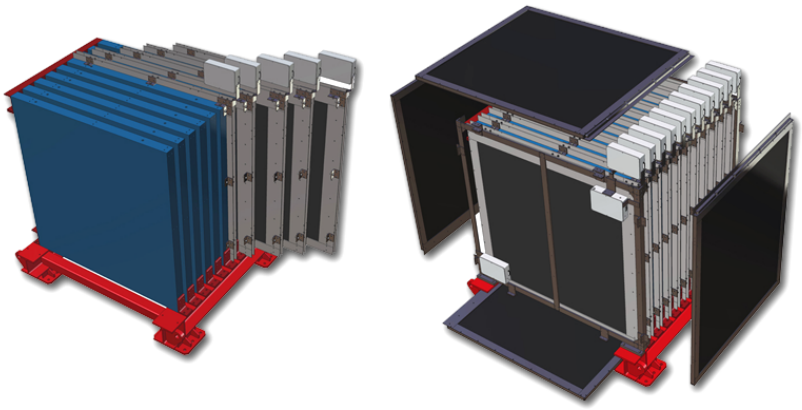

Fig. 2.14 An INGRID module.

of the iron plates are 124 cm × 124 cm in x and y directions and 6.5 cm along the beam direction. The total iron mass serving as a neutrino target is 7.1 tones per module. Each of the 11 tracking planes consists of 24 scintillator bars in the horizontal direction glued to 24 perpendicular bars in the vertical direction with Cemedine PM200, for a total number of 8,448. No iron plate was placed between the 10 th and 11 th tracking planes due to weight restrictions, without affecting the tracking performance. The dimension of the scintillator bars used for the tracking planes are 1.0 cm × 5.0 cm × 120.3 cm. Due to the fact that adjacent modules can share one veto plane in the boundary region, the modules have either three or four veto planes. Each veto plane consists of 22 scintillator bars segmented in the beam direction. The dimensions of those scintillator bars are 1.0 cm × 5.0 cm × 111.9 cm (bottom sides) and 1.0 cm × 5.0 cm × 129.9 cm (top, right and left sides). The total number of channels for the veto planes is 1,144, which gives a total of 9,592 channels for INGRID as a whole.

The extruded scintillator bars used for the tracking and veto planes are made of polystyrene doped with 1% PPO and 0.03% POPOP by weight. The wavelength of the scintillation light at the emission

peak is 420 nm (blue). They were developed and produced at Fermilab[44]. A thin white reflective coating, composed of TiO_2 infused in polystyrene, surrounds the whole of each scintillator bar. The coating improves light collection efficiency by acting as an optical isolator. A hole with a diameter of about 3 mm in the center of the scintillator bar allows the insertion of a wavelength-shifting (WLS) fiber for light collection. The WLS fibers used for INGRID are 1 mm diameter Kuraray Y-11 MS(200). THe absorption spectrum of the fiber is centered at a wavelength of 430 nm (blue). The small overlap with the emission spectrum, centered at 476 nm (green), reduces self-absorption effects in the fiber. One end of the fiber is glued to a connector by epoxy resin, ELJEN Technology EJ-500. The surface of the connector was polished with diamond blades. An MPPC is attached to each fiber using the connector. Finally, the set of scintillators, fibers and photosensors is contained in alight-tight dark box made of aluminum frames and plastic plates. The readout front-end electronics boards, the Trip-T front-end (TFBs), are mounted outside the dark box and each connected to 48 MPPCs via coaxial cables. Thus, one tracking scintillator plane has been completed.

INGRID is calibrated using cosmic data taken on the surface and, during beam, in the ND280 pit. As a result the mean light yield of each channel is measured larger than 20 pothoelectrons for mip tracks and it satisfies our requirement. Furthermore the timing resolution of each channel is measured 4.5 ns.

2.4.3 Off-Axis Neutrino Detectors

A modestly sized fine-grained off-axis detector (see Fig. **??**) serves to measure the flux, energy spectrum and electron neutrino contamination in the direction of the far detector, along with measuring rates for exclusive neutrino reactions. This characterizes signals and backgrounds in the Super-Kamiokande

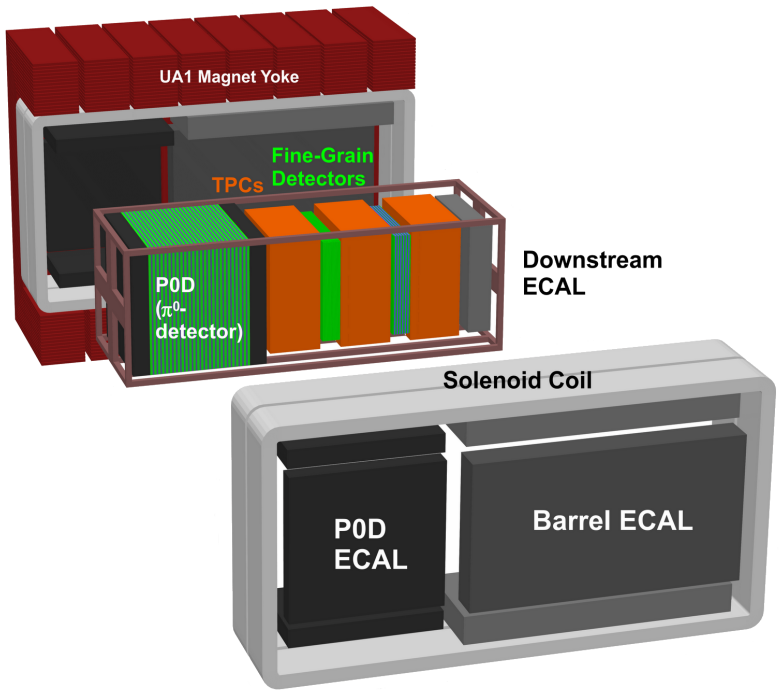

Fig. 2.15 An exploded view of the ND280 off-axis detector.

detector. The ND280 off-axis detector must satisfy several requirements. Firstly, it must provide information to determine the ν_μ flux at the Super-Kamiokande detector. Secondly, the $|nu_e$ content of the beam must be measured as a function of neutrino energy. The beam $|nu_e$ background is expected to be approximately 1% of the ν_μ flux and creates a significant non-removable background. Thirdly, it must measure ν_μ interactions such that the backgrounds to the ν_3 appearance search at Super-Kamiokande

Table. 2.2 Main parameters of the ND280 magnet.

Magnetic field	0.2 T
External dimensions	5.6 m (W) × 6.1 m (H) × 7.6 m (L)
Internal dimensions	3.5 m (W) × 3.6 m (H) × 7.0 m (L)
Iron yoke weight	850 tons, 16 independent C-elements
Coils material	Aluminum
Number of turns	208
Number of double pancakes	26
Total conductor weight	31 tons
Ohmic resistance (at T=$40^{c}irc$C	0.0576 Ω
Inductance	0.36 H
Nominal current	2900 A (for B=0.2T)
Nominal DC voltage	170 V (for B=0.2T)
Power dissipation	0.5 MW
Cooling water flow in coils	30 L/s
Water pressure drop in coils	7 bar

can be predicted. These backgrounds are dominated by neutral current single $\pi 0$ production. To meet these goals the ND280 off-axis detector must have the capability to reconstruct exclusive event types such as ν_μ and ν_e charged current quasi-elastic, charge current inelastic, and neutral current events, particularly neutral current single π^0 events. In addition, the ND280 off-axis detector should measure inclusive event rates. All of these requirements were considered in designing the off-axis detector. The constructed off-axis detector consists of the π^0 detector (P0D) and a TPC-FGD sandwich, both of which are placed inside a metal frame container, called b̈asket;̈ and electromagnetic calorimeter (ECal) that surrounds the basket; and the recycled UA1 magnet instrumented with scintillator to perform as a muon range detector (the SMRD).

The basket has dimension of 6.5 m (length) 2.6 m (width) 2.5 m (height). It is completely open at the top, to allow the insertion of the various detectors. Two short beams are fixed at the center of the two faces of the basket perpendicular to the beam axis. The short beams are connected outside the magnet to a structure fixed on the floor, which holds the basket. The beams contact the basket to the external support structure passing through the holes in the magnet coils, originally designed to allow the passage of the beam pipe. When opening the magnet, the Cs and the coils move apart, while the basket and the inner detector remain in the position chosen for data taking. The UA1 magnet provides a field of up to 0.2 T to momentum analyze the charge particles in the inner detector. In the following sections, more detailed descriptions of thee elements are provided.

2.4.3.1 UA1 Magnet

The ND280 off-axis detector is built around the old CERN UA1/NOMAD magnet providing a dipole magnetic field of 0.2 T, to measure momenta with good resolution and determine the sign of charged particles produced by neutrino interactions. A list of parameters in presented in Table 2.2. The magnet consists of water-cooled aluminum coils, which crete the horizontally oriented dipole field, and of a return yoke. The dimensions of the inner volume of the magnet, where the ND280 subdetectors are located, are 3.5 m × 3.6 m × 7.0 m. The external dimension are 5.6 m × 6.1 m × 7.6 m and the total weight of the yoke is 850 tones. The coils are made of aluminum bars with 5.45 cm × 5.45 cm square cross-section, with a central 23 mm diameter bore for water to flow. The coils are composed of individual p̈ancakesẅhich are connected hydraulically in parallel and electrically in series.

The magnet consists of two mirror-symmetric halves (Fig. 2.16)

The coils are split into four elements, two for each half, and are mechanically supported but electrically insulated from the return yoke. The two half yoke pieces each consist of eight C-shaped element, made of low-carbon steel plates, which stand on movable carriages. The carriages are fitted on rails and operated

Fig. 2.16 The ND280 magnet previously used at CERN for UA1/NOMAD.

by hydraulic moves, so that each half magnet is independent of the other van be separately moved to an open or closed position. When the magnet is in an open position, the inner volume is accessible, allowing access to the detectors. The magnet yoke and coils were reused from UA/NOMAD, while the movers were obtained from the completed HERA experiments at DESY. In order to comply with seismic regulations, detailed FEM static and dynamic analyses were performed and cross-checked with deformation and modal frequency measurements of the yoke elements. As a result of this, the carriages were mechanically reinforced by additional steel bars to increase their lateral strength. Additional components had to be specially designed and built for the ND280 magnet operation. These were: the power supply (PS), the cooling system (CS), the magnet safety system (MSS), and the magnet control system (MCS). Finally, the magnetic field map was determined with a dedicated measurement campaign.

The PS, specially made for ND280, was designed and manufactured by Bruker to provide the DC current to energize the magnet. The nominal current is 2900 A with a voltage drop of 170 V. Th requirements for the DC current resolution and stability were 300 ppm and ± 1000 ppm over 24 ours respectively. The PS is also able to cope with AC phase imbalance (± 2%) and short voltage drops. A thyristor switch mode was employed, with digital current regulation via a DCCT captor (ULTRASTAB series from Danfysik). The power supply can be controlled locally or remotely via the magnet slow control PC.

The CS, assembled by MAN ferrostaal AG (D) provides up to 750 kW of cooling power via two independents demineralized water circuits to compensate for the heat loss in the coils and in the power supply. The cold source consists of a primary glycol circuit maintained 8 °C by a chiller (built by Friotherm, D). The secondary pumping circuit units and their heat exchangers, the water purification units and the main panel controller are mounted in an ISO container, suitable for easy road and sea transport. They were assembled and tested in Europe before shipment to J-PARC. The secondary demineralized water for the magnet coils has a flow of 30 L/s and a pressure of 10 bar to compensate for the 7 bar pressure drop across the coil bare holes.

Th MSS, based on a hardwired fail-safe interface, was built to ensure the operational safety of the magnet. It continuously monitors a set of input signals from the thermo-switches mounted on the magnet coils, fault signals from the power converter, cooling and magnet control systems, and magnet

emergency stop signals from manual buttons located in the ND280 building. A boolean OR of all fault signals is generated and logically combined with the on/off magnet status. When the magnet is off, the system issues a power convert permit signal only if non of the input signals is in fault state. When the magnet is operating, a fast abort signal is generated and sent to the power converter in less than 1 ms when any of the input signals switches to fault state. All input and output signals of the MSS are monitored by a VME computer, and any change in the status of the signals is recorded with 1 ms timing resolution, meaning that the detailed sequence of events leading up to a fast abort can be understood.

The aim of MCS is to monitor the behavior of the magnet and cooling system, to control the current set point of the magnet power supply and to interface all the information and control parameters with the global slow control (GSC). The system is based on and industrial programmable logic controller (PLC) that reads the coil temperature at 52 points; the water flow, input and output temperature at 52 points; the water flow, input and output temperature and pressure on each half of the magnet; the voltage and current; and the status flags of the power converter, cooling system and magnet safety system.

The commissioning and B-field mapping campaign during August/September 2009 allowed us to fully test many aspects of the magnet and gain experience in its operation.

During the dedicated mapping campaign the magnetic field of the ND280 magnet was precisely measured with a computer controlled movable device equipped with 89 electronic cards, each holding three orthogonal Hall proves and the corresponding readout electronics. The overall mechanical structure of the device had dimensions of 2 m $\times$ 2 m $\times$ 1 m and could be moved throughout the whole instrumented region of the basket. Special care was taken in the region of the TPCs. The intrinsic uncertainty of each Hall prove in our region of interest is 0.2 G and the systematic error of the measurements is as low as 0,5 G. This could be ensured by a calibration method employing a very well-known homogeneous field of a magnet designed for this purpose. Higher order magnetic moments and second order Hall effects were taken into account for the measurements.

An important element of the field mapping was surveying the position and skewing of the measurement device before, during, and after its mapping campaign, Two surveys were carried out: one related the reference frame of the mapping machine to the ND280 main reference frame. The accuracy of this survey is better than 1mm in position offset and better than 1 mrad in rotation uncertainty. The second survey defined the internal reference frame of the mapping device, which is even more accurate with the possibility of measuring changes in position up to a precision of 10 μm. The alignment of the Hall proves with respect to each other was ensured at a level of 1m rad. The above-mentioned systematic error of 0.5 G was achieved by exploiting the ND280 magnet's Cartesian symmetry.

The measurement were performed at a magnetic field value of 0.07T - lower than the nominal field during neutrino data taking duet to limited electrical power available at the time from the ND280 facility. A scaling of the field value was therefore necessary to rescale to the nominal field, also taking hysteresis and saturation effects into account. By using a quadratical function as a first-order correction, afield uncertainty of 10^{-3} was obtained after scaling. The errors of the measurements scale in the same way, leading to final magnetic field uncertainty of 2 G for each field component at the nominal field of 0.2 T. This very precise knowledge of the magnetic field map, especially for the transverse field components, helps reduce the error on the momentum resolution, which is intended to be below 5%. Fig. 2.17 and 2.18 show two performance plots of the magnetic field mapping. Fig. 2.17 shows a slice of the TPC region, THe field is quite homogenous in the center of magnet but increasing varies the closer on comes to the edges of the TPC region.

In Fig. 2.18, the difference between our fit to the data and the actual measured values is plotted for each B-field component. The widths of the resulting distributions are a measure of the systematic error of the B-field measurement. They indicate residuals less than 1 G for each field component.

2.4.3.2 Pi0 Detector

The objective of the Pi-zero detector or P0D is to measure the neutral current process $\nu_\mu + N \rightarrow \nu_\mu + N + \pi^0 + X$ on a water (H_2O) target with the same neutrino beam that is aimed at Super-K. THese aims were realized by a design using x and y planes of scintillator bars, each read out with a single

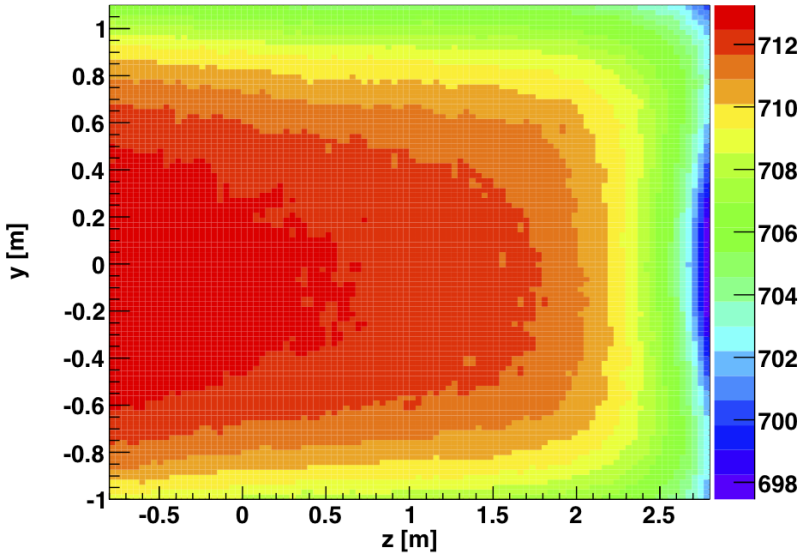

Fig. 2.17 The color plot shows a slice (x=0) of the mapped B-field (in Gauss) in the TPC region. The neutrino beam is entering the picture from the left.

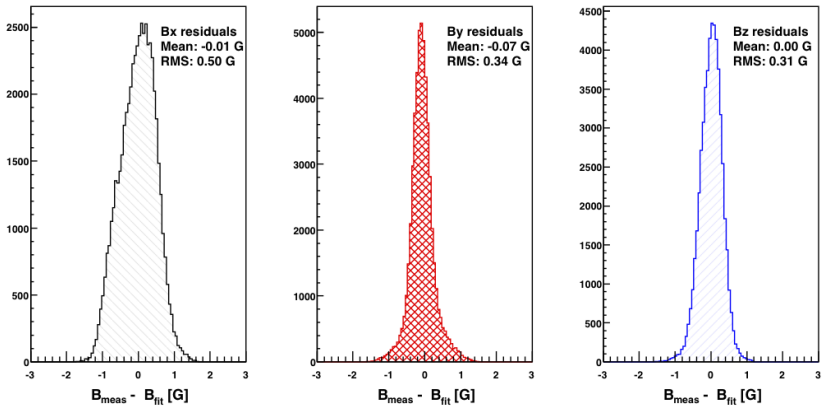

Fig. 2.18 For each B-field component the residuals between a fit of the data and the actual measurements is shown. The RMS of the distribution is taken as a measure of the systematic uncertainty of the mapping. The fit is performed in the center region.

wavelength-shifting fiber. The planes of scintillator bars are interleaved with fillable water target bags and lead and brass sheets. This arrangement forms an äctiveëutrino target where the P0D operates with the water target bags filled or emptied, enabling a simple subtraction to determine the water target cross sections. The scintillator bars provide sufficiently fine segmentation to reconstruct charged particle tracks (muons and pions) and electromagnetic showers (electrons and photons from π^0's).

The main feature of the P0D design are shown in Fig. 2.19.

The central section, composed of the üpstream water targetänd c̈entral water target; uses alternating scintillator planes, water bags, and brass sheets. This layout improves the containment of electromagnetic showers and provides a veto region before and after the water target region to provide effective rejection of particle interactions entering from outside the P0D.

There are a total of 40 scintillator modules in the P0D. Each angular scintillator bars. There are 134 vertical bars (2200 mm long) and 126 horizontal bars (2340 mm long) in each P0Dule. each bar has a single hole filled with a wavelength-shifting fiber (Kuraray multi-clad, S-5, J-type, doped with Y-11

Fig. 2.19 A schematic of the Pi-zero detector. The beam is coming from the left and going right. Insets show details of the Water Target SuperP0Dule layers and Central ECal layers.

*175 ppm) with a diameter specification of 1.00 mm). Each fiber is mirrored on one end and the other end is optically read out using a Hamamatsu MPPC. There are 40 P0Dules, each with 260 scintillator bars and fibers being readout, totaling 10,400 channels for the entire P0D detector. The P0Dules were formed into four s̈uper-groupsc̈alled Super P0Dules. The twoEal Super P0Dules alternating with 12 (13) water bag layers (28 mm thick), and 12 (13) bras sheets (1.5mm thick). The dimensions of the active target of the entire P0D are 2103 mm × 2239 mm × 2400 mm (width × height × length) and the mass of the detector with and without water is 16.1 tones and 13.3 tones respectively.

The P0D polystyrene scintillator bars were identical to bars originally developed for the MINERνA experiment[45]. The bulk polystyrene is Dow Styron 663 (W), a commercial grade, general-purpose polystyrene without additives. Wavelength shifting dopants, 1% PP) and 0.03 P)P)P, are added into the bulk polystyrene. The cross section of the extrusion is an isosceles triangle with a 33 mm base ad 17 mm height. There is a hole centered in both dimensions, with a diameter of approximately 1.5 mm, through which and optical fiber may be inserted. A thin (0.03 mm on average) co-extruded layer of poly styrene with 20% TiO_2 was added to the outside of the strip in order to reflect escaping light back into the bulk and increase the probability of capture by the center fiber.

The wavelength-shifting fibers were mounted in the scintillating bars by attaching glueing a custom ferrule over one end of each fiber so that a small portion of the fiber and epoxy extended past the ferrule. The fiber and epoxy were then diamond polished. The MPPCs are mounted in custom sleeves designed to snap-fit to a ferrule, allowing them to be installed and removed necessary. The P0D construction was done in three stages. First, the scintillator bars were glued into arrays of 15-17 bars on a template

mounted on an optical table, The gluing was done under a vacuum film and cured for four hours. These pre=glued bar arrays were called p̈lanks:̈ Each P0Dule uses 16 planks and a total of 640 are required for the entire detector. In the next stage, the P0Dules were constructed on a gluing table. The P0Dules were assembled as a sandwich of an outer lower PVC skin, eight x-scintillator planks, eight y-scintillator planks, and an outer upper PVC skin. ALl four edge of the assembly were enclosed with PVC frames which had been drilled with precision holes to allow the fibers to be inserted and connected to the MPPCs after the P0Dules were assembled. The assembly was coated with epoxy and cured under a vacuum film overnight. After the P0Dules were assembled, the fibers were inserted into each bar, and the MPPCs were attached to the fibers and connected via mini-coaxial cables to the TFB electronics boards. Then the P0Dule was scanned with a movable ^{6}0Co source to characterize the signal from every channel.

In the last stage, the instrumented P0Dules were assembled into SuperP-Dules by laying a P0DUle with lead plates (for the ECals) or water bags plus brass sheets (for the water targets) on a horizontal strong back table. This strong back table was lifted to a vertical position to assemble an upright SuperP0Dule. The water target layers each have two bags, for a total of 50 in the P0D detector, and each with the dimensions 1006 mm × 2062 mm × 28 mm. Finally, the electronics plus cooling assembly was mounted on the top and one side of the SuperP0DUle. Alight injection system was added that strobes the opposite end of the fiber with an LED flasher. FInal testing of the SuperP0Dules was done at J-PARC prior to installation int o the ND280 Detector using a cosmic ray trigger, the water bag filling system and the light injection system.

Determining the amount of water in the fiducial volume is critical to the P0D physics goals. The required precision is achieved by first measuring the mass vs depth in an external buffer tank, and then filling the water targets to predetermined levels. The water target volume is instrumented using a combination of binary level sensors and pressure sensors allowing the depth of the water to be determined to ± 5 mm. The water target fiducial region is designed to contain 1944 ± 53 kg of water.

During initial operations, all but seven of the 10,400 P0D detector channels were operational. The detector was calibrated with minimum ionizing tracks. An average of ?? photoelectrons was obtained for the scintillator bars and ?? photoelectrons per x/y layer. The average attenuation of the pulse height in the scintillator bars from opposite ends is approximately ??%. The internal alignment of scintillator bars was checked using through-going muons with the magnet field off, and was deter- mined to be approximately 3 mm.

2.4.3.3 Fine Grained Detector

Two massive fine grained detectors (FGDs) provide target mass for neutrino interaction as well as tracking of charged particles coming from the interaction vertex. The FGDs are constructed from 9.61 mm × 9.61 mm × 1864.3 mm × bars of extruded polystyrene scintillator, which are oriented perpendicular to the beam in either the x or y direction. Each scintillator bar has a reflective coating containing TiO_2 and wavelength-shifting fiber going down a hole in its center. One end of each fiber is mirrored by vacuum deposition of aluminum, while the other end is attached to a silicon multi-pixel photon counter[41][42][43] and associated electronics, which digitize the light signal produced by scintillation inside the bar.

Each FGD has outer dimension of 230 cm × 240 cm × 36.5 cm (width × height × depth in beam direction), and contains 1.1 tones of target material. The first FGD consists of 5,769 scintillator bars, arranged into 30 layers of 192 bars each, with each layer oriented alternatively in the x and y directions perpendicular to the neutrino beam. The scintillator provides the target mass for neutrino interactions, and having alternating x and y layers of fine grained bars allows for tracking of charged particles produced in those interactions. An ẌY modulec̈onsists of one layer of 192 scintillator bars in the horizontal direction glued to 192 perpendicular bars in the vertical direction, with thin G10 sheets glued to the outer surfaces to add structural stability. The photosensors are mounted along all four sides of the XY module on photosensor bus boards that are screwed directly into the edges of the XY module. Each fiber is read out from one end, and within an x or y layer alternating fivers are read out from alternating end. An LED-based light injection system that flashes the exposed far ends of the wavelength-shifting

fibers permits calibration of photosensor response, saturation, and non-linearity. The second FGD is a water0rich detector consisting of seven XY modules of plastic scintillator alternating with six 2.5 cm thick layers of water (for a total of 2,688 active scintillator bars and 15 cwerem total thickness of water). THese layers are made from sheets of thin-walled hollow corrugated polycarbonate, 2.5 cm thick, whose ends have been sealed with epoxy. The modules are then filled with water to provide a layer of water target. The water is maintained under negative pressure by a vacuum pump system so that if a leak develops the system will suck air into the modules rather than spilling water inside the FGD. Comparing the interaction rate in the two FGDs permits separate determination of cross section on carbon and on water. Both FGDs were built with the same geometry, mounting and readout for interoperability. Each FGD is contained in a light-tight dark box that contains the scintillator, fibers, and photosensors, while the FGD electronics are mounted in minicrate around the outside of the dark box. The modules are supported by several stainless steel straps that loop around the bottom of each module and attach to anchor points in the top side of the dark box. The dark box itself is a sturdy aluminum frame that supports the weight of the FGD modules and transfers that weight to the detector basket. The walls of the dark box are made of thin opaque panes to keep its interior light-tight.

Fig. 2.20 Photograph of an FGD with the front cover removed, supported by a portable brown cart. The surface of the outermost XY scintillator module is clearly visible, along with the fiber steel steps that support its weight.

2.4.3.3.1 FGD electronics

The FGD's front-end electronics resides in 24 mini-crates that attach to the outside of the four sides of the dark box. Signals from the photosensors inside the dark box are carried from the photosensor bus boards to the electronics by ribbon cables that attach to the crates' back planes, which are mounted over cutouts on the four sides of the box. The mini-crates are cooled by a negative-pressure water cooling system running along the sides of the frame of the dark box, and power is carried to the mini-crates by a power bus mounted on the frame. The electronics is arranged so that all heat-producing elements are located outside of the dark box in the mini-crates where thy can be readily cooled by the cooling system, while only elements with negligible power outputs (the photo sensors themselves) are present inside the dark box.

Each mini-crate contains four front-end boards and one master control card, and can read out 240 photosensors. THe frontend boards shape and digitize high and low attenuation copies of the photosensor signals at 50 MHz, storing the waveform in a 511-deep switched capacitor array. In addition the front-end boards provide the photosensor bias voltages and analog trigger primitives, Data from each crate is read out over optical fiber links to Data Collector Cards (DCCs) located outside of the magnet. These DCCs compress the data and pass it to the DAQ system. Slow control systems use a separate data and power bus for redundancy.

2.4.3.4 Electromagnetic Calorimeter

THe ND280 ECAL is a sampling electromagnetic calorimeter surrounding the inner detectors (P0D, TPCs, FGDs). It uses layers of plastic scintillator bars as active material with Pb absorber sheets between layers, and it provides near-hermetic coverage for all particles exiting the inner detector volume. Its role is to complement the inner detectors in full event reconstruction through the detection of photons and measurement of their energy and direction, as well as the detection of charged particles and the extraction of information relevant for their identification (electron-muon-pion separation). A key function of the ECAL is the reconstruction of π^0s produced in neutrino interactions inside the tracker detectors. In the case of π^0 production inside the P0D, the P0D-ECAL complements the P0D reconstruction with information on escaping energy. The ECAL is made of 13 independent modules of three different types arranged as in Fig. 13: six Barrel-ECAL modules surround the tracker volume on its four sides parallel to the z (beam) axis; one Downstream module (DS-ECAL) covers the downstream exit of the tracker volume; six P0D-ECAL modules surround the P0D detector volume on its four sides parallel to the z axis. Each module is made of consecutive layers of scintillator bars glued to a sheet of Pb converter. The DS-ECAL is located inside the basket carrying the inner ND280 detectors. The other 12 ECAL modules are mounted on the UA1 magnet iron yokes.

All scintillator bars have a 4.0 cm $\times$ 1.0 cm cross-section with a 1.0 mm $\times$ 2.0 mm elliptical hole running along their full length in the middle. The bars were extruded at the dedicated FNAL facility and the material used was polystyrene doped with 1% PPO and 0.03% POPOP. A 0.25 mm-thick layer of TiO_2 was co-extruded at the surface of the bars providing light reflection and isolation. Kuraray 1mm-diameter multi-clad Y11(200)S wavelength-shifting fibre runs along the hole in the centre of each bar. The fibers were cut to length and diamond-polished at a dedicated FNAL facility. Those read out at one end only are mirrored at the other end with vacuum-deposition of Aluminum done at the same facility. The light is read out at one or both ends of each fibre with MPPCs. Fibre-MPPC optical coupling is achieved using custom-made plastic connector assemblies with a sheath glued to the fibre end using Saint-Goban BC600 silicon-based optical epoxy resin and an MPPC holder that secures mechanically to the sea the and includes a layer of elastic foam to ensure good contact between the fibre end and the MPPC entrance window. The MPPC signal is read out with TFB card. The Pb sheets were made of pure Pb with 2% Sb to provide some stiffness and were primed on both sides with a quick-drying metal primer.

Each ECAL module was made by assembling pre-made scintillator-Pb layers. Each layer was prepared by laying the appropriate scintillator bars on a special Aluminum tooling plate, aligning then within a layer-border made of precision machined Aluminum bars, and glued to the Pb sheets using Araldite

2911 cured for a few hours under vacuum bagging. Each module mechanical frame is made of a Carbon-Fibre sandwich front plate providing support with minimum material in the way of incoming photos glued to an Aluminum frame, side plates made of thick Aluminum plates with holes to allow exit of the wavelength fibers, and back frames made of Aluminum plates providing support and the system to attach the modules in their final position. A separate side wall made of thinner Aluminum plates carries the TFB readout cards, special extruded pipes carrying cooling water, a dry-air circulation system, and support power distribution bars and signal and communication cables. A complete module is closed off with thin Aluminum covers for protection and light tightening. For every module, the mechanical structure was assembled and aligned and then the scintillator-Pb layers were installed one at a time. For each layer the fibers were threaded and glued to their seats. After the glue had vured all fibers of the layer were connected to a test system of MPPCs and readout electronics of well known performance and scanned with a ^{137}Cs source moved each bar in predefined intervals. An automated scanner, data acquisition system and analysis software suite allowed this process to be completed within a few hours for each layer. A very small percentage of damaged fibers were thus identified and replaced before the next layer was installed in the module. Once all layers of each module were in place the module was fitted with the readout electronics, cables, and other services, tested, and shipped to J-PARC for installation.

The DS-ECAL module consists of 34 layers with Pb sheets of 1.75 mm thickness for a total of $10.6X_0$. THere are 50 2.04m long bars in each layer and each one is readout with an MPPC at each end. Consecutive layers have their bars at 90° to allow 3-dimensional reconstruction of electromagnetic clusters and charged particle tracks. Limited by available space inside the UA1 magnet and structural considerations, the Barrel-ECAL module have 31 layers each with the same Pb sheets of 1.75 mm thickness for total of $9.7X_0$. Layers are again assembled with bar orientation alternating at 90°. The bars running in the z direction are 3.84m long and are read by MPPCs at each end. Bares running in the x(y) directions in the top/bottom(side) modules are 1.52m(2.36m) long and are read by a single MPPC at one end each.

The P0D-ECAL modules are not optimized for π^0 reconstruction as this takes place inside the dedicated P0D detector which they surround. However their presence is required to detect photons that do not convert in the active P0D volume or their showers-are only partically contained in it. It can also confirm the passage of charged tracks, identify MIPs, and act as veto for incoming backgrounds. This allows a simpler construction. Each module is made of 6 active scintillator laters separated by 5 layers of 4mm-thick lead converter giving $3.6X_0$. All bars are 2.34m long and run along the z direction for all layers. This simplifies construction while meeting the requirements as verified by Monte-Carlo simulation. Each bar is read out by a single MPPC at one end. The DS-ECAL module was constructed in 2008 and was used for beam tests at the CERN T9 PS mixed electron-muon hadron beam in April-June 2009. It was installed in ND280 in October 2009. The Barrel-ECAL and P0D-ECAL modules were constructed in 2009-2010 and were installed in ND280 in July-October 2010. The complete ECAL has been integrated with the rest of ND280 and is taking data.

2.4.3.5 Time Projection Chamber

The TPCs perform three key functions in the near detectors. Firstly, with their excellent imaging capabilities in three dimensions, the number and orientations of charged particles traversing the detectors are easily determined and form the basis for selecting high purity samples of different types of neutrino interactions. Secondly, since they operate in a magnetic field, they are used to measure the momenta of charged particles produced by neutrino interactions elsewhere in the detector, and therefore determine the event rate as a function of neutrino energy for the neutrino beam, prior to oscillation. FInally, the amount of ionization left by each particle, when combined with the measured momentum, is a powerful tool for distinguishing different types of charged particles, and in particular allows the relative abundance of electron neutrinos in the beam to be determined.

Each TPC consists of an inner box that holds and argon based drift gas, contained within an outer box that holds CO_2 as an insulating gas. The inner (outer) walls are made from composite panels with copper-clad G10 (aluminum) skins. THe inner box panels were precisely machined to form and 11.5

mm pitch copper strip pattern which, in conjunction with a central cathode panel, produce a uniform electric drift field in the active drift volume of the TPC, roughly aligned with the field provided by the near detector magnet. A simplified drawing of the TPC design is shown in Fig. 2.21.

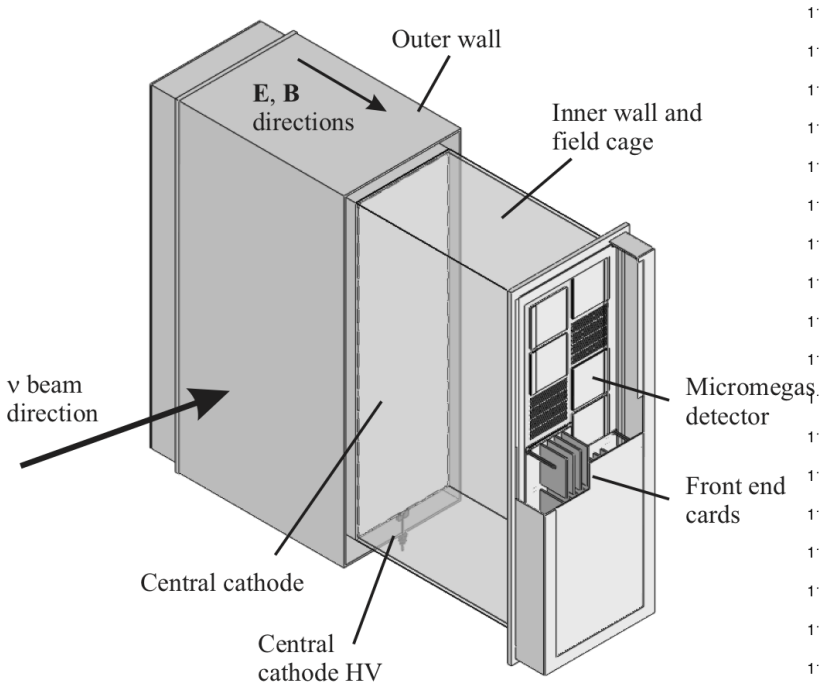

Fig. 2.21 Simplified cut-away drawing showing the main aspects of the TPC design. The outer dimension of the TPC are approximately 2.3 m × 2.4 m× 1.0 m.

Charged particles passing through the TPCs produce ionization electrons in the gas that drift away from the central cathode and towards one of the readout planes. There, the electrons are amplified and sampled with bulk micromegas[46] detectors with 7.0 mm × 10.8 mm × (vertical × horizontal) anode pad segmentation. The pattern of signals in the pad plane and the arrival time of the signals combine to give complete 3D images of the paths of the traversing charged particles. Twelve 342 mm × 359 mm micromegas modules tile each readout plane, for a total of 72 modules and nearly 9 m^2 of active surface for the three TPCs, the first to use micropattern gas detectors in a physics experiment. The modules are arranged in two vertical columns that are offset so that the small inactive regions between modules are not horizontally aligned.

Blind bias are used to route connections between the readout pads and connectors on the back side of the micromegas printed circuit boards. Six front-end electronics cards, each using four custom ASICs called ÄFTER; plug into the connectors and sample and digitize signals from the 1,728 pads. Each AFTER ASIC shapes the signals and buffers 72 pad signals into 411 time-bin switched capacitor arrays. The six front-end cards connect to as single front-end mezzanine card that aggregates the data, performs zero suppression, and sends the remaining data off detector over a 2Gb/s optical link.

The gas system was designed to maintain a stable mixture in the inner volume, and a constant positive pressure with respect to the outer volume, and a constant pressure between the outer volume and the atmosphere. The inner gas mixture, Ar:CF_4:C_4H_{10} (95:3:2) was chosen for its high speed, low diffusion, and good performance with micromegas chambers. Each of the three TPC volumes contains 3000 liters, and each of the three gap volumes contains 330 liters. The TPC gas system was designed for an operating flow of 10 L/min/TPC (30 L/min total flow), corresponding to five TPC-volume flushes per day. To reduce gas operating costs, the system was designed to purify and recycle roughly 90% of the TPC exhaust gas.

A calibration system produces a control pattern of electrons on the central cathode in order to measure

and monitor important aspects of the electron transport in the TPCs. Photoelectrons are produced from thin aluminum discs glued to the copper surface of the cathode by flashing the cathode with a diffuse pulse of 266 nm light. Data from this system are used to precisely determine the electron drift velocity and to measure distortions in the electron drift due to inhomogeneous and misaligned electric and magnetic fields.

Since late 2009, the three TPCs have been in place within the off-axis near detector, and the TPC siestas operated stably during the first physics run. After correcting for atmospheric pressure variation, the residual gain variation, due to other factors such as gas composition, is below 1%, and therefore does not degrade particle identification performance.

Particle identification is done with a truncated mean of measurements of energy loss of charged particles in the gas. The linear charged density of the track is estimated for each cluster by taking into account the length of the track segment corresponding to a pad column, The lowest 70% of the values are used to compute the truncated mean, an optimized approach found through Monte Carlo simulation and test beam studies. The resolution of deposited energy obtained using this method is about 7.8% for minimum ionizing particles, better than the design requirement of 10%.

The point spatial resolution is estimated by comparing the transverse coordinate resulting from the global track fit to the one obtained with information from a single column of pads. As expected, the resolution is found to be typically 0.7mm per column and degrades with increasing track angle with respect to the horizontal, duet to the ionization fluctuations along the track. The observed spatial resolution is sufficient to active the momentum resolution goals for the detectors. More information about the design, construction, and performance of the TPC systems can be found in a recent publication[47].

2.4.3.6 Side Muon Range Detector

The side muon range detector (SMRD) performs multiple functions. Firstly, it records muons which escape with large angels with respect to the beam direction and measures their momenta; secondly it triggers on cosmic rays which enter or penetrate the ND280 off-axis magnet; and thirdly, it helps identify beam related events which were generated in the surrounding cavity walls and the iron of the magnet. The detailed design and performance of SMRD is described at next chapter.

2.4.4 DAQ System

2.4.4.1 Readout Electronics

THe P0D, the ECal, the SMRD and the INGRID sub detectors use identical electronics to read out he MPPCs. THis electronics is based on the Trip-T ASIC[50] developed at Fermilab. Signals from 64 MPPCs are routed to custom-designed front-end boards (TFB) that house four Trip-T ASICs using miniature coaxial cables. The signals from the photosensors are capacitively spilt (1:10) and routed to two separate channels of the ASIC, to increase the dynamic range of the electronics. One Photoelectron signal corresponds to around 10 ADC counts in the high-gain channel, while the full-scale signal in the low gain channel corresponds to 500 pe.

The Trip-T chip integrates the charge in programmable integration windows, which are synchronized with the neutrino beam structure. There is a programmable dead time after each integration cycle, which is at least 50 ns long. The chip can store the result of 23 integration cycles in a capacitor array. Once the 23 integration cycles have been recorded, the data is multiplexed onto two dead-channel 12-bit ADCs, which digitize the data. Signals from the high gain channel are routed to a discriminator, which is part of the Trip-T ASIC. The front-end board is controlled by an FPGA, which also time stamps the output of the discriminator with a 2.5 s resolution. THe threshold is programmable from 0 to 5 p.e. The ADC and timestamp data is assembled by the FPGA and sent to a back-end board for data concentration and buffering. The output from the discriminators is used to calculate trigger primitives, which are used to initiate the readout of the detector for cosmic ray muons. Monitoring information (mainly temperature and voltages) is also recorded by the TFB and asynchronously transmitted to the readout merger module. More detail of the front-end part of the electronics can be found in [51]. The back-end of the electronics system consists of readout merger modules (RMMs), comic trigger modules

(CTMs), several slave clock modules (SCMs) and a master clock module (MCM). All the boards were developed at the Rutherford Appleton Laboratory using a common hardware platform, which has been built around a high-end Vertex II Pro FPGA from Xilinx, which is clocked at 100 MHz. The board can drive 14 high-speed optical links via its RoketIO and up to 192 LVDS links.

The signals from 48 TFBs, which are on the detector and typically less than 1 m away form the photosensors, are routed to one RMM via cat5e cables. The RMM controls the TFBs, distribute the clock and trigger signals and receives the data after a trigger signal is received by the TFBs. It sends this data asynchronously via a Gigabit Ethernet link to a commercial PC that collects and processes the data. The RMM is equipped with 500 MB DDR2 memory and can buffer up to 128 triggers. Each RMM receives trigger and timing signals from the SCMs (see below).

The master clock module receives signals from the accelerator that determine when the neutrino spill happens and also from a GPS-based clock. The latter signals are used to synchronize the electronics to UTC. The MCM is also connected to two cosmic trigger modules, which receive signals from up to 192 TFBs or from 48 crate master boards (in the case of the FGD). Based on these signals the CTM will decide whether there was a cosmic event in the detector and trigger the readout. The MCM can also generate pedestal and calibration triggers at a programmable rate. All timing and trigger signals are transmitted via the RocketIO-driven optical link to the slave clock modules. There is one SCM for each of the sub detectors (SMRD< ECal, P0D, FGD, TPC), which allows the electronics to be configured for independent operation of each sub-system. The INGRID is operated independently from ND280 and only uses one MCM and a single CTM.

2.4.4.2 DAQ and Global Slow Control

The ND280 data acquisition system has been divided in two components: DAQ and global slow control. The DAQ component takes care of the main data stream, collecting the data banks from each sub detector front-end system, storing the data in files and providing online histogramming. The global slow control (GSC) component runs in parallel to the DAQ using the dame software framework: MIDAS, developed at the Paul Sherer Institute and TRIUMF.

In terms of hardware, the GSC consists of two PCs and two network switches connecting to subdetector-specific equipment. Front-end tasks running on the GSC PCs or on a subdetector computer connect to the various equipments of the magnet and the subdetectors. A central shared memory database named ODB contains the setting and the read back information from all font-end tasks. This data is in turn stored in a MySQL database at regular intervals. Users interact with the GSC through web pages and can display history plots of any of the stored variables. Several customized web pages have been developed for controlling the magnet, power supplies, electronics parameter settings, and the TPC gas system, or for displaying temperature sensors, P0D water target levels, etc. Alarms are set up interactively to catch read back variables going out of range, alerting the shift person as well as sending messages to remote experts. The GSC system is the main tool used by the shift person responsible for safety matters.

The MySQL database containing the GSC information is expanding at the rate of 0.5GB per week while taking data. It is an essential element of the calibration process and offline analysis. This database is currently replicated from J-PARC to a server located at TRIUMF.

The ND280 and INGRID detectors are equipped with independent DAQ systems[52]. These have a common architecture and are based on the MIDAS DAQ framework, operating on commercially available computing hardware running the Scientific Linux operating system. MIDAS provides the system with a number of standard components necessary for operation and is interfaced to the experimental hardware through custom C/C++ front-end client applications.

In both the INGRID and ND280 systems the back-end electronics modules on the Trip-T based subdetectors are interfaced to the DAQ by point-to-point optical Gigabit Ethernet links. The MIDAS processes are distributed across a number of nodes to provide the necessary performance and to allow flexible partitioning of the system. An additional MIDAS instance is implemented for each of the FGDs and TPCs in the ND280 system. THese assemble data from the respective readout electronics and transmit it to the global DAQ. A par of commercial Gigabit Ethernet switches interconnect the nodes

in the DAQ system, providing local infrastructure and data transfer networks. The DAQ networks are isolated from the main T2K experimental network by a further node acting as a gateway.

The Trip-T based subdetectors are controlled and read out by the front end processor nodes (FPNs), each of which serves up to two back-end boards. The FPN is implemented as three tasks running as separate processes, interconnected by shared memory data buffers and communicating via standard interprocess mechanisms. Readout and configuration of the electronics and all connected hardware is provided by the readout task (RXT). The readout is parallelized across electronics boards in a multi-threaded manner and data s buffered for access by the data processing task (DPT). The RXT additionally receives periodic monitoring data from the TFBs which it passes to the global slow control. The DPT performs data reduction and basic data processing. The DPT decodes the TFB raw data blocks, associates amplitude and timing information for individual hits, performs pedestal subtraction on a channel-by-channel basis, applies zero suppression to the unspecified data and formats the data for output. To preserve monitoring information, the DPT also performs per-channel histogramming of signal amplitudes for specific trigger types prior to zero suppression and periodically inserts the histograms into the output data stream. The processed event fragments are buffered and dispatched to the DAQ back-end by the third process, which implements the MIDAS font-end functionality. Need to insert paragraph about TPC/FGD front-ends here.

The MIDAS framework provides the core components necessary for the DAQ system and is used to gather the event fragments from the Trip-T FPNs, the TPC and the FGD front-ends. An event-building process collects the fragments, performs some basic consistency check and writes the fully assembled events to a system buffer for output to a local RAID array. A custom archiver process transfers completed files to the KEK HPSS[53] mass storage facility over the network and additionally makes a preview copy to a local semi-offline system for fast-turnaround analysis.

Additional clients are provided to interface the DAQ to the light injection (LI) hardware for the ECal and P0D subdetectors. These configure the LI hardware according to predefined calibration sequences and monitor the status of the LI system. This information is provided in real-time to the DPT, where it is used to manage the formation of calibration histograms, A custom online-monitoring server based around the ROOT framework retrieves built events from the system buffer and generates a range of plots for data and detector quality monitoring.

2.4.5 T2K Data Processing and Distribution

2.4.5.1 ND280

The ND280 detector produces a few MB of data a second during normal data taking. Single raw data files are approximately 1 GB in size, and are recorded to disk every 10 minutes or so. The DAQ group writes these to the HPSS storage system at the KEK Computing Centre (KEKCC)as the primary archive for ND280 data.

2.4.5.2 Data Distribution of ND280

Fig.5 is a schematic of the flow of data from the ND280 counting room to the end-users, via the primary archive. From the primary archive onwards, we make use of tools that have been created for the GRID[54] to manage the flow and storage of data files. LCG utilities are used to transfer files to GRID storage elements at the RAL or TRIUMF laboratories in the UK and Canada respectively, where the data is also copied to long-term storage, for secondary archival. Multiple replicas of the same file therefore exist on the GRID. These are recorded and tracked using the LFC tools, which are based around a central catalog for all replica files.

2.4.5.3 Data Processing

Once the file are made available on the GRID, they are distributed to different sites of processing using the LCG tools. Subsequent processing of these files may be either GRID-based, or on independent computing clusters with their own batch processing systems.

2.4.5.4 Monte Carlo Processing and Distribution

Monte Carlo files are generated at computing sites across the collaboration. Once these files are generated, they are copied to the GRID, and archived at RAL and TRIUMF, and replicas made and tracked in the same way as the data files.

2.5 2010 Beamrun

Neutrinos for T2K experiment was derivered by J-PARC proton accelerator and neutrino beamline during Jan.2010 to Mar. 2011. The beam period is formalliy divided to 2 periods, Jan. 2010 to Jun. 2010 (Run I) and Nov. 2010 to Mar. 2011 (Run II). The beam power was gradually increased from 20 kw to 145 kw during these runs. The bunch cycle was 3.52 sec at Run I, 3.20 sec at most of RunII and 3.04 sec at last few days in Run II. The number of bunches was 6 at Run I and 8 at Run II.(Tab. 2.5)

Run	Period	Power	Cycle	# of bunches	delivered POT
Run I	Jan. - Jun. 2010	20 - 50 kW	3.52s cycle	6 bunches	3.26×10^{19} POT
Run II	Nov. 2010 - Mar. 2010	50 - 145 kW	3.20s (3.04s) cycle	8 bunches	1.12×10^{20} POT

Table. 2.3 Summary table of 2010 beam runs.

In this thesis, near detector analysis is carried out with Run I dataset and Super-Kamiokande with Run I+II. The difference of datasets is coming from understanding detectors. Super-Kamiokande had been run over ten years and the characteristics is quite well known. On the other hand, the condition of near detector is being examined by the groups of each detector components. The examination of near detector condition during Run I is finished and the datasets are reasonablly available in current stage. Since, extrapolation from Run I to Run II is applied to the ratio of near detector measurement and Monte-Calro. Here, only POT of each Run is considered for the extrapolation.

Chapter 3

Design and Basic Performance of Side Muon Range Detector

3.1 Detector Overview

The off-axis near detector complex consists of finely segmented detectors acting as neutrino targets and tracking detectors surrounded by a magnet and Side Muon Range Detector, SMRD. The inner part of this complex is divided into three regions: a π^0 detector, P0D, a tracking detector, FGD and TPC, and electromagnetic calorimeter, ECal. The SMRD is designed as the multi layers structure of plastic scintillation counters situated between iron plates and the iron yokes of the UA1 magnet. The main purpose of SMRD is to measure the momentum of muons created in neutrino interactions in the case when they escape the inner detector at large angles with respect to the neutrino beam. It is also designed to identify backgrounds from beam neutrino interactions in magnet yoke and surrounding walls and to provide a cosmic trigger signal for calibration of the inner detectors.

One of the main goal of the ND280 detector is to measure the neutrino energy spectrum. For charged current quasi elastic CCQE process neutrino energy is closely related to the muon momentum and its angle of emission. The active target mass is concentrated in the FGD and P0D detectors. Muons emitted at large angles with respect to the neutrino direction which do not cross TPC or go a short distance in the TPC are seen in the SMRD detector to measure their momenta and directions.

To fulfill the above requirements a high muon detection efficiency, a high hermetic layout and long therm stability are expected for SMRD detector. experimental

3.2 Detector Design

The side muon range detector is embedded in the UA1 magnet which is located at the neutrino experimental hall. The magnet is housed in an open detector pit 17m below the surface, 280m downstream from the carbon target and at an off-axis angle of 2.5°. The following sections describe the geometry, design and components of the SMRD.

3.2.1 The ND280 Off-Axis Magnet

The UA1 magnet consists of 16 flux return yokes which are grouped in pairs (labeled 1 through 8 from upstream to downstream with respect to the neutrino beam axis) to from a series of 8 consecutive rings which surround the magnetic field and the current coils on four sides. All 16 yokes have essentially the same fundamental dimensions with the four yokes forming the first and the last ring exhibiting slightly different geometry at the interface where two yokes meet to form a ring. The nominal outer dimensions of each yoke are 6150 mm × 2815 mm × 876 mm (height × width × depth) and the enclosed space measures 4040 mm × 3600 mm × 7568 mm (height × width × depth) for a relative ring spacing of 120 mm for the outermost rings and 80 mm for all other rings. The spacing between neighboring pairs of yokes measures 12 cm for yoke-pairs no (1,2) and no (7,8) and 8 cm for all others. The original

UA1 inner volume width was 80 mm smaller but the yokes were slightly modified for the NOMAD experiment. Each yoke is composed of sixteen 48 mm thick iron plates which are separated by 17 mm thick spacers and held together by long bolts. Figure 2 shows the basic structure of a single yoke and the slits in between iron plates. Slits which are located in between the same set of bolts are grouped into towers. Except for corner towers, all horizontally oriented slits have a nominal gap size of 17 mm × 700 mm × 867 mm (height × width × depth) , and all vertically oriented slits have a nominal gap size of 910 mm × 17 mm × 876 mm (height × width × depth). Due to imperfections and deformations of the magnet as well as welding seams of the spacers the actual gap sizes may differ slightly.

3.2.2 Geometry of the SMRD

Since the yokes consist of 16 iron plates they have 15 air gaps in radial direction. ll of the instrumented SMRD modules populate the innermost gaps so as to be able to detect particles escaping the inner detectors (the inner-module spacing in beam direction is determined by the spacing of yokes). Three layers of horizontal SMRD modules on the top and bottom arms for all yokes (two modules per layer per yoke's arm) are instrumented. All sides are instrumented with vertical SMRD modules (4 modules per layer per yoke's side) - 3 layers for yokes 1 through 5, 4 layers in yoke 6 and 6 layers in yoke 7 and 8. Hence, the SMRD consists of 192 horizontal and 248 vertical SMRD modules in total. The approximate external dimensions are 9 mm × 686 mm × 955 mm (height × width × depth) for horizontal and 9 mm × 892 mm × 955 mm (height × width × depth) for vertical modules. The longest module's dimension goes along the neutrino beam axis.

3.2.3 SMRD Modules

The counter sizes have been optimized to maximize the active area in each magnet gap. Due to the differently sized spaces for horizontal and vertical gaps, horizontal SMRD modules are composed of 4 scintillation counters with dimensions 7 mm × 167 mm × mm (height × width × depth) and vertical SMRD modules consist of 5 scintillation counters with dimensions 7 mm × 175 mm × mm (height × width × depth). Hence, the SMRD consists of 768 horizontal and 1240 vertical scintillation counters in total.

3.2.3.1 Extruded scintillator

Polystyrene-based scintillator slabs with double-ended WLS (wave-length shifting)fiber readout are used as active elements of the SMRD detector. The main feature of the SMRD individual counters is the usage of S-bent fibers. A Y11 WLS fiber is glued into a serpentine-shaped groove with BC600 Bicron glue. Such a design allow us to collect scintillation light uniformly over the entire plastic surface, to obtain a high light yield as well as to minimize the number of photosensors and electronics channels to a pair per a counter.

Extruded polystyrene scintillators (1.5% PTP, 0.01% POPOP) have been produced by Uniplast company in Vladimir, Russia, The outer surfaces of a slab are etched by a chemical agent, thus resulting in formation of a white diffuse layer. The deposit thickness is 30-100μm depending on etching time. The diffuse layer acts as a reflector and has been demonstrated to have an excellent performance. Extruded scintillators of this type have shown good light yield stability over two years.

After the etching procedure raw scintillator slabs were cut using Woodpecker 3D engraving-milling machine. Milling of S-shaped grooves was done at the next step. In SMRD counters the serpentine geometry of a groove consists of 7 loops with a diameter of 58 mm. Grooves of two different length are used: 2.10 m for horizontal counters and 2.22 m for vertical ones. A groove depth is 2.8 mm. A mill of 1.1 mm in diameter was used for slab treatment. The accuracy of the operations was about 100 μm.

3.2.3.2 Multi Pixel Photon Counter

Multi Pixel Photon Counter (MPPC) developed for T2K by Hamamatsu was chosen as the common photosensor for all ND280 detectors to cope with magnetic field and limited space inside UA1 magnet.

More than 4000 MPPCs are used to readout SMRD counters. The T2K MPPC is an array of 26 by 26 independent avalanche photodiodes (pixels) operating in Geiger mode. 9 corner pixels have been replaced by a lead bringing the total number of 50 $\times$ 50 μm^2 pixels to 667. The MPPC sensitive area of 1.3 $\times$ 1.3 mm ^{2} is well suited to accept light from 1 mm diameter Y11 fibers.

The MPPC signal is a sum of fired pixels and multi-pixel sensor operates as an analogue photodetector with dynamic range limited by the finite number of pixels. Typical light signal in SMRD counters is below 50 photoelectrons so the dynamic range issue can be neglected. The pixel can be represented as a micro capacitor which quickly discharges during Geiger breakdown initiated by an photoelectron until the voltage difference across it has decreased below the breakdown voltage. Overvoltage, the difference between the supplied bias voltage and the breakdown voltage, is the main parameter that affects the performance of MPPC and stability of its operation. The MPPC has an excellent single photoelectron resolution that allows us to perform an accurate calibration of each counter.

MPPCs are characterized by the following parameters at operational bis voltage and $T = 25°C$. Typical gain is 7.5 $\times$ 10^5; photo detection efficiency of about 25% is achieved at green light from Y11 fiber; average dark rate is 700 kHz with maximum values approached to 1 MHz; the combined crosstalk and after pulse probability is estimated to be 20=25%; recovery time of a single pixel is about 30 ps.

3.2.3.3 Counter Assembly

Endcaps were attached to scintillator slabs with glued WLS fiber and glued using BC600 optical glue. Scintillators with inserted fiber were tested with cosmic rays. It was found 20 counters that showed large asymmetry (more than 50%) in light yield between the ends due to damaged fiber cladding during gluing. This particular 20 counters were repaired by gluing new fiber in groove milled over the same place as previous with broken fiber. Counters which passed the test, were additionally wrapped by layer of 0.1 mm Tyvek paper. This increases a light yield by 15%. Then this counters were enveloped in a stainless steel lightproof container. The container was fixed to scintillator and endcaps with DP-490 black epox glue and a double side 20 $\times$ 0.15 mm Tesa adhesive tape. Additionally all joints between the container surface and the endcap were covered by a black Tesa adhesive tape of 25 $\times$ 0.065 mm. Each fiber end inside the endcap ferrule was cut by cylindrical mill and polished to provide good optical contact with the MPPC. After assembly, the dark noise of the SMRD counter with connected MPPC was measured on oscilloscope to ensure there is no light leakage into the envelope. In total, 2130 counters (800 - 167 mm and 1330 - 175 mm counters) were assembled and shipped to Japan. After shipping all counters were visually inspected as well as optical contact between ferrule and MPPCs. It was found that 230 optical contacts have an additional air gap between the fiber end the ferrule surface. It happened during the shipping. It was decided to fix endcap additionally by 2 screws for all shipped counters to ensure there will be no increase of air gap between fiber end and MPPC in optical coupling during counter movement inside the magnet gap and further degradation of the optical contact over the time. About 70 fiber ends have been also repolished. After additional measurements of the light yield and the coincidence rate between two ends for cosmic muon passed the center of counter, this counters were comprised in modules.

3.2.3.4 Module Assembly

Single counters are assembled into bigger units called modules to facilitate installation and position stabilization in the magnet slits. There are two type of modules: vertical and horizontal ones. Vertical modules consist of five counters while the horizontal ones of four counters. Aluminum extrusions are used to assemble the counters into the modules.

3.2.4 Readout electronics

The SMRD is using the same electronics as same of the other T2K near detectors P0D, ECal and the INGRID to read out the MPPCs. This electronics is based on the TRIP-T ASIC developed at Fermilab. Signal from 64 MPPCs are routed to custom designed front end boards(TFB) that house 4 Trip-T ASICS using miniature coax cables. The signals from the photosensors are capacitively spilt

1:10 and both routed to separate channels of the ASIC to increase the dynamic range of the electronics. A one photo-electron signal corresponds to around 10 ADC counts in the high gain channel, while the full scale signal in the low gain channel corresponds to 500 pe.

3.3 SMRD Counter Performance

SMRD consists from two components, the iron plate of UA1 magnet yoke and SMRD scintillation counter. The counter is the active component of SMRD. Though the detection efficiency of muons generated by neutrino interaction is the main concern, the performance of the SMRD scintillation counter is not obvious. In this section, the result of measurements of the light yield and position resolution of the SMRD scintillation counter is reported.

3.3.1 Outline

The SMRD counter is a polystyrene-based scintillator with embedded WLS fibers in S-bent groove. The geometry is followings:

- Horizontal counter: 7 mm × 167 mm × 875 mm (height × width × length)
- Vertical counter: 7 mm × 175 mm × 875 mm (height × width × length)

This S-bent groove design is proposed to optimize the light yield for double-sided readout with two MPPCs.(Fig. 3.1) To obtain the characteristics of this design, position dependency of light yield and position resolution, a SMRD counter was measured by scanning of cosmic rays. The mass production SMRD counters and MPPCs for practical SMRD are used for this measurement.

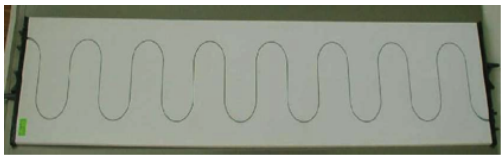

Fig. 3.1 The inner structure of SMRD counter. S-bent groove is dug in to the plastic scintillator and a WLS fiber is embedded in the groove. The readout is done by MPPCs connected to both ends of the WLS fiber. The practical counter is covered with thin stainless steel.

3.3.2 Setup

3.3.2.1 Cosmic Trigger Counter

For triggering cosmic rays, a trigger counter segmented by 20 × 20 mm^2 is used. The cosmic trigger counter is 3 layers structure which consists of twelve $80\times20\times10mm^3$ plastic scintillators. The scintillators are arranged with the alternate axes. WLS fibers are embedded in each scintillators and read out by multi anode PMTs. The coincidence of the 3 layers gives the cosmic trigger for each 20 × 20 mm^2 division on the SMRD counter. (Fig.3.2, 3.3)

3.3.2.2 SMRD Scintillation Counter

A horizontal SMRD counter, ID 167.304.1 is used as the sample. The inner 160 × 860 mm^2 region of the SMRD counter was scanned at each 20 × 20 mm^2 region with the cosmic trigger. Two MPPCs were connected to both end of WLS fiber in the SMRD counter as the photon counters. These counter and MPPCs are the same productions as practical SMRD.

3.3.2.3 DAQ

The signals of two MPPCs are amplified and recorded by Phillips Scientific 7186 20GHz TDC and LeCroy 2249w ADC. The cosmic trigger is given as the coincidence of three layers of the cosmic trigger

counter.

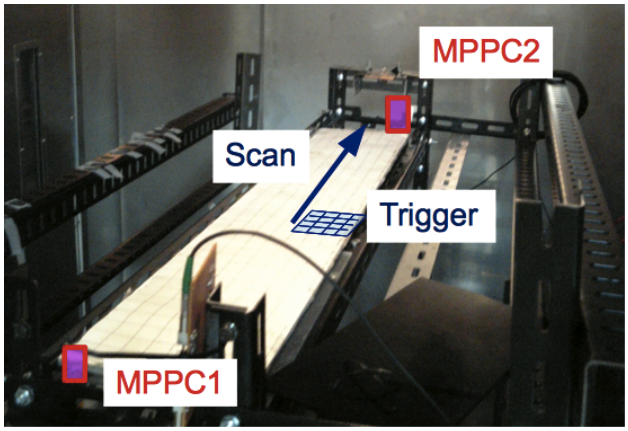

Fig. 3.2 A picture of comic measurement setup. The white board with the squares is the SMRD counter. A schematic picture of trigger counter and scanning method is written.

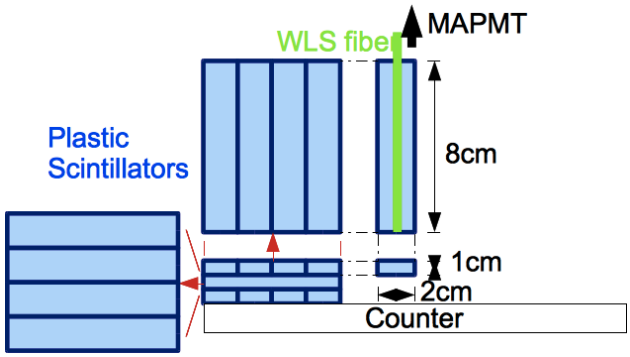

Fig. 3.3 A schematic view of cosmic trigger counter geometry is shown. The cosmic trigger counter consists of 12 small plastic scintillators. These scintillators are arranged with alternate axes. WLS fiber is embedded in each scintillators and read out with multi anode PMTs.

3.3.3 Analysis

The SMRD counter's ADC distributions are analyzed for the light yield map. The gain of MPPC was calculated from the peak structure of low light yield data.(Fig. 3.4) The light yield of each region was calculated with cosmic triggered data and the MPPC gain data. Both of MPPCs acquired about 40 photoelectrons for a muon penetrating near each of them and 25 p.e./MIP at the center of the counter. Total of these MPPCs' light yields is more than 30 p.e./MIP for all of scanned regions. The detection efficiency was found to be better than 99% for all of the counter. A Poisson distribution with threshold of 2.5 p.e. was assumed for the calculation.

Time difference between the left and the right MPPC (TDC_{right} and TDC_{left}) is measured at each position with TDC in 20 GHz mode. Fig. 3.5 shows the time difference. The signal propagation velocity along the long-axis is calculated as 6.55 cm/ns from the linear fitting of TDC_{right} - TDC_{left}. The non-linearity is estimated from the past measurement as 2% of the dynamic range. The position resolution is also calculated as 6.1 $\pm$ 0.8 cm from the velocity and the distribution of the standard deviation of TDC_{right} - TDC_{left}.

3.3.4 Conclusion

The >99% detection efficiency and the 6.1 $\pm$ 0.8 cm position resolution meet the T2K experiment requirements.

3.4 Cosmic Trigger System Test

One of the SMRD function is to provide the cosmic triggers to inner detector for monitoring these detectors continuously. In this section, early cosmic trigger test of SMRD detector is reported.

3.4.1 Outline

After the installation at 2009, cosmic trigger test of SMRD was performed at J-PARC. The purpose is to inspect the trigger function with SMRD. The cosmic triggers for ND280 off-axis DAQ system are generated by Cosmic Trigger Module (CTM). The most primitive cosmic triggers (trigger primitives)

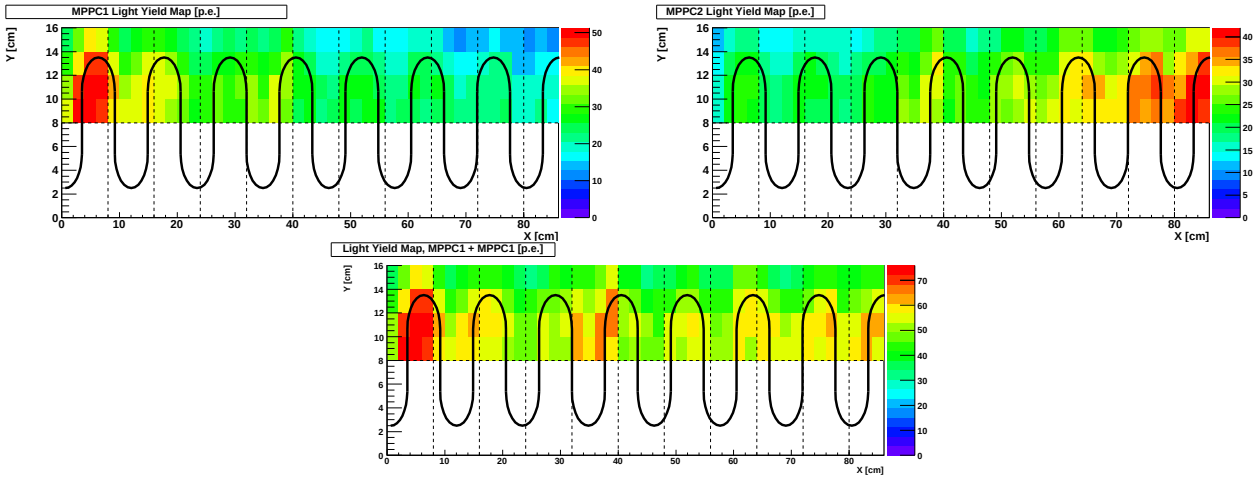

Fig. 3.4 The light yield map read by MPPC1 (top left), MPPC2 (top right) and total light yield of MPPC1 and MPPC2 (bottom left) are shown. The light yield is shown in the number of photo electrons.

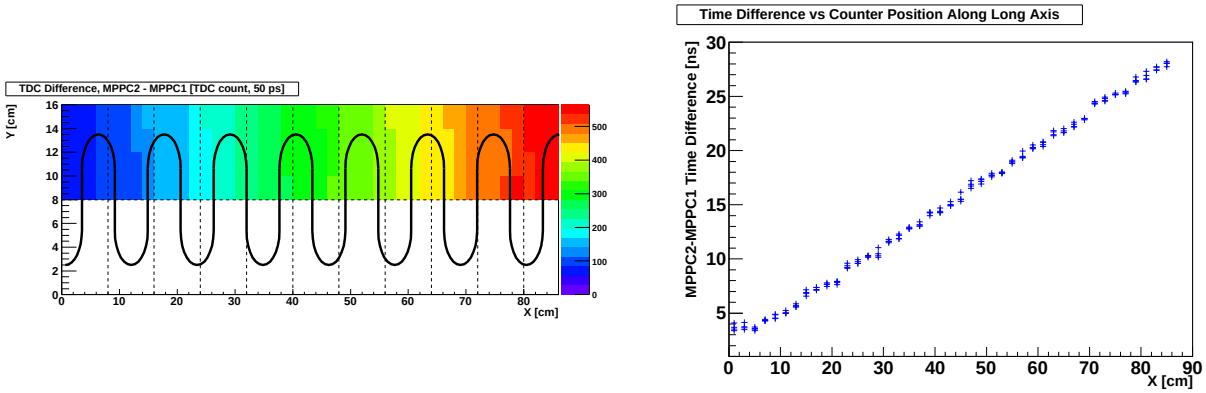

Fig. 3.5 The map of time difference between two MPPCs: TDC_{right} - TDC_{left}(left) and time difference vs position along X axis (right) are shown. Here, 1 TDC count is 50 ps. X axis is position along the long-axis of the SMRD counter [cm] and Y axis the time difference [TDC count].

are generated by TFB. In SMRD case, TFB watches the coincidence of pairs of two MPPCs connected to one SMRD counter. When TFB detect the coincidence of the pair of MPPCs, it provides a trigger primitive to CTM. The trigger primitive are inspected its coincidence by CTM with another trigger primitives from other TFBs. Then CTM generates the cosmic trigger to Master Clock Module, which controls data readout of the off-axis detectors. Here, early SMRD cosmic ray triggering system test and the result are reported. This test was done in late 2009.

3.4.2 Setup

Cosmic triggered events are acquired with two UA1 magnet status. One is opened magnet, in which status the parts of UA1 magnet were moved to the outside by 3.5 m. This status is for installation of ND280 detectors. Another is closed magnet. In this is status, the parts of UA1 magnet were moved inside and contacted. This is for usual beam data taking and turning on magnet field.

The trigger configuration of the DAQ is following:

- Coincidence timing window of TFB channels: 30ns.
- Required number of MPPC pairs: 2
- Coincidence configuration of TFB trigger primitives: TFBs should belong to other SMRD plane.

e.g. top plane - bottom plane.
- Coincidence timing window of TFB trigger primitives: 200 ns

3.4.3 Analysis

For the analysis, pattern matching was applied. The cosmic triggered events were classified with the following 5 patterns:

- A. SMRD top plane - bottom plane
- B. SMRD top plane - side plane
- C. SMRD side plane - bottom plane
- D. SMRD side plane - side plane

A Monte Carlo simulation was performed by Justyna Lagoda, and the ratio of patterns was compared.(Table 3.1, Table 3.2)

3.4.4 Results and Conclusion

The ratio of each patterns show good consistency, especially for opened magnet. We can conclude SMRD-CTM system works as expected.

Data sets	Run1928(Opened Magnet)	Simulation
Pattern A.	30.3±0.4% (14833 Events)	33.8±0.7% (4600 Events)
Pattern B.	52.3±0.3% (25636 Events)	52.2±0.6% (7112 Events)
Pattern C.	16.5±0.4% (8094 Events)	13.6±0.8% (1849 Events)
Pattern D.	0.2±0.5% (90 Events)	0.4±0.8% (52 Events)
Total: A-D.	99.3±0.03% (48653 Events)	100% (13613 Events)
ALL (2-3 TFB fired)	100% (48974 Events)	100% (13613 Events)

Table. 3.1 Comparison with data and Monte-Carlo simulation.(Opened Magnet) Percentages of each patterns at 2-3 TFB fired events are shown. The statistical errors are expressed.

Data sets	Run1928(Closed Magnet)	Simulation
Pattern A.	21.7±0.8% (2732 Events)	28.5±0.6% (5650 Events)
Pattern B.	33.6±0.7% (4226 Events)	33.2±0.6% (6581 Events)
Pattern C.	17.9±0.8% (2244 Events)	16.3±0.6% (3224 Events)
Pattern D.	2.9±0.9% (367 Events)	2.5±0.7% (494 Events)
Total: A-D.	76.1±0.4% (9569 Events)	80.5±0.3% (15953 Events)
ALL (2-3 TFB fired)	100% (12571 Events)	100% (19827 Events)

Table. 3.2 Comparison with data and Monte-Carlo simulation.(Closed Magnet) Percentages of each patterns at 2-3 TFB fired events are shown.

3.5 Beam Commissioning with SMRD

The beam commissioning for ND280 off-axis detectors was performed at Dec. 2009. The purpose is to synchronize the ND280 off-axis DAQ with neutrino beam and to optimize the DAQ parameters. SMRD found the event peak corresponding to beam spill. The off-axis detector DAQ was properly set to the beam timing basing on this analysis.

3.5.1 Outline

After the installation of ND280 off-axis detectors, the beam commissioning was performed at Dec. 2009 to Feb. 2010 with J-PARC beam line. The commissioning can be classified to two stages: timing adjustment and continuous data taking test with detectors. At the commissioning in Dec. 2009, timing adjustment between ND280 off-axis DAQ and neutrino beam spills was done.

3.5.2 Setup

In 13th to 21th Dec. 2009 run, the integration window of TFB was set as 1.5 μs to find the neutrino beam. (In the 2010 run, the integration was set to 440 ns.) The ND280 off-axis detector was closed during these period.

3.5.3 Analysis

At the 1st step, beam triggered events were picked up. At the 2nd step, the coincidence of two MPPCs belonging to one SMRD counter was required. The coincidence window was ± 30 ns. Eye scan was performed for events on beam timing. Two timing peaks were found at 16780 ns and 19680 ns.

3.5.4 Results and Conclusion

In 13th - 21th Dec. data, SMRD found 2 hit timing peak at 16780 ns and 19680 ns corresponding to the neutrino beam timing. (Fig. 3.6) ND280 off-axis DAQ was configured with 440 ns integration window for 2010 run successfully basing on this information.

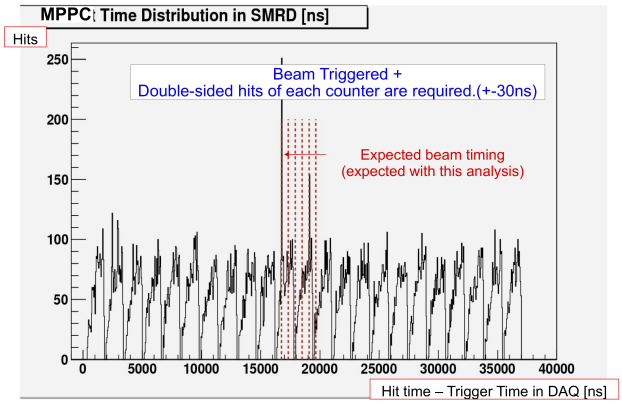

Fig. 3.6 SMRD hit timing distribution. One entry corresponds to one SMRD counter with coincidence hit within ± 30 ns. Two timing peak can be found in this plot. 1st timing peak corresponds to 1st beam bunch. 2nd timing peak is expected to be 5th beam bunch.

Bunch	1st	2nd	3rd	4th	5th	6th
POT	3.4×10^{15}	4.5×10^{14}	7.3×10^{14}	4.9×10^{14}	2.4×10^{15}	4.9×10^{14}

Table. 3.3 Total POT of neutrino beam run during 13th Dec. to 21th Dec.

3.6 Stability of SMRD

SMRD consists from UA1 magnet yoke, scintillation counters and MPPCs. In SMRD components, the most variable parts are MPPCs. The variants of MPPCs are coming from temperature of the neutrino experimental hall, where ND280 off-axis detector located. In this section, the stability of SMRD was studied.

3.6.1 MPPC Gain Monitoring

3.6.1.1 Setup

The ND280 off-axis DAQ system can acquire data with several types of triggers, e.g. beam trigger, cosmic trigger and pedestal trigger. The pedestal trigger is random trigger to monitor the MPPC thermal noise signals. For gain monitoring, the pedestal triggered data is used. The pedestal data are taken during beam run period. DAQ integration window was set to 440 ns.

3.6.1.2 Analysis

The gain of MPPCs are calculated with the random triggered events. For each channels, the ADC distribution are fitted with multiple Gauss functions. The difference between 1st and 2nd peak is defined as the gain of the MPPC. The gain distribution of all MPPCs of SMRD is shown in Fig. 3.7. The gain was monitored during all beam run period at 2010 and 2011. During $>$ 99% of the period, $>$ 99 % of MPPCs worked within $\pm$ 10 % of the average gain.

3.6.1.3 Conclusion

More than 99 % of MPPCs belonging to SMRD worked within $\pm$ 10% of the averaged gain during 99% of Run I and Run II. We can conclude SMRD worked stably during with more than 99% efficiency the beam run period.

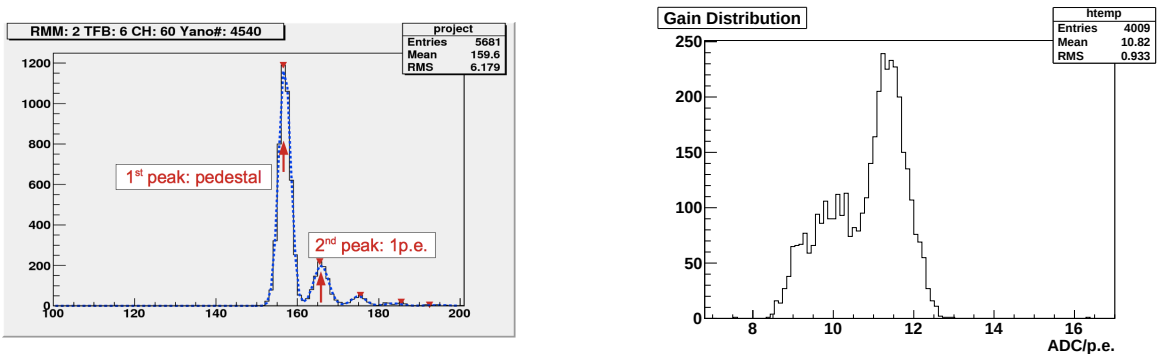

Fig. 3.7 An example of MPPC ADC distribution is shown. The MPPC is belonging to RMM 2 TFB 6 Channel 60.(left) The distribution is fitted with multiple Gauss functions. The difference between 1st and 2nd peak is defined as the gain of the MPPC. The gain distribution of MPPCs of SMRD.(right) Two peaks is coming from readout cable difference.

Chapter 4

Monitoring off-axis beam with SMRD

SMRD is the most massive detector of nd280 off-axis detectors. The mass is mainly coming from 850t UA1 magnet. About 5% of neutrino interactions in UA1 magnet is expected to be detected with SMRD counters. With this mass, SMRD can be managed as a neutrino monitor. In this chapter, the performance and stability of SMRD, monitoring beam with SMRD during early 2010 neutrino physics beam run are reported.

4.1 Beam monitoring

The energy spectrum and flux of T2K beam is easily changed by the difference off-axis angle of the beam. For T2K experiment, we have on-axis detector INGRID to measure the center position of neutrino beam. The requirements for the beam center measurements of INGRID is $\pm$ 1 mrad for each day. $\pm$ 1 mrad dispersion equals to $\sim$ 4.8% intensity dispersion at the energy peak of T2K off-axis beam. For this conversion, we have to depend on the beam simulation.
On the other hand, the off-axis detector are located on the same axis with SK and there's the possibility of direct measurement of the beam stability. SMRD detector consists form double-sided readout scintillation counter and the UA1 magnet, which has the weight of 850t. The double-sided readout enable the measurement with less noise event, in spite of the high noise rate of MPPC. The mass of UA1 magnet gives SMRD more neutrino interaction event. The effective mass of the UA1 magnet for SMRD event detection is studied as $\sim$ 5%. Here, the result of measurement of the T2K beam with SMRD is reported.

4.1.1 Beam Event Acquisition

The SMRD started the acquisition of physics neutrino beam event from Jan. 2010. Other inner detectors and UA1 magnet power supply was ready at March. 2010. As the whole of off-axis detector, the time period suitable for analysis is March. 2010 to Mar. 2011. For following analysis, the beam data during the period are used.

Here, the SMRD hit timing distribution is inspected to check the soundness of SMRD data taking. The SMRD hit is counted on the number of SMRD counters. The criteria of SMRD hit is followings:

- Both of two MPPCs of a counter have a signal with $>$ 10 p.e. light yield.
- The signals of MPPCs are coincident in $\pm$ 23 ns.

The light yield of MPPC is calibrated with the gain calculated as the method of Sec. 3.6.1. The SMRD hit timing distribution during the beam run is shown in Fig. 4.1.

4.1.2 Beam Timing in SMRD

At the early 2010 beam run, the T2K was still in the first stage of the experiment. The intensity of beam, setup of beam line magnet had been changing. These change of the beam setup can be cause of the different beam timing. The beam related SMRD hits have to be inside of the integration windows.

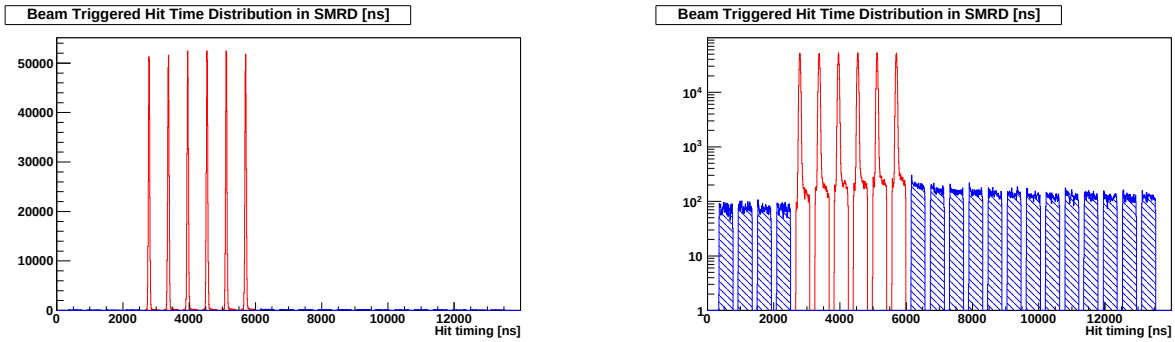

Fig. 4.1 Beam triggered hit time distribution in SMRD is shown. The hit is defined as a counter with double-sided coincidence hit. Each hits required to have 10 p.e. and these time difference should be in 23 ns. Red and blue regions are the 430 ns integration window of SMRD electronics. Red window has the hit peaks correlated with 6-bunch J-PARC beam. We can see the 150 ns dead time of our electronics as the time period without SMRD hits. Physics data during Mar. to Jun. is used to plot.

Here, the hit timing in SMRD during beam period are inspected.
The SMRD hit in integration windows with beam spill is plotted as the same integration window as shown Fig. 4.1, whole of beam period are used here. Fig. 4.3 shows the history of detected hit timing in the merged integration window. Each data point shows the SMRD hit timing peak fitted with Gauss function. The error bar is the SMRD hit timing dispersion defined as the sigma of the fitted function. During the data taking period, the SMRD hit timing dispersion was stable $\sim$ 20 ns and peak timing was placed 150 $\pm$ 20 ns. This means SMRD had been acquired the neutrino beam with the timing period of $\pm$ 6σ. This beam timing condition is sufficient for data taking with SMRD.

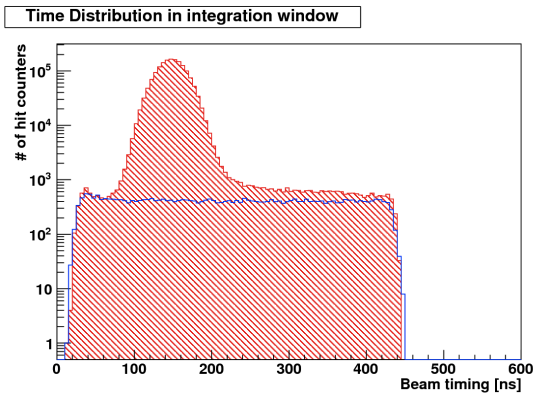

Fig. 4.2 Hit time distribution merged to a integration cycle is shown. The hits in the 6 integration windows with beam bunch is merged and shown as the red region. Blue line shows the sum of 6 integration windows neighboring these windows with beam.

4.1.3 Beam Stability

SMRD acquired the T2K neutrino beam during the beam period successfully. Here, the stability of beam intensity is studied basing on the hit base analysis of SMRD data.

SMRD hit rate is calculated with the number of beam related SMRD hits N_{SMRD} and total number of protons on target N_{POT}. The SMRD hits definition follows the definition at Sec. 4.1.1. N_{SMRD} is defined as $N_{SMRD} = N_{Beam} - N_{Empty}$. Here, N_{Beam} is the number of SMRD hits in the integration windows with beam spill. N_{Empty} is the normalized number of SMRD hits in the integration windows

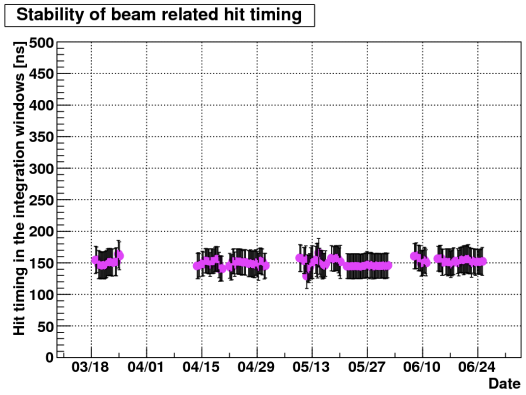

Fig. 4.3 The history of detected hit timing peak in integration cycle. Each point shows the mean timing of hit peak and error bar shows the width. The integration window is 10 ns to 440 ns. The beam timing and SMRD DAQ was synchronized quite well and the beam bunches are recorded with sufficient integration time.

without beam spill. For the normalization, factor 6/17 was applied. This is coming from 6 bunch structure of neutrino beam and 23 integration cycle of SMRD DAQ. We have 6 integration windows with beam spill and 17 integration windows without beam spill. The number of protons measured with the beam monitor nearest to beam target, CT5 is used as the total number of protons on target.

For each 12 hours, the number of beam related SMRD hits N_{SMRD} and total number of protons on target N_{POT} are counted up. Fig. 4.4 shows the history of beam related SMRD hit rate N_{SMRD}/N_{POT}. Best fit with constant value gives 5.93(6.12)± 0.11 (0.07) hits/ 1e+14 POT/12 hours in SMRD for Run I (Run II) datasets. As the error, RMS of data points are adopted. We can conclude SMRD detector has capability to work as the off-axis neutrino intensity monitor. The measured beam intensity at the off-axis detector position is stable in ± 2% and this result satisfies the requirement of T2K experiment.

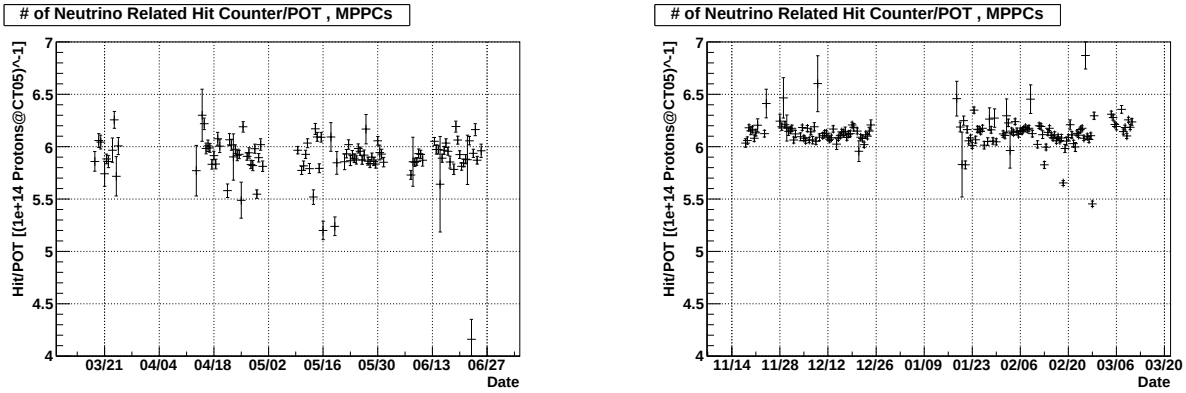

Fig. 4.4 Stability of the beam related hits measured by SMRD for Run I (left) and Run II (right) data. Each point corresponds to 12 hours data. The error bars shows statical errors. 5.93 ± 0.11 hits/1e+14 POT/12 hours in SMRD is acquired as hit rate for Run I. 6.12 ± 0.07 hits/1e+14 POT/12 hours in SMRD is acquired as hit rate for Run I.

Chapter 5

Measurement of Neutrino Beam at J-PARC

In this chapter, the measurement of ν_μ beam with off-axis near detector (ND280) at J-PARC is described. The goal of this chapter is to find the normalized factor, ratio of measured beam intensity to Monte-Carlo(MC) N_{obs}^{ND}/N_{MC}^{ND} for estimating $\nu_\mu$flux at Super-Kamiokande.

5.1 Outline of Analysis

At J-PARC, we measure the ν_μ beam intensity and give the normalization factor of MC for the ν_μ disapperance analysis stage. For the ν_μ intensty measurement, we count up μ tracks from ν interactions to select ν_μ CC inclusively. Though we cannot define precise mother neutrino energies with the information of μ from ν_μ CC interaction except for CCQE, the selection is still valuable to measure the intensity of ν_μ component in our neutrino beam.

At first, we select interaction events in our active target, Fine Grained Detector and then pick up a track with highest momentum in the interaction. Then information of the track in Time Projection Chamber or Side Muon Range Detector are applied to examine for μ possibility. The same cuts are also applied for MC, and then the number of ν_μ CC events N_{obs}^{ND} are compared with that of MC N_{MC}^{ND}. The normalization factor N_{obs}^{ND}/N_{MC}^{ND} are provided for estimating ν_μ flux at Super-Kamiokande.

5.2 Dataset

For ND280 analysis, real beam data correspoinding to 2.94×10^{19} protons on target (POT) and Monte-Calro simulation (MC) corresponding to 3.0×10^{20} POT are used. Both of real data and MC are processed for calibration and track reconstrcution with same analysis code, so called nd280 software v9r7p5.

5.2.1 Real Dataset

The T2K Run I dataset used in this analysis covers the beamrun period from Jan. to Jun. 2010. The off-axis detector ND280 joined to the beamrun from mid-March to late June 2010 and recorded 2.94×10^{19} protons on target (POT) with ND280 good data quality. ND280 good data quality is defined as the condition of ND280 detector. Each detector component were checked their conditions by subgroups. The period when all ND280 components, TPC, FGD, ECAL, P0D, SMRD and magnet are good condition is marked as ND280 good data quality period. For Run I, our ND280 corrected 96.7% of good spills under ND280 good data quality[75]. This period is conventionally split in 4 main "Main Ring" [MR] runs 31 to 34(Table. 5.1).

5.2.2 Monte-Calro Dataset

For comparison with real datasets, Monte-Calro simulation (MC) is provided with detector simulation GEANT4 v9r3p02 and neutrino generator NEUT v5.1.0. The detector setup in MC reproducts real

MR	period	ND280runs	POT
Run31	18/3-25/3	4165-4222	1.58e+18
Run32	13/4-1/5	4367-4546	7.16e+18
Run33	7/5-1/6	4671-4819	1.17e+19
Run34	7/-28/6	4979-5115	8.90e+18
All Runs			2.94e+19

Table. 5.1 Start and end dates for each MR run and corresponding POT.

ND280 detector condition at Run I period, full installation of TPC, FGD, P0D and SMRD, and partical installation of ECAL.The MC corresponds to total exposure of 3×10^{20} POT. The MC has been produed at a constant beam power of 50 kW, but the real data beam power was gradually increased from 20kW to 50 kW during Run I.

5.3 Event Reconstruction

The event reconstruction method is provided by nd280 software, and summarized as follows[78][79][80]:

1. Track reconstruction in TPC is performed. Hit pattern recognition is done by SBCAT (Scibar Cellular Automaton Tracker) algorythm[76] Then track fitting is done using a likelihood method.
2. Incremental Track-Hit matching is performed. Fitted TPC tracks are extrapolated into each plane of other detector components containig hits. Hits compatible with the extrapolated TPC track are grouped together and a track is formed. This track is then merged with the corresponding TCP track to from a combined track.
3. FGD isolated reconstruction is run. In this process, a search for isolated tracks among all FGD hits not associated to any TPC track is performed using SBCAT.
4. TPC-FGD track matching is done. The track segments formed in step 2 (TPC1-FGD1, FGD1-TPC2-FGD2 and FGD2-TPC3) are extrapolated to the same plane and the χ^2 for the matching is computed. Track pairs matched well together are merged and refitted with the Kalman filter in RECPACK[77].
5. Isolated track reconstruction for P0D, ECAL and SMRD is performed.
6. Finally all objects mentioned above are matched together to form the longest possible track using whole ND280 detector informtion. These global tracks are then again refitted with a Kalman filter.

5.4 Neutrino Interactions

The neutrinos in beam interact with the target materials through charged current (CC) and neutral current (NC) weak interactions. We classify these interactions into follows for near detector analysis:

- Charged current(CC) quasi-elastic scattering ($\nu + N \rightarrow l + N'$)
- CC current single π production ($\nu + N \rightarrow l + N' + \pi$)
- CC coherent π production ($\nu +^{16} O \rightarrow l + \pi +^{16} O$)
- CC Other interactions
  - CC single K production ($\nu + N \rightarrow l + K + \Lambda$)
  - CC single η production ($\nu + N \rightarrow l + \eta + N'$)
  - CC deep inelastic scattering ($\nu + N \rightarrow l + N' + hadrons$)
- NC current single π^0 production ($\nu + N \rightarrow \nu + N + \pi^0$)
- NC Coherent π production ($\nu +^{16} O \rightarrow \nu +^{16}) + \pi^0$)
- NC Other interactions

- NC current single $\pi^{\pm}$ production ($\nu + N \rightarrow \nu + N' + \pi^{\pm}$)
- Neutral current(NC) elastic scattering ($\nu + N \rightarrow \nu + N$)
- NC single K production ($\nu + N \rightarrow \nu + K + \Lambda$)
- NC single η production ($\nu + N \rightarrow \nu + \eta + N'$)
- NC deep inelastic scattering ($\nu + N \rightarrow \nu + N' + hadrons$)

where N and N' are the nucleons and l is the charged leptons, respectively.

5.4.1 Charged Current Quasi-Elastic Scattering Interaction

The chearged current quasi-elasitc scattering (CCQE) is the most remarkable interaction mode in our analysis, because of its kinematics. Since CCQE is a two-body interaction, we can reconstruct the energy of mother neutrino with following equation:

$$E_{\nu}^{CCQE} = \frac{(m_p - E_{bind})E_{\mu} - (E_B^2 - 2m_p E_{bind} + m_{\mu}^2)/2}{(m_p - E_{bind}) - E_{\mu} + p_{\mu}\cos\theta_{\mu}} \tag{5.1}$$

Here, E_{bind} MeV is a binding energy of target nuclei. $E_{bind} = 27$ is applied for C and O nuclei. E_{μ} and p_{μ} are the muon energy and momentum. The angle θ_{μ} is muon emittion angle. m_p and m_{μ} are the mass of proton and muon, respectively.

5.5 FGD - TPC analysis

In this section, we describe the measurement of T2K ν_{μ} beam intensity basing on reconstructed tracks with FGD and TPC constituents. FGD1 and FGD2 are used as active target detector with each $\sim$ 1t mass, and TPCs are used to provide the track momentum and particle identification information.

5.5.1 Selection for Muons Induced from ν Interaction

The basic idea of the selection is to extract μ tracks with the highest momentum induced from the neutrino interaction in FGD. These tracks gives us inclusive selection for ν_{μ} CC interaction events, which is suitable for measurement of ν beam intensity. Here, the cuts for the μ selection are described.

5.5.1.1 Event Bunching

We had 6 beam bunches per spill with 581 ns separation time during Run I beam period, and our reconstructed tracks represents the structure with 6 bunches. In order to select tracks produced in beam neutrino interactions, only tracks starting in a time window of nominal bunch time $\pm$ 86 ns are considered. The width 86 ns is chosen as 4 times as the typical RMS of bunch structure in data.
Following cuts are applied for each 6 bunches independently, to avoid missing duplicated ν interaction in the spill as possible.

5.5.1.2 Upstream TPC VETO Cut

We request no reconstructed track in upstream TPCs for rejecting the background muons from the upstream sand and concrete walls of ND280 pit. At first, we search for tracks starting in FGD1 under the condisiton that no track exists in TPC1. If there is no track in FGD1, we apply the same procedure for FGD2 with TPC2.

5.5.1.3 FGD Fiducial Volume Selection

At least one FGD track is requested which has its most upstream position in FGD FV with TCP Hits > 18. Definate TPC hits are required to provide momentum measurements for the track. The geometry of FGDs' active volume and fiducial volume (FV) are shown at Table. 5.2. The two FGDs are not identical; FGD1 alternates two layers of scintillator bars (9.8mm wide each) with a gap of 2.65 mm,

while FGD2 has a larger inactive gap of 32.65 mm between layers. The 25 mm of a gap in FGD2 corresponds to the water target.

	FGD1 Active [mm]	FGD1 FV [mm]	FGD2 Active [mm]	FGD2 FV [mm]
X_{min}	-932.17	-832.17	-932.17	-832.17
X_{max}	932.17	832.17	932.17	832.17
Y_{min}	-877.17	-777.17	-877.17	-777.17
Y_{max}	987.17	887.17	987.17	887.17
Z_{min}	115.95	123.35	1473.95	1481.35
Z_{max}	447.05	447.05	1807.05	1807.05

Table. 5.2 The geometry of FGD active, fiducial volume.

For the vertex position, we define to be most upstream position of highest energetic tracks in the events. The comparison for the geometrical distribution of vertices in the FGDs is shown in Fig.[5.1].

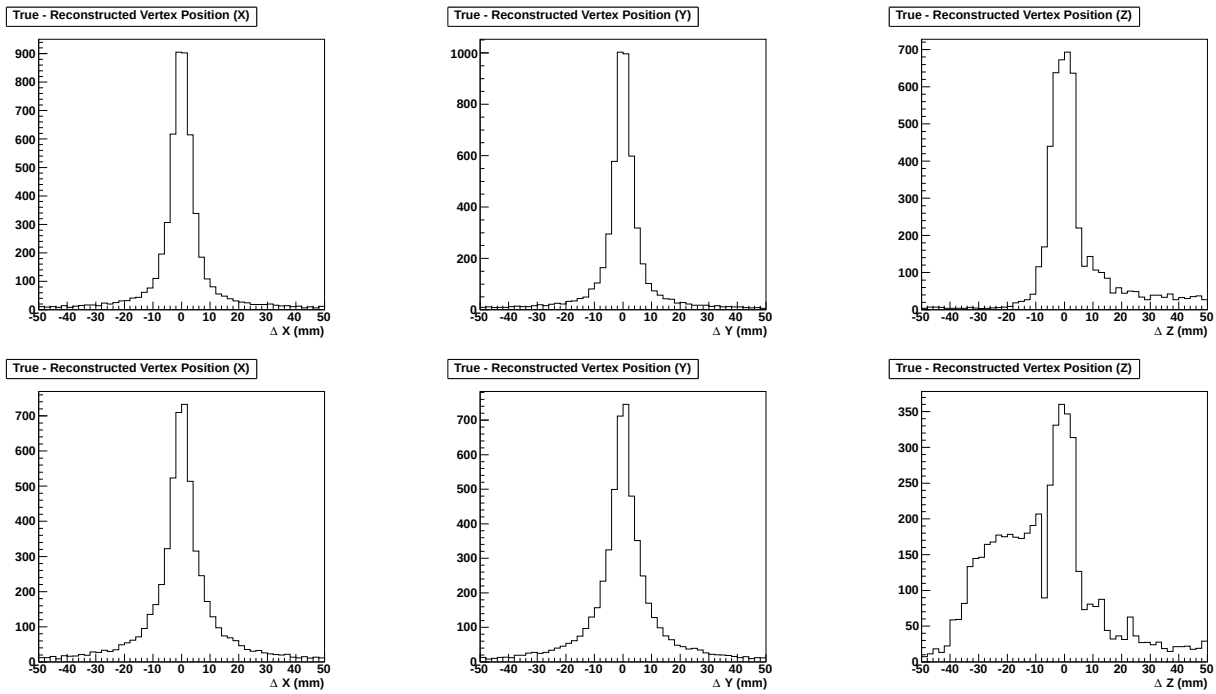

Fig. 5.1 Disribution of the difference of true and reconstructed vertex ΔX, ΔY and ΔZ in FGD1(top row) and FGD2 (bottom row).

5.5.1.4 Negative Highest Momentum Tracks Selection

In this selection, we search the track with the higest momentum (HM) among the all tracks starting in the FGD fiducial volume and having TPC track constituents in downstream. Then, request the HM track to be negative and has the momentum larger than 100 MeV/c.

5.5.1.5 Particle Identification

Finally, we applied particle identification criteria as follows: $|\delta_E(\mu)| < 2.5$ to select muons and $|\delta_E(e)| > 2$ to reject low energy electrons/positrons.
$\delta_E(e/\mu)$ is the so-called "pull" value which is the difference between the expected and mesured value of the ionization rate in TPC divided by the deposited energy resolution for the different hypotheses on the particle type. The pull has been corrected on a run-by-run basis to center its distribution on zero.

In Fig. 5.2, pull distribution for data, MC and the true particle identitiy in MC is also shown. Ater the PID selection our sample contains about 88% of muons (red histogram). After the PID selection our sample contains about 92% of muons. The 6.4% contamination after the PID cut is given by pions. The contributions from electrons and positive muons travelling backwards and that of protons are less than 1%. They are practically negligible.

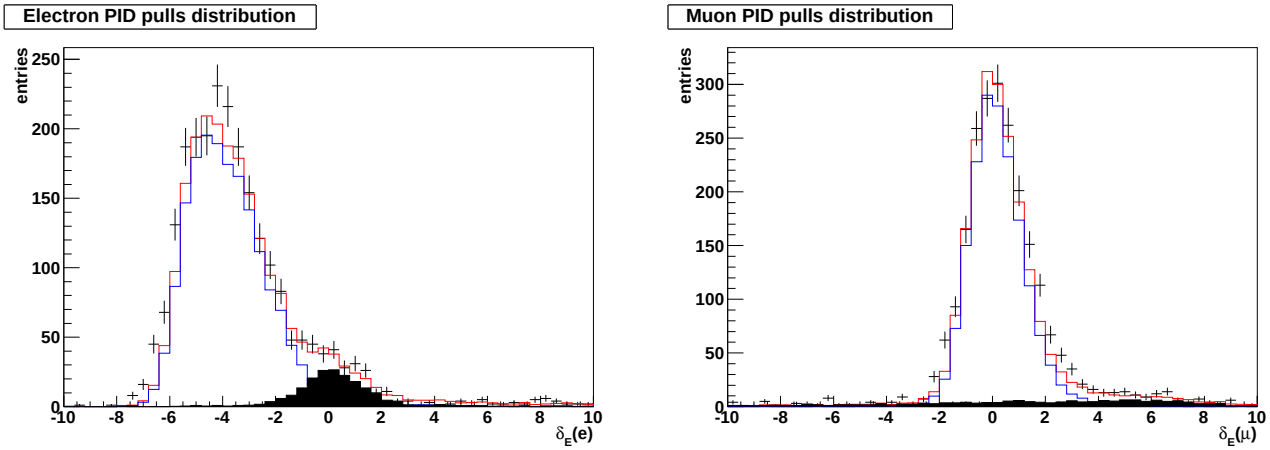

Fig. 5.2 PID pulls in the electron (left) and muon (right) hypothesis. Black marker shows data, red histogram shows MC, blue histogram shows MC muons and black filled histogram shows MC electrons. MC is normalized basing on POT.

5.5.2 Data and Monte-Carlo Comparison

The distributions of the reconstructed muon momentum and the cosine of the muon polar angle are shown for data and MC in Fig. 5.3. The MC probides a good description of the data both in terms of normalization and shape of these distributions. The number of events expected according to the NEUT MC is 1651.4 while 1816 candidates are found in the data. The final sample in the Monte Carlo has

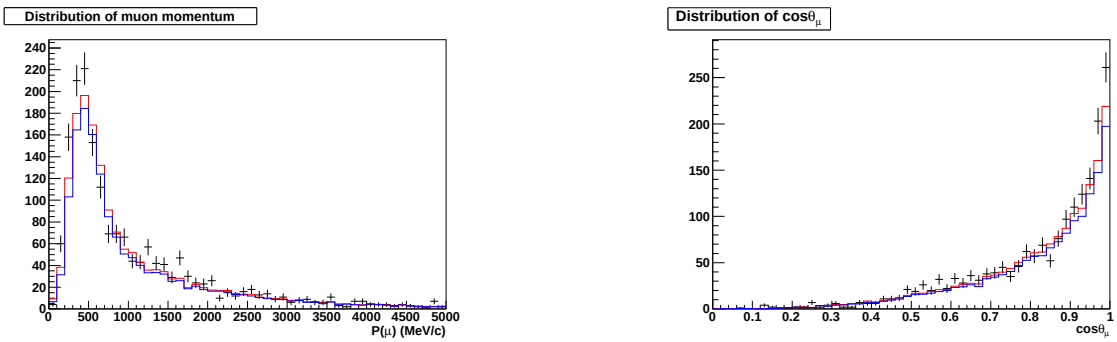

Fig. 5.3 Distribution of the muon momentum (Left) and of the muon $\cos\theta_\mu$ (Right) for the selected events are shown. Black marker shows data, red histogram shows MC and blue histogram shows MC true muons. MC histograms are normalized with POT.

been classified into seven different categories corresponding to different types of interaction (CCQE, CC resonance, CC DIS, NC, coherent π production), neutrino flavour ($\bar{\nu}_\mu$ or the position of the vertex in the detector ("Outside FGD"). The break down of the sample in these categories is giben in Tab[5.3] .

This selection has a reasonably high efficiency, dominated by the feometrical acceptance of the TPC, and that the sample is indeed dominated by CC interactions. Monte Carlo provides a remarkably good description of the kinematical variables both in shape and normalization.

Component	Fraction (%. after PID)
CCQE	55.0%
CC resonance	21.6%
CC coherent	3.2%
CC DIS	7.5%
NC	3.0%
$\bar{\nu}_\mu$	0.5%
Outside FGD	6.3%

Table. 5.3 True interaction types after PID selection (NEUT).

5.6 FGD - SMRD analysis

In this section, we describe the measurement of T2K ν_μ beam with tracks starting in FGD and injecting to SMRD. Here, FGD1 and FGD2 are used as active target detector and SMRD are used to provide the track momentum.

5.6.1 Selection for Muons in FGD - SMRD Tracks

The basic idea of the selection for FGD - SMRD is same as that for FGD - TPC tracks, to extract μ tracks with highest momentum in the event. We consider the tracks going through 4.8 cm iron of SMRD as the muons, ideally.

5.6.1.1 Event Bunching, TPC VETO and FGD FV Selection

At first, the same cuts as FGD - TPC analysis are applied to tracks, event bunching and upstream TPC veto. We search tracks starting in FGD1 fiducial volume with TPC1 veto, and then FGD2 FV with TPC2 veto in case there's no tracks with SMRD constituents in FGD1. Here, we don't request TPC hits but SMRD hits for the tracks. The end position of reconstructed tracks requested to be out of SMRD inner yoke. ($|X| > 1836.0$mm, $|Y| > 2024.5$mm)

5.6.1.2 Highest Momentum Tracks Selection

For extracting most energetic tracks, we select the track with the most SMRD hits in X or Y layers among the all tracks. At same time, we discarded events with tracks which have hits in outermost layer of SMRD to reject tracks with unmeasurable momentum with SMRD, cosmic muon backgrounds and muons from sand or wall around ND280 pits.

5.6.2 Energy Reconstruction with SMRD

The kinematic energy of tracks are evaluated with the sum of energy loss in the FGD and SMRD. The energy loss in SMRD is obtained with approximation:

$$dE_{SMRD} = 13.05 \times x + 54.68 - 32.60 \times \exp\left(-0.5948 \times x\right) \tag{5.2}$$

The track length in SMRD x is calculated with SMRD outermost hit position and reconstructed particle direction at end point of tracks. This approximation was given by 2 component fittng of Bethe-Bloch equation, with iron absorber and muon injection.

5.6.3 Data-Monte Carlo Comparison

The distributions of the reconstructed kinematic energy and the cosinus of the polar angle are shown for data and MC in Fig.5.4. The simulation probides a good description of the data both in terms of

normalization and shape of these distributions. Data gives 973 events for all SMRD tracks, and MC expects 873.61 for them. Data/MC is 1.11 for these select conditions. The number of TPC hits <= 18 tracks gives us tracks selection exclusive of tracks FGD-TPC analysis. In condition of TPC hits <=18, data gives 461 events for all SMRD tracks, and MC expects 395.03. Data/MC is 1.16 for these select conditions. The data/MC value is consistent with not-reweighted data/MC of FGD-TPC selection.

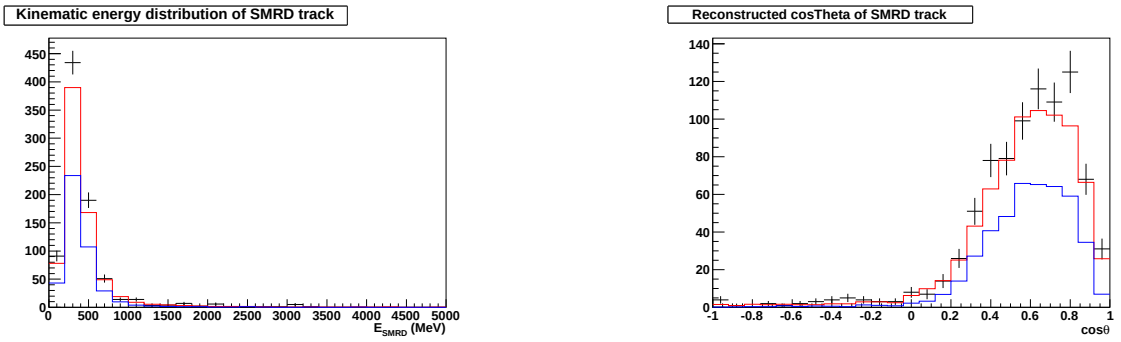

Fig. 5.4 Distribution of the reconstructed kinemtic energy (Left) and of the $\cos\theta_\mu$ (Right) for the selected tracks are shown. Black marker shows data, red histogram shows MC and blue histogram shows MC true muons. Black line shows true kinematic energy of MC ture muons.

5.7 Reweighting with Tuned Flux

The Monte Carlo used in the analysis is based on the flux release 11a. In order to test the effect of using a more recente flux release (11-tuned-v1), the simulated interactions are reweighted on an event-by-event basis with a correction which depends on the true neutrino energy.

The distribution of the muon momentum before and after the reweighteing is shown in Fig. 5.5. The reweighted Monte Carlo number of events is 6% higher than the not reweighted one leading to the data/MC ratio after the flux reweighting:

$$R_{data/NEUTMC,reweighted} = 1.033 \pm 0.023(stat.)^{+0.044}_{-0.037}(det.sys.) \pm 0.038(phys.model). \quad (5.3)$$

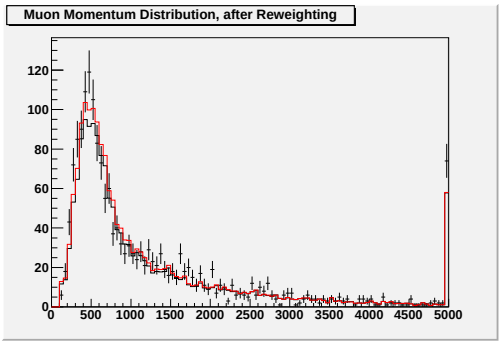

Fig. 5.5 Distribution of the muon momentum before (black histogram) and after (red histogram) flux reweighting. Black plotted histogram shows data.

5.8 Summary of ν_μ Measurement at J-PARC

An analysis of nd280 near detector data is described in this section. Two kind of track selections, FGD-TPC and FGD-SMRD are applied to 2010a, Run I data set. FGD-TPC selection gives 1816 and 1651.4

events for data and MC, respectively. The data/MC is calculated as 1.10 for not reweighted FGD-TPC selection. FGD-SMRD selection gives 973 and 873.61 events for data and MC, respectively. With additional selection for FGD-SMRD analysis, which is exclusive to FGD-TPC selection, FGD-SMRD selection gives 461 and 395.03 events. Data/MC is 1.11 for all of FGD-SMRD and 1.16 for exclusive condition. These values are consisntent in these errors.

Data/MC value of FGD-TPC selection is reweighted with 11a-tuned-v1 flux for following oscillation analysis with SK measurement. The final input from near detector is:

$$R_{data/NEUTMC,reweighted} = 1.033 \pm 0.023(stat.)^{+0.044}_{-0.037}(det.sys.) \pm 0.038(phys.model). \quad (5.4)$$

Chapter 6

Measurement of Neutrino Beam at Kamioka

6.1 Outline

Neutrinos produced by the accelerator at J-PARC propagate through the 295 km of the Earth and and then are detected by the Super-Kamiokande (SK) far detector. Here, we measure the amount and the energy of ν_μ beam events at SK. The analysis strategy is to select CCQE events induced by T2K ν_μ beam and to measure P_μ and θ_μ to reconstruct the energy of ν_μ after 295 km propagation. To select CCQE events, we apply a selection called Fully Contained (FC) Fiducial Volume (FV) 1-Ring μ-like. Additionally, we request $P_\mu \geq 200$MeV/c and the number of decay electrons ≤ 1. The amount and the reconstructed energy of selected FCFV 1-Ring μ-like events are provided for ν_μ disappearance analysis.

6.2 Dataset

We use the beam spills suitable to make the SK analysis within Run I+II datasets, which were recorded Jan. 2010 to Mar.2011. The following cuts are applied to extract the SK good spills: (1) SK DAQ alive, (2) Bad subrun cut, (3) DAQ/GPS error cut, (4) Special data block cut and (5) Pre-activity cut[81]. After these cuts, we acquire datasets corresponds to 1.431×10^{20} accumulated protons on target (POT) during these periods.(Fig. 6.1)

The Monte Calro (MC) simulated events are generated using the beam flux simulation and reweight-generateded with fine-tuned flux. Interactions within the SK volume are generated by the NEUT v5.06 interaction generator and are simulated using the GETANT3-based SKDETSIM v11.79. Both MC and data are reconstructed using the Super-K apfit10a libraries. Unless otherwise noted, plots in this section have been normalized to the above beam time by using POT.

6.3 Selection Criteria for Neutrino Events at Super-Kamiokande

The Super-Kamiokande detector is operated in self-trigger mode by itself and all of the "hit" signals are continuously collected by the online PCs. Information on the absolute timing of each T2K beam spill, which is measured by using the GPS system at J-PARC, is sent to the SK DAQ system spill by spill. We store all the hit information within $\pm 500\mu$sec from the beam arrival time at SK by taking a neutrino time-of-flight (TOF, 295.336 km/c = 985.134 msec) into account. This DAQ system enables us to record all the detector activities induced by T2K beam neutrinos.

6.4 Fully Contained Fiducial Volume Selection

Events used in this analysis are selected as subsets of the T2K Fully Contained (FC) Fiducial Volume (FV) samples at SK. The FCFV sample is defined by a set of cuts standard to the Super-K atmospheric analysis[81]. The selection criteria of FC sample are as follows:

- The events are observed within 12μsec of expected T2K spill timing (-2μsec$\sim$+10μsec).

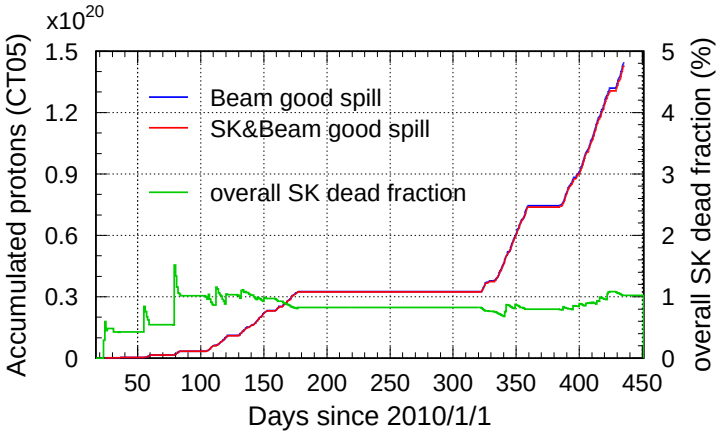

Fig. 6.1 The blue line shows the number of accumulated protons (see the left-hand vertical axis) as a function of date by using all the "beam good" spills. The red line shows the number of accumulated protons by using the "SK good" spills among the beam good spills. The number of protons is measured at CT5. The red line is almost overlapping with the blue line. The number of accumulated protons at the end of Run II is 1.446×10^{20} for the beam good spills and 1.431×10^{20} for the SK&beam good spills. The green line shows the variation of the overall SK dead fraction, i.e. (blue-red)/blue (see the right-hand vertical axis). The SK livetime fraction to the beam good spills is about 99%.

- Removing "flashing PMT" events (FLASHER) are applied.
- Visible energy (E_{vis}) is greater than 30 MeV.
- All visible particles are inside the Inner Detector(ID). The number of hit PMTs in largest OD cluster <= 16.

In addition to these criteria, a fiducial volume cut is required for FV events (Fig. 6.2):

- Reconstructed vertex is inside the fiducial volume. Distance from nearest ID wall > 200cm.

6.5 FCFV 1-Ring μ-like Selection

For ν_μ disappearance analyses, we require further cuts:

- Number of rings is one.
- Particle ID is muon-like (μ-like).
- Number of decay electrons is equal or less than one.
- Reconstructed muon momentum is greater than 200MeV/c.

Figure 6.3 shows the number of ring distribution of FCFV, and particle ID results for FCFV single-ring events. Figure 6.4 shows the number of decay electrons for FCFV single-ring μ-like events, and reconstructed momentum for the sample after applying cuts (1)-(6). Figure 6.5 shows the reconstructed muon momentum and cosine of the angle of muon direction with respect to the neutrino beam direction. Figure 6.6 shows the reconstructed neutrino energy.

Finally, 31 FCFV single-ring μ-like events are found in Super-Kamiokande Run I+II dataset with 1.431×10^{20} POT.

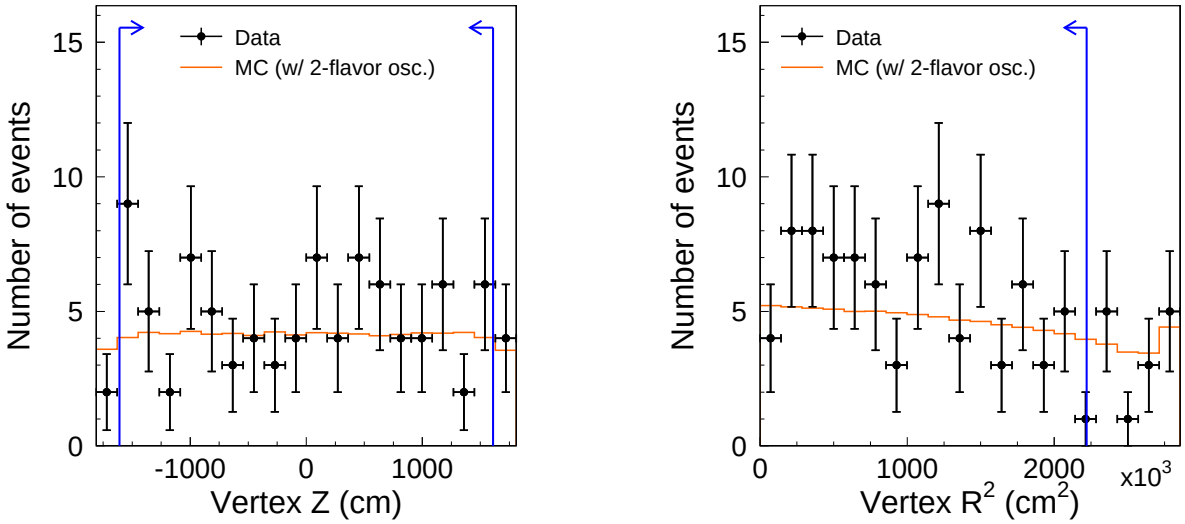

Fig. 6.2 The vertex Z (i.e. the height of the vertex) distribution for the FC events with visible energy >30MeV and vertex R<1490cm (left) and the vertex R^2 (i.e. the square of the distance from the vertex to the vertical central axis of the SK tank) distribution for the FC events with visible energy >30MeV and vertex |Z|<1610cm (right) are shown. The blue arrows show the fiducial volume cut, |Z|<1610cm and R<1490cm, respectively.

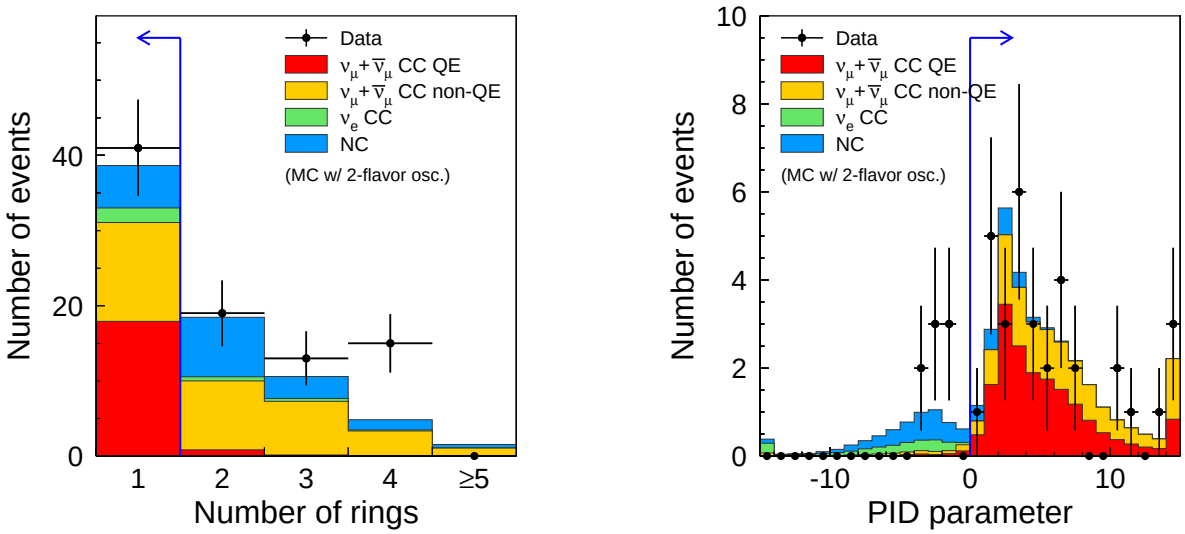

Fig. 6.3 The number of rings for the FCFV events (left) and the particle ID parameter distribution of the FCFV single-ring events (right) in the Run I+II data. The blue arrow shows one of the event selection criteria for the numu disappearance analysis, Nring=1(left) and μ-like (right). The MC distribution is normalized to the observed data by using POT. Two-flavor neutrino oscillations with $sin^2 2\theta_{23} = 1.0$ and $\Delta m^2_{23} = 0.0024(eV^2)$ are included in the MC distribution.

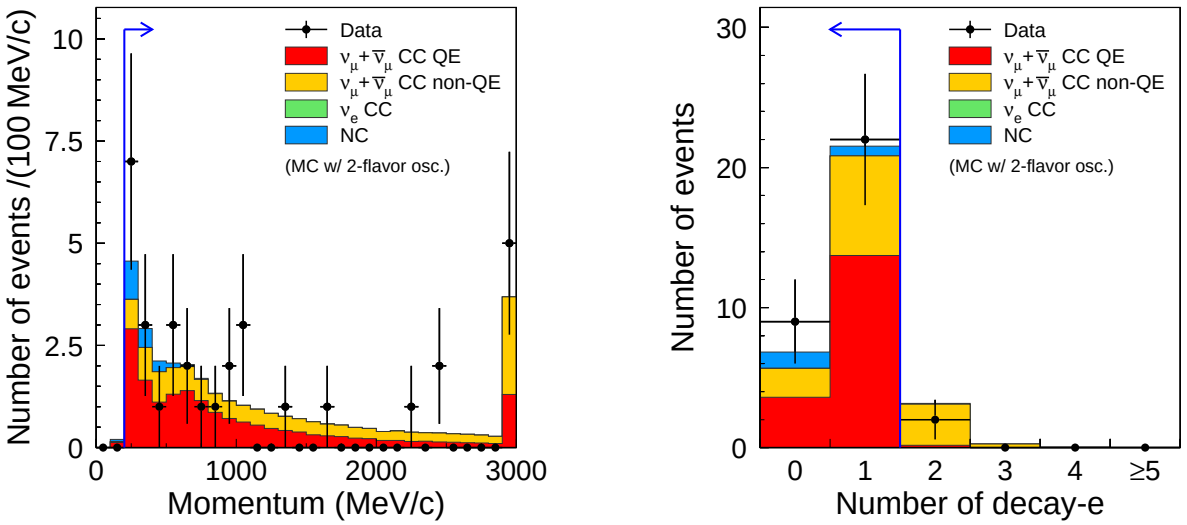

Fig. 6.4 The reconstructed muon momentum distribution (left) and The number of delayed electron signals distribution (right) of the FCFV single-ring mu-like events in the Run I+II data. The blue arrow shows one of the event selection criteria for the numu disappearance analysis, $P_\mu > 200$MeV/c (left) and the number of delayed electron signals <=1.

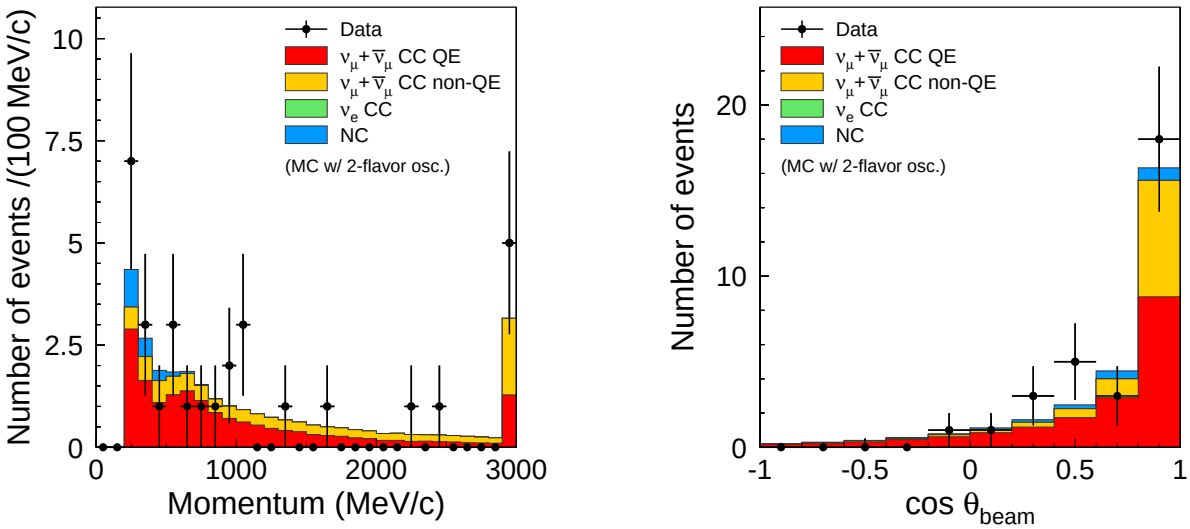

Fig. 6.5 The reconstructed muon momentum distribution (left) and the directional distribution (right) for the final numu events in the Run I+II data, where θ_{beam} is an opening angle between the reconstructed muon direction and the beam direction.

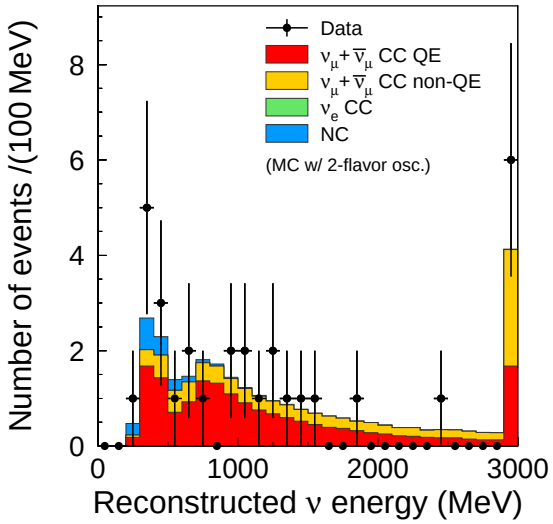

Fig. 6.6 The reconstructed neutrino energy (Enurec) distribution for the final numu events in the Run I+II data. The neutrino energy is reconstructed by using muon momentum and direction with an assumption of CCQE interaction kinematics ignoring Fermi motion.

Event Sample	MC(null osc.)	MC (with osc.)	Data
FCFV	165.3	73.9	88
Single-ring	120.1	38.6	41
μ-like	111.6	31.9	33
$P_\mu > 200$MeV/c	111.0	31.7	33
N(decay-e)≤ 1	103.3	28.3	31
ν_μ analysis sample	103.3	28.3	31

Table. 6.1 The number of selected events at each step for the numu disappearance analysis (Run I+II data). The MC corresponds to 1.431×10^{20} POT and where oscillations have been considered, two flavor transitions $\nu_\mu \leftrightarrow \nu_\tau$ at $\Delta m^2 = 2.4\times10^{-3}\mathrm{eV}^2$ and $\sin^2 2\theta = 1.0$ have been assumed. Descriptions of the cuts used to select event samples re described in the text. A correction factor 1.033 from ND280 observation is multiplied to the MC expectation.

Sample	Total	ν_μCCQE	ν_μCCnQE	ν_e CC	NC
FCFV(null osc.)	165.3	88.6	55.3	3.0	18.2
FCFV(osc.)	73.9	18.9	33.7	3.0	18.2
ν_μ analysis sample (null osc.)	103.3	84.3	17.2	<0.1	1.8
ν_μ analysis sample (osc.)	28.3	17.2	9.2	<0.1	1.8

Table. 6.2 Breakdown of the MC events in Table 6.1.

Chapter 7

ν_μ Disappearance Analysis

In, this chapter, we describe about the method of the ν_μ disappearance analysis and the result with 1.431×10^{20} POT in SK. Maximum likelihood method is employed to get the allowed interval of the neutrino oscillation parameters.

7.1 Analysis method

The ν_μ disappearance analysis is carried out by comparing the observed data and the expectation assuming $\nu_\mu \to \nu_\tau$ neutrino oscillation. To obtain a allowed region of the neutrino oscillation parameter, we employed a maximum likelihood method. In ν_μ disappearance analysis, we use FCFV 1-R μ-like sample which is a ν_μ CCQE enriched sample. The definition of the likelihood is written in Eq. 7.1:

$$L(\sin^2 2\theta, \Delta m^2, \vec{f}) = L_{norm}(\sin^2 2\theta 2, \Delta m^2 2, \vec{f}) \times L_{shape}(\sin^2 2\theta 2, \Delta m^2 2, \vec{f}) \times L_{syst.}(\vec{f}) \quad (7.1)$$

where, L_{norm} is the likelihood for observed number of events,L_{shape} is the likelihood for the shape of the reconstructed neutrino energy spectrum, L_{sys} is the likelihood for systematic error terms, respectively. The information of the observed number of events and shape of the neutrino energy spectrum are separately included in the likelihood.

The term $\vec{f} =^t (f_{\vec{flux}}, f_{\vec{Xsec}}, f_{\vec{\rm SK}}, f_{\vec{\rm ND}})$ is parameter representing systematic errors. The term f is optimized to get maximum of L for each ($\sin^2 2\theta$,Δm^2,$\vec{f}$). We employ a MINUIT2 package to optimize (fit) the f. We do the grid search in ($\sin^2 2\theta$,Δm^2) parameter space to find the maximum of L, and estimate the allowed region of the neutrino oscillation parameters. The likelihood for observed number of events, we assume Poisson probability:

$$L_{norm} = Po(N^{\rm SK}_{\rm exp}, N^{\rm SK}_{\rm obs}) = \frac{\exp(-N^{\rm SK}_{\rm exp}) \cdot (N^{\rm SK}_{\rm exp})^{N^{\rm SK}_{\rm obs}}}{N^{\rm SK}_{\rm obs}} \quad (7.2)$$

where $N^{\rm SK}_{\rm exp}$ and $N^{\rm SK}_{\rm obs}$ are the expected and observed number of FCFV 1R μ-like events, respectively.

The likelihood for spectrum shape, we define as a product of the PDF of each events"

$$L_{shape} = \prod_{i=1}^{N^{\rm SK}_{\rm obs}} \rho(E^{rec}_i; \sin^2 2\theta; \Delta m^2; \vec{f}) \quad (7.3)$$

where $\rho(E^{rec}_i; \sin^2 2\theta; \Delta m^2; \vec{f})$ is a probability density function of the reconstructed neutrino energy spectrum for given ($\sin^2 2\theta$,Δm^2).

The likelihood for systematic error terms, we assume multi-dimensional gaussian distribution:

$$L_{sys} = \frac{1}{\sqrt{(2\pi)^{nsys} \cdot |M|}} \cdot \exp(-\frac{1}{2}^t \vec{\Delta f} M^{-1} \vec{\Delta f}) \quad (7.4)$$

where, $\vec{\Delta f}$ is the difference of $\vec{f}$ from nominal value (set to 1 for all f), and M is the error matrix, nsys is the dimension of $\vec{f}$.

7.2 Calculation method of PDF and $N_{\rm exp}^{\rm SK}$

In the oscillation analysis program, we calculate PDF and $N_{\rm exp}^{\rm SK}$ for given ($\sin^2 2\theta$,Δm^2) and systematic error terms $\vec{f}$. These quantities are calculated based on the histograms of reconstructed neutrino energy distribution, N_i^{rec}. We calculate the histogram of reconstructed neutrino energy distribution from 0.0 GeV to 10.0 GeV with 50 MeV interval. We consider the contribution from ν_μ,$\bar{\nu}_\mu$, and ν_e:

$$\begin{aligned} &N_i^{rec}(\sin^2 2\theta, \Delta m^2, \vec{f}) = \\ &N_i^{rec,\nu_\mu}(\sin^2 2\theta, \Delta m^2, \vec{f}) + N_i^{rec,\bar{\nu}_\mu}(\sin^2 2\theta, \Delta m^2, \vec{f}) + N_i^{rec,\nu_e}(\sin^2 2\theta, \Delta m^2, \vec{f}) \end{aligned} \tag{7.5}$$

The $N_i^{rec}(\sin^2 2\theta, \Delta m^2, \vec{f})$ is calculated by true neutrino distribution by Eq. 7.6:

$$\begin{aligned} N_i^{rec,\nu_X}(\sin^2 2\theta, \Delta m^2, \vec{f}) = &\sum_I F^{FSI}(E_i^{rec}, f^{\vec{FSI}}) \cdot F_I^{\rm SK}\left((f^{\vec{\rm SK}})\right) \times \\ &\sum_j M_{,j}^{\nu_X,I} \cdot F_I^{Xsec}(E_j^{true}, f^{\vec{Flux}}) \cdot N_j^{true,\nu_X,I} \times \\ &P_{osc}\left(E_j^{true}, \sin^2 2\theta, \Delta m^2\right) \end{aligned} \tag{7.6}$$

where,

- N_i^{rec} : Number of events in i-th bin of reconstructed neutrino energy distribution.
- $N_j^{ture,\nu_X,I}$: Number of events in j-th bin of true neutrino energy distribution.
- $M_{ij}^{\nu_X,I}$: Conversion matrix from true neutrino energy distribution to reconstructed energy distribution.
- $P_{osc}\left(E_j^{true}; \sin^2 2\theta, \Delta m^2\right)$: Neutrino oscillation probability
- F^{FSI} : A factor representing the effect of the systematic errors of Final State Interaction of pions.
- $F_I^{\rm SK}$: A factor representing the effect of the systematic errors of event selection efficiency in SK.
- $F_I^{X_{sec}}$: A factor representing the effect of the systematic errors of neutrino cross sections.
- F_{shape}^{Flux} : A factor representing the effect of uncertainty of the spectrum shape of calculated neutrino flux.

Summation of index I runs over neutrino interaction mode (CCQE, CC1π, CC others, NC). The F's are factors representing the effect of the systematic errors:

$$F^{FSI}(E_i^{rec}, f^{FSI}) = 1 + \sigma^{FSI}(E_i^{rec}) \cdot \left(f^{FSI} - 1\right) \tag{7.7}$$

$$F_I^{\rm SK}(f^{\vec{FSI}}) = 1 + \sigma^{{\rm SK}_I} \cdot \left(f_I^{\rm SK} - 1\right) \tag{7.8}$$

$$F_I^{X_{sec}}(E_j^{true}, f^{\vec{X}_{sec}}) = 1 + \sigma^{{\rm SK}_I} \cdot \sigma_I^{X_{sec}}(E_j^{true}) \cdot (f_I^{X_{sec}} - 1) \tag{7.9}$$

where, index I represents the interaction modes, and σ is the estimated systematic uncertainty of each parameter. THe energy dependence of the uncertainty is taken into account in $\sigma(E)$.

The index I in $F^{\rm SK}$ runs over (CCQE, CCnQE, NC), and CC1π production and CC others are treated as CCnQE. For ν_e, I runs over (CC, NC), and CC ν_e interactions are treated by one parameter. For CC ν_e interaction, $F^{X_{sec}}$ has additional factor representing an uncertainty of (CCν_e /CCν_μ) cross section ratio:

$$F_I^{X_{sec}}(E_j^{true}, f^{\vec{X}_{sec}}) = (1 + \sigma_I^{X_{sec}}(E_j^{rec}) \cdot (f^{X_{sec}} - 1))(1 + \sigma_{\nu_e/\nu_\mu}^{X_{sec}} \cdot (f_{\nu_e/\nu_\mu}^{X_{sec}} - 1)) \tag{7.10}$$

The uncertainty of the shape of the calculated neutrino spectrum are treated by 19 parameters. We divide neutrino energy range (0 to 10 GeV) into 19 intervals, and assign 19 parameters. F^{Flux} is written as:

$$F^{Flux}\left(E_j^{true}, f^{\vec{Flux}}\right) = f_k^{Flux} \tag{7.11}$$

where k is the bin number corresponding to E_j^{true}. The size of the uncertainty and the correlation of f_k^{FLux} are estimated and given by error matrix.

The list of the systematic error parameters and the estimated size of their uncertainty are shown in Table. 7.1.

7.2.1 Calculation of PDF

The probability density function (PDF) of the reconstructed neutrino energy spectrum, $\rho(E^{rec})$, is calculated by a linear interpolation of N_i^{rec}:

$$\rho(E^{rec}) = \frac{x \cdot N_i^{rec} + (1-x) \cdot N_i^{rec}}{\sum_i N_i^{rec}} \tag{7.12}$$

where

$$x = \frac{E^{rec} - E_i^{rec}}{E_{i+1}^{rec} - E_i^{rec}} \tag{7.13}$$

and the bin number i is satisfying the condition that $E_{i+1}^{rec} > E^{rec} > E_i^{rec}$.

7.2.2 Calculation of $N_{\rm exp}^{\rm SK}$

The expected number of events, $N_{\rm exp}^{\rm SK}$, is calculated by the equation below:

$$N_{\rm exp}^{\rm SK} = F^{\rm ND} \cdot F_{SK/ND}^{Flux} \cdot \frac{N_{\rm obs}^{ND}}{N_{MC}^{ND}(f^{\vec{X}_{sec}})} \cdot N_{MC}^{SK}(\sin^2 2\theta, \Delta {\rm m}^2, \vec{f}) \tag{7.14}$$

where,

- $N_{\rm obs}^{\rm ND}$: Observed number of events of single track sample in ND280 off-axis detector
- $N_{MC}^{\rm ND}$: MC expectation of single track sample in ND280 off-axis detector
- $N_{MC}^{\rm SK}$: MC expectation of FCFV 1R μ-like events in SK
- $F^{\rm ND}$: A factor representing the effect of the systematic errors in ND280 single-track sample.
- $F_{SK/ND}^{Flux}$: A factor representing the systematic uncertainty of the ratio of SK event and ND events from calculated neutrino flux uncertainty.

$N_{MC}^{\rm SK}$ is calculated by summing N_i^{rec}:

$$N_{MC}^{\rm SK}(\sin^2 2\theta, \Delta {\rm m}^2, \vec{f}) = \sum_i N_i^{rec}(\sin^2 2\theta, \Delta {\rm m}^2, \vec{f}) \tag{7.15}$$

In this calculation, N_i^{rec} does not include the factor F_{shape}^{Flux} (defined in Eq.[7.11]). The systematic uncertainty of $N_{MC}^{\rm SK}/N_{MC}^{ND}$

μ neutrino flux are represented in $F_{SK/ND}^{Flux}$.

The factor F^{ND} and $F_{SK/ND}^{Flux}$ are written as below:

$$F^{ND}F_{SK/ND}^{Flux}F^{ND}(f^{ND}) = 1 + \sigma^{ND} \cdot (f^{ND} - 1) \tag{7.16}$$

$$F_{SK/ND}^{Flux}(f_{SK/ND}^{Flux}) = 1 + \sigma_{SK/ND}^{Flux} \cdot (f_{SK/ND}^{Flux} - 1) \tag{7.17}$$

Item	Source of the uncertanties	Estimated size of uncertainty
f^{SK}_{CCQE}	Uncertainty of SK efficiency of ν_μ CCQE	7.8%
f^{SK}_{CnCQE}	Uncertainty of SK efficiency of ν_μ CC nonQE	25.5%
f^{SK}_{NC}	Uncertainty of SK efficiency of ν_μ NC	115.1%
$f^{SK}_{CC\nu_e}$	Uncertainty of SK efficiency of ν_μ CC ν_e	100%
$f^{SK}_{E-scale}$	Uncertainty of SK efficiency of ν_μ Energy scale	1%
$f^{X_{sec}}_{CCQE}$	Uncertainty of CCQE cross section	E^{true} dependent error
$f^{X_{sec}}_{CC1\pi}$	Uncertainty of cross section of CC 1π	30%(<2GeV), 25%(>2GeV)
$f^{X_{sec}}_{CCothers}$	Uncertainty of cross section of other CC channels	30%(<2GeV), 20%(>2GeV)
$f^{X_{sec}}_{NC}$	Uncertainty of cross section of NC	36%
$f^{X_{sec}}_{\nu_e/\nu_\mu}$	Uncertainty of cross section ratio of $\nu_e/\nu\mu$	6%
f^{FSI}	Uncertainty of Final state interactions	E^{rec} dependent error%
f^{ND}	Uncertainty of ND280 normalization	5%
$f^{Flux}_{SK/ND}$	Uncertainty of SK/ND normalization	E^{true} dependent error%
f^{Flux}_{shape}	Uncertainty of neutrino flux shape	E^{true} dependent error%

Table. 7.1 Table of the parameters representing the systematic errors.

$N^{ND}_{MC}(f^{\vec{X_{sec}}})$ is calculated by summing the neutrino energy distribution. The procedure is similar as in N^{SK}_{MC} calculation:

$$N^{ND}_{MC}(f^{\vec{X_{sec}}}) = \sum_{\nu_X}\sum_{I}\sum_{j} F^{X_{sec},\nu_X}_{I}(E^{true}, f^{\vec{X_{sec}}}) \cdot N^{true,\nu_X,I}_{j} \tag{7.18}$$

The summation is done over neutrino interaction mode, neutrino species, and true neutrino energy, similarly as N^{SK}_{MC} calculation. The true neutrino energy distribution in this event sample, $N^{true,\nu_X,I}$ is given by ND280 group in advance (shown in Fig. 7.1).

The FSI π systematic uncertainty (F^{FSI}) re not included in the N^{ND}_{MC} calculation, because CC inclusive events sample are used for ND280 events, and they are irrelevant for the pion final state. However since the ND efficiency is affected by the nuclear model due to the limited detector acceptance, this uncertainty is considered in the estimation of ND efficeniy systematics f^{ND}.

The cross section systematic uncertainty are commonly used as those of SK except that the parameter for CC QE shape error. This is because the CC QE shape error represents the uncertainty due to the difference in target material in the low energy region, and must be applied to either SK or ND expectation, but not both.

The list of the systematic erros are summarized in Table. 7.1. We consider 32 systematic errors in total.

7.3 Inputs to neutrino oscillation analysis

This section we described about the inputs from Super-K, Near Detector, neutrino beam calculation, and neutrino interactions.

7.3.1 Input from Super-Kamiokande

In this analysis we used T2K 2010a beam data with 1.431×10^{20} POT.

The selection criteria of the sample used for the ν_μ disappearance analysis are as follows.

- Require the Fully Contained selection. THis is essentially to select neutrino interactions inside the inner detector (ID) of the Super-K. Also, removing "flashing PMT" events (FLASHER) are applied.

Super-K run number	event number	Reconstructed E_ν (GeV)
66690	36903128	0.649
66691	109968531	0.448
66719	44482935	1.269
66776	178987674	0.714
66778	190840452	0.280
66796	90460332	0.577
66831	96851432	1.203
66857	146806151	0.376
67892	112157442	0.382
67922	39957655	2.487
67959	2396708	0.416
68051	71413973	1.480
68056	20955003	1.363
68056	157925298	1.020
68057	122987276	0.995
68058	74768431	1.078
68058	232989657	0.930
68058	276863306	3.514
68077	65859771	3.081
68095	193697663	1.118
68095	224971814	5.230
68097	278480734	0.323
68098	35006764	3.632
68111	14891219	0.363
68120	235729788	4.837
68124	16151599	0.607
68143	144688725	0.494
68202	131338204	1.526
68202	283554324	1.879
68203	5960693	4.272
68207	156169102	0.361

Table. 7.2 Table of the parameters representing the systematic errors.

- Reconstructed vertex is inside the nominal fiducial volume, which is defined as the region 2m inside from the ID boundary.(22.5kton)
- The number of reconstructed Cherenkov ring is 1. (single-ring).
- particle ID of the reconstructed Cherenkov ring is μ-like.
- Reconstructed momentum of the muon is above 200 MeV/c. This is to keep the performance of the PID, and remove the contamination from the decay-electrons from invisible muons.

The summary of the selected events in 2010a data is shown in Table. 7.2. The information of the number of events and the shape of the neutrino spectrum is separately used in the oscillation analysis.

Fig. 7.1 shows the true neutrino energy distribution for each interaction mode and neutrino species for 1.431×10^{20} POT, and Fig. 7.2 shows the conversion matrices from true neutrino energy distribution to reconstructed neutrino energy distributions. These are used in the calculation of PDF and $N_{\rm exp}^{SK}$.

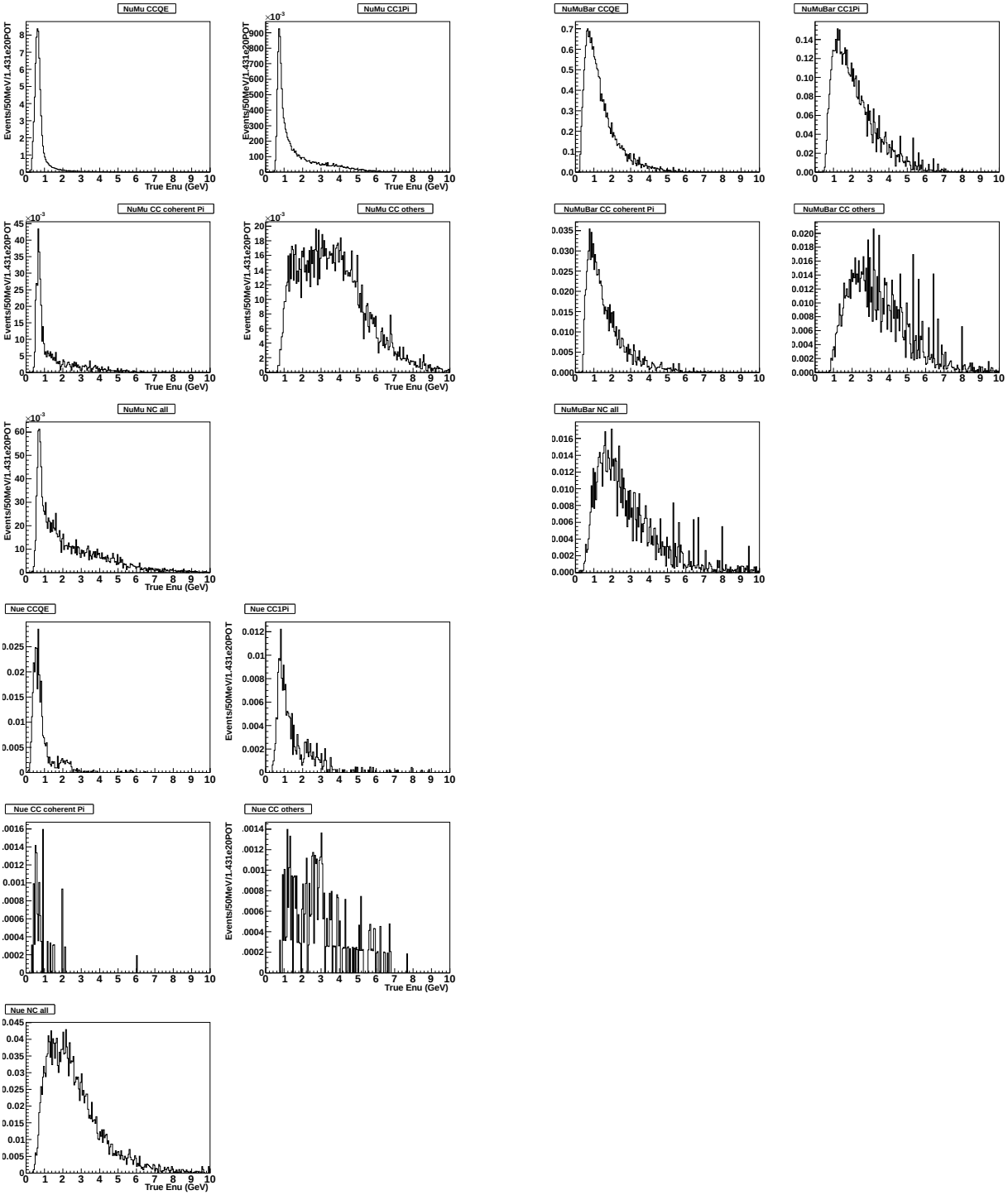

Fig. 7.1 The neutrino energy distributions for each interaction mode and neutrino species, Upper left: ν_μ, Upper right: $\bar{\nu}_\mu$, Lower: ν_e

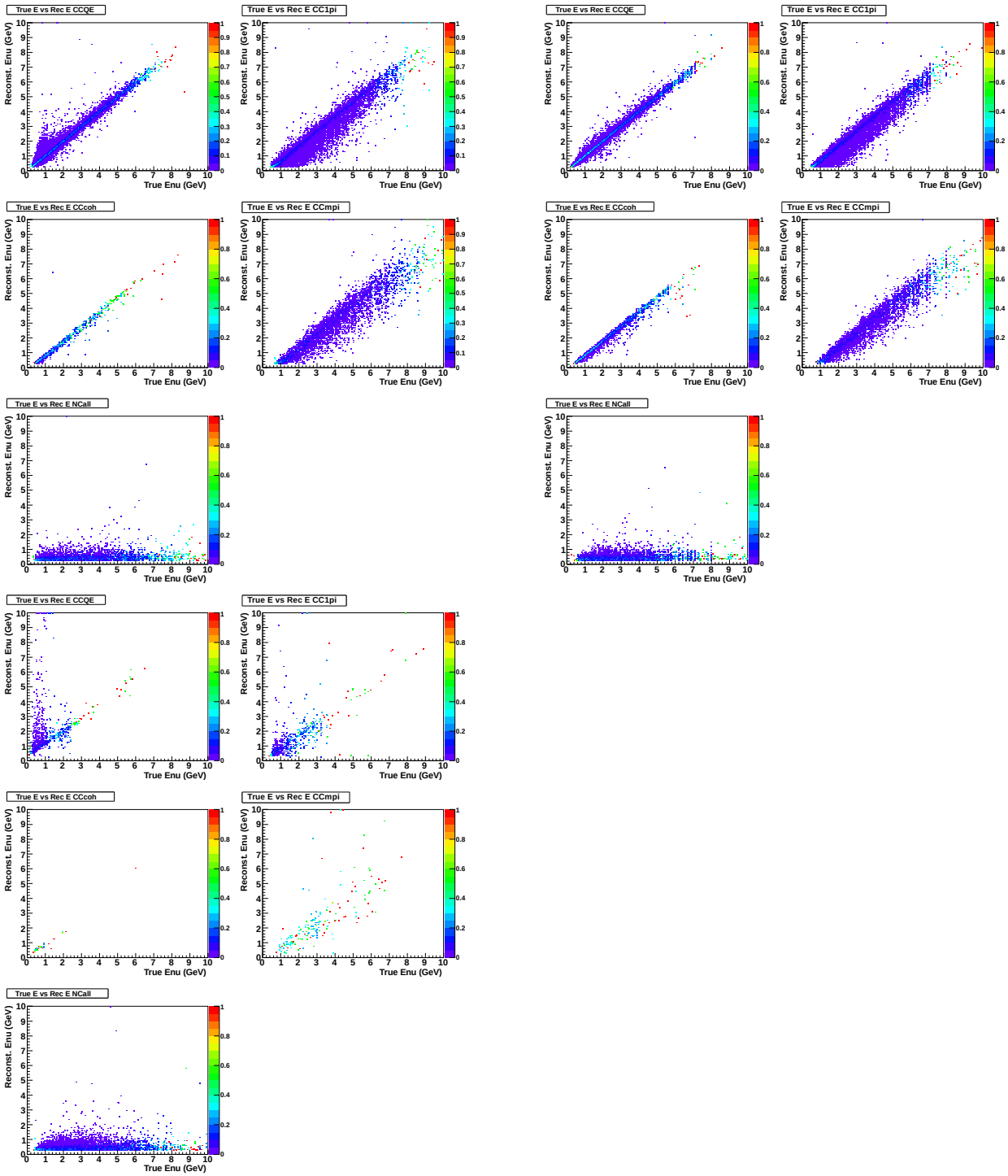

Fig. 7.2 Conversion matrix from true neutrino energy distribution to reconstructed neutrino energy distribution. The matrix are prepared for each interaction mode (CCQE, CC1π, CC coherent π, CC others, NC) and each neutrino flavor (ν_μ, $\bar{\nu}_\mu$, ν_e)

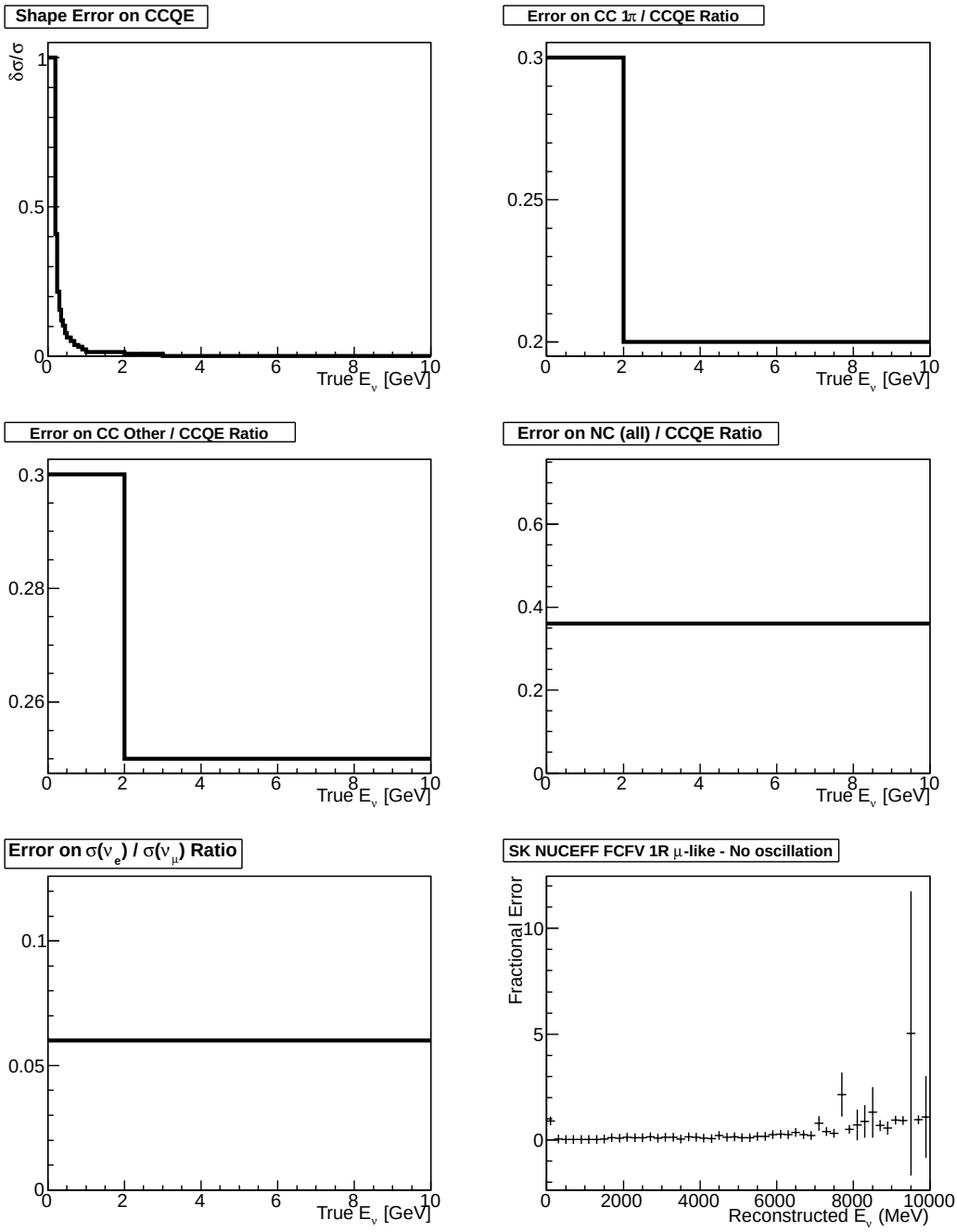

Fig. 7.3 Estimated systematic error of neutrino interactions and FSI.

7.3.2 Input from neutrino interaction working group

The neutrino interaction working group (NIWG) provides the systematic errors related to the neutrino cross section [70], and the final state interactions (FSI) of pion in nuclei[71]. Fig. 7.3 shows the estimated errors as a function of true or reconstructed neutrino energy. The uncertainty of the absolute CCQE cross section is not considered in the ν_μ disappearance analysis. It is because CCQE is the dominant interaction mode in ND280 single-track muon events, and the absolute interaction rate is normalized by the observed number of events in the calculation in Eq. 7.14.

Inputs from ND	Value
Data	1816.0 events
MC (11a tuned v1)	1758.2 events
Data/MC ratio	1.033

Table. 7.3 Inputs from ND280 Off-Axis detector analysis.

Oscillation parameter	N_{exp}^{SK}
Null oscillation	103.7 events
(1.00, 2.4×10^{-3}eV^2)	28.3 events

Table. 7.4 Calculated number of expected events in Super-K for null oscillation case and with neutrino oscillation case.

Uncertainty from the difference of the nuclear target in ND280 and Super-K is included in the CCQE shape error. A large systematic uncertainty is estimated in lowers energy region.

7.3.3 Input from Beam Group

The beam group provided the function to calculate the beam normalization error($\sigma_{SK/ND}^{Flux}$) from the energy spectra at SK and ND[72]. This function calculates the error size on the ratio between the number of SK and ND events, (N_{MC}^{SK}/N_{MC}^{ND}), which includes every uncertainty related to the neutrino beam production and the propagation from near to far detector. Also, the correlation of the shape error terms are provided by the beam group. The range from 0.0 GeV to 10.0 GeV are separated in to 19 intervals, and the size of the systematic uncertainty and the correlation of these 19 bins are estimated. This is included in the error matrix discussed in Eq.7.4.

7.3.4 Input from Near Detector

The measurement of the single-track muon events in the ND280 off-axis near detector are used for normalization of the Super-K expectation. The observed number of events and MC expectation are shown in Table. 7.3.

As described , we use the true neutrino energy distribution of MC events after selection. The histograms are prepared by the ND280 group for each neutrino species ($\nu_\mu, \bar{\nu}_\mu, \nu_e$) and interaction modes.

7.4 Calculated N_{SK} and reconstructed neutrino energy distribution

Using the Eq. 7.14, we calculated the expected number of events. Table. 7.4 shows the $N_{\rm exp}^{SK}$ of selected neutrino oscillation parameters. Fig[7.4] shows the calculated $N_{\rm exp}^{SK}$ as a function of ($\sin^2 2\theta$,Δm^2).

Table. 7.5 shows the systematic uncertainty of $N_{\rm exp}^{SK}$ from each systematic errors sources. Fig. 7.5 shows the calculated PDF with changing systematic error parameters. We change the systematic error parameter, f, by $\pm$ 1 and re-calculate the PDF. For Flux shape errors,f_{shape}^{Flux}, we changed $\pm$ 100% in these plots.

7.5 Expected allowed region of neutrino oscillation parameters

We carried out the ν_μ disappearance analysis with toy MC samples. Fig. 7.6 shows the allowed interval of the neutrino oscillation parameters estimated by to MC data sets correspond to 1.431×10^{20} POT. We calculate =log$L$ in ($\sin^2 2\theta$,Δm^2) space with (0.05,0.00025) grid size, and draw a allowed parameter region. The 68%,90%,99% C.L. allowed interval are defined by a conventional way: The line where the

Source of systematic errors	change of N_{exp}^{SK}
f_{CCQE}^{SK}	+4.73%, -4.73%
f_{CnCQE}^{SK}	+8.36%, -8.36%
f_{NC}^{SK}	+7.47%, -7.47%
$f_{CC\nu_3}^{SK}$	+0.05%, -0.05%
$f_{E-scale}^{SK}$	+0.00%, -0.00%
f^{ND}	+5.26%, -4.76%
f_{CCQE}^{Xsec}	+2.53%, 02.53%
$f_{CC1\pi}^{Xsec}$	+0.44%, -0.49%
$f_{CCothers}^{Xsec}$	+4.13%, -3.69%
f_{NC}^{Xsec}	+0.87%, -0.90%
f_{ν_e/ν_μ}^{Xsec}	+0.00%, -0.00%
f^{FSI}	+5.99%, -5.99%
$f_{SK/ND}^{Flux}$	+6.61%, -6.61%
Total	+16.47%, -16.47%

Table. 7.5 Calculated number of expected events in Super-K for null oscillation case and with neutrino oscillation case.

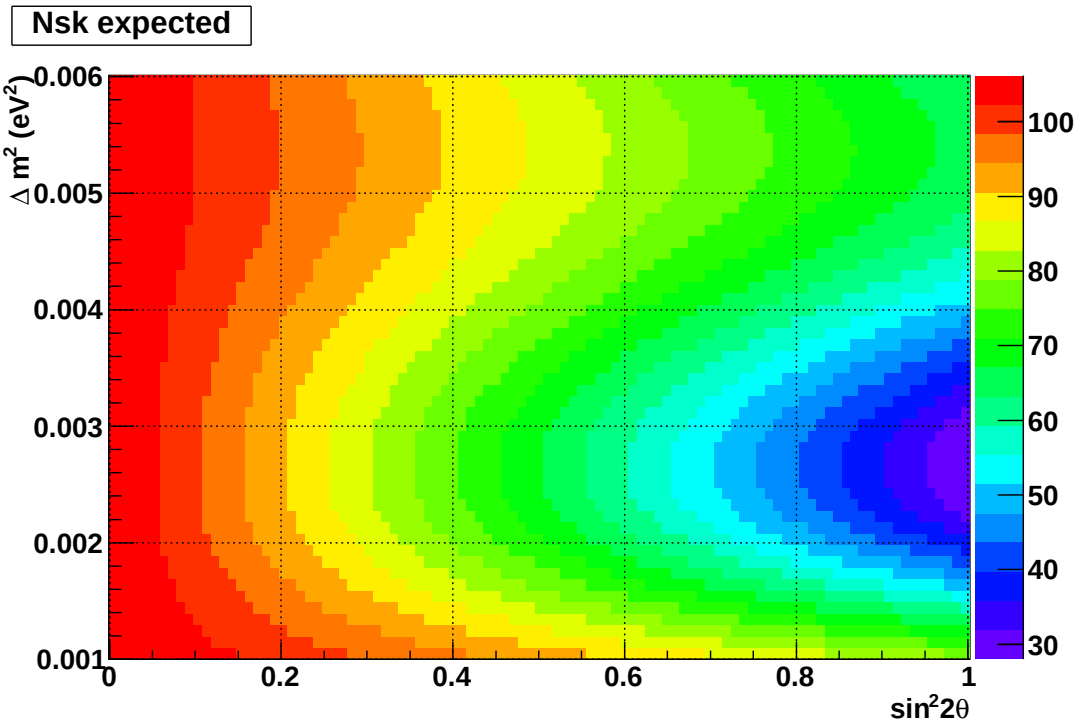

Fig. 7.4 Calculated N_{SK} as a function of oscillation parameters.

difference from the minimum of $-2.0 \times \ln L$ is 2.3,4.6, and 9.2, respectively. We carried out the analysis with 10 set of the to MCs and average the log(L) are shown in the plots. The toy MC are generated with $(\sin^2 2\theta, \Delta m^2) = (1.00, 2.4^{-3} \mathrm{eV}^2)$.

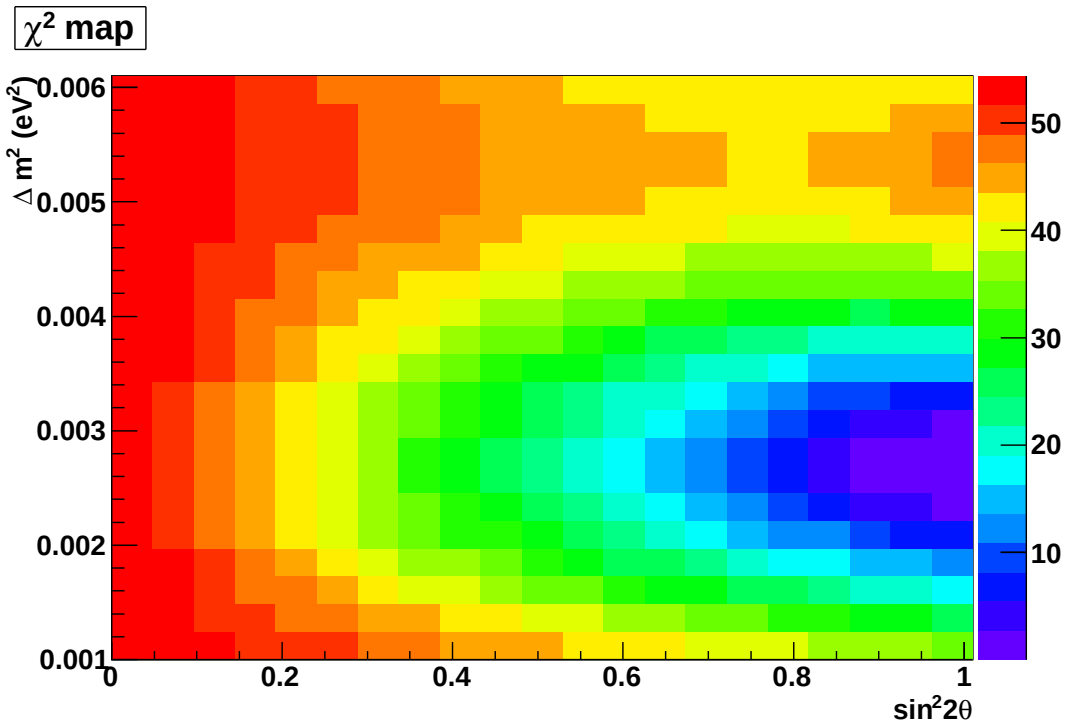

Fig. 7.5 The χ^2 map as a function of neutrino oscillation parameters.

7.6 Analysis Results with T2K 1.431×10^{20} POT data

We apply our analysis tool on the real data shown in sub-section 3.1. Fig. 7.6 shows the obtained allowed region of the neutrino oscillation parameter. We carried out a grid search of the best fit point in this map. We scanned ($\sin^2 2\theta$,Δm^2) map with the binning of (0.05, 0.00025), and with finer binning (0.01, 0.0001) at (0.08-1.00, 0.002-0.003) region. The 68%, 90% and 99% C.L. allowed interval is defined by a conventional way: The line where the difference from the minimum of $-2.0 \times \ln L$ is 2.3, 4.6 and 9.2, respectively. The best fit point is obtained at ($\sin^2 2\theta$,Δm^2) = (0.99, 2.6×10^{-3}eV^2), and the value of $-2.0 \times \ln L$ is 262.902. Fig. 7.7

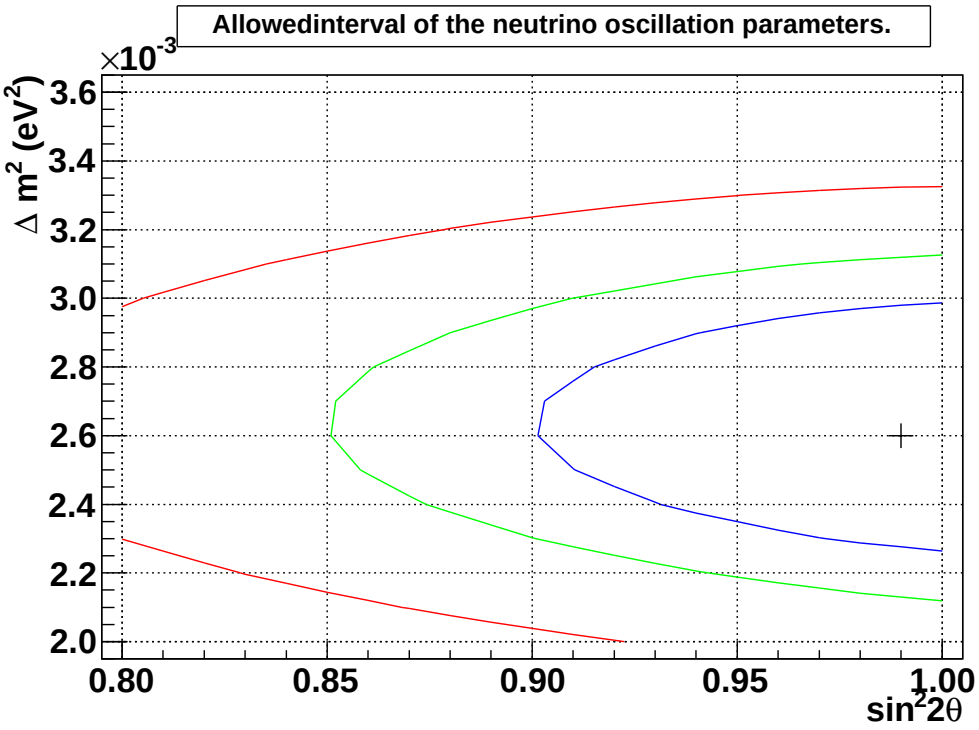

Fig. 7.6 Allowed interval of the neutrino oscillation parameters. 68% C.L. (blue), 90% C.L. (green) and 99% C.L. (red) line are shown. Black point shows the best fit point, $(\sin^2 2\theta, \Delta m^2) = (0.99,\ 2.6 \times 10^{-3}\mathrm{eV}^2)$.

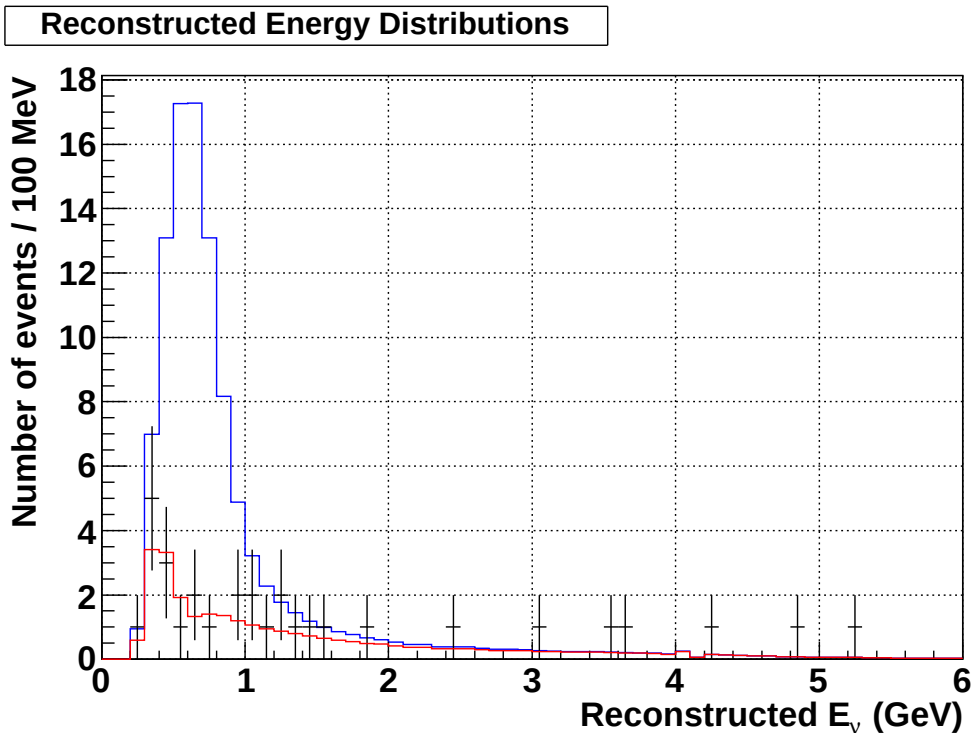

Fig. 7.7 The energy distribution of SK measuement results (black), MC without oscillation (blue) and MC with the best fit point $(\sin^2 2\theta, \Delta m^2) = (0.99,\ 2.6 \times 10^{-3}\mathrm{eV}^2)$ (red). MC is normalized with POT.

Chapter 8

Conclusion

The T2K experiment is a 295 km long-baseline neutrino oscillation experiment in Japan. The goal of T2K are measurement of the neutrino mixing angle θ_{13} and precision measurement of the mixing angle θ_{23} and the mass difference Δm^2_{23}.

The ND280 near detector complex is located 280 m downstream from the beam target in J-PARC (Japan Proton Accelerator Research Complex) for measuring the flux, the energy spectrum and the flavor contents of the initial neutrino beam. We will compare the near detector based predictions with the measured oscillated beam at the far detector, Super-Kamiokande.

The Side Muon Range Detector surrounds the inner detector components of ND280 off-axis detector and is optimized for energy measurement of large angle muons coming from charged-current neutrino interactions in the inner detectors. The construction of SMRD was successfully finished at Jul. 2009. We measured the performance of the counter of SMRD with cosmic rays. The light yield of counter was > 10 p.e. at all measured point, and the position resolution was 6.1 ± 0.8 cm. These performances satisfy the requirements of SMRD.

After the installation, SMRD's function were tested. The cosmic trigger function was tested by acquiring cosmic rays with opened and closed UA1 magnet. Acquired data was classified to 4 patterns and compared with simulation. The ratio of these patterns showed good consistency. We concluded SMRD cosmic trigger function work fine.

The beam trigger function was tested during beam commissioning at Dec. 2010. We find two peak structure corresponding the T2K neutrino beam. This check revealed the beam trigger system worked correctly. Basing on the beam commissioning information, the DAQ of SMRD was configured successfully for T2K physics beam run.

Two kind of nd280 analysis, FGD-TPC and FGD-SMRD are done to 2010a, Run I data set. FGD-TPC selection gives 1816 and 1651.4 events for data and MC, respectively. The data/MC is calculated as 1.10 for not reweighted FGD-TPC selection. FGD-SMRD selection gives 973 and 873.61 events for data and MC, respectively. With additional selection for FGD-SMRD analysis, which is exclusive to FGD-TPC selection, FGD-SMRD selection gives 461 and 395.03 events. Data/MC is 1.11 for all of FGD-SMRD and 1.16 for exclusive condition. These values are consistent in these errors. These value shows FGD-SMRD tracks can contribute future analysis with $\sim$10% more statistics for current FGD-TPC analysis.

Data/MC value of FGD-TPC selection is reweighted with 11a-tuned-v1 flux for following oscillation analysis with SK measurement. The final input from near detector is:

$$R_{data/NEUTMC,reweighted} = 1.033 \pm 0.023(stat.)^{+0.044}_{-0.037}(det.sys.) \pm 0.038(phys.model). \quad (8.1)$$

With these inputs, the SK oscillation analysis gives best fit point at ($\sin^2 2\theta$,Δm^2) = (0.99, 2.6×10^{-3}eV^2). This result is consistent with recent measurement of ($\sin^2 2\theta$,Δm^2).

Biblography

[1] PDG p.555 Vol. 37. 2010
[2] Z. Maki, M. Nakagawa, S. Sakata, Prog. Theor. Phys. 28,870(1962)
[3] M. Kobayashi, T. Masukawa, Prog. Theor. Phys. 49,652 (1973)
[4] H. Gallagher for the MINOS Collaboration arXiv:0809.5240v1 [hep-ex]
[5] Y. Ashie et al. (Super-Kamiokande Collab.) PR D71 112005
[6] Y. Ashie et al. (Super-Kamiokande Collab.) Phys.Rev.Lett.93, 101801,2004.
[7] S. Abe et al. (KamLAND Collab.), Phys. Rev. Lett. 100, 221803 (2008).
[8] C. Arpesella et al., Phys. Rev. Lett. 101, 091302 (2008).
[9] J. Hosaka et al., Phys. Rev. D73, 112001 (2006).
[10] S. Abe et al. (KamLAND Collab.) PRL 101 119904E
[11] B.T.Cleveland et al.,. Astrophys. J. 496 (1998) 505.
[12] Abdurashitov, J. N. et al. (SAGE), Phys. Rev. C80 (2009) 015807.
[13] M. Altmann et al. (GNO) Phys. Lett. B 616 (2005) 174
[14] W. Hampel et al. (GALLEX) Phys. Lett. B 447 (1999) 127.
[15] B. Aharmim et al. (SNO Collab.) PRL 101 111301
[16] M. Apollonio et al. (CHOOZ Collab.) PL B466 (1999) 415.
[17] P. Adamson et al. (MINOS Collab.) PRL 101 131802
[18] P. Adamson et al. (MINOS Collab.) Phys.Rev.Lett.106:181801,2011
[19] N. Agafonova et al. (OPERA Collaboration) Phys.Lett.B691:138-145,2010.
[20] K. Abe et al. (T2K Collaboration) PhysRevLett.107.041801.
[21] Letter of intent: Neutrino oscillation experiment at JHF, Letter of intent: Neutrino oscillation experiment at JHF, 2003. http://neutrino. kek.jp/jhfnu/loi/loi_JHFcor.pdf.
[22] Y. Fukuda, T. Hayakawa, E. Ichihara, M. Ishitsuka, Y. Itow, et al., Nucl.Instrum.Meth. A501 (2003) 418-462.
[23] D. Beavis, A. Carroll, I. Chiang, et al., Long Baseline Neutrino Oscil- lation Experiment at the AGS (Proposal E889), 1995. Physics Design Report, BNL 52459.
[24] J-PARC TDR, KEK-Report 2002-13 and JAERI-Tech 2003-044, http: //hadron.kek.jp/ accelerator/TDA/tdr2003/index2.html, 2003.
[25] T. Nakamoto, et al., IEEE Trans. Appl. Supercond. 14 (2004) 616-619.
[26] T. Nakamoto, et al. (2005). An invited paper presented at the 2005 Par- ticle Accelerator Conference (PAC05), Knoxville, Tennessee, U.S.A., May 16-20, 2005.
[27] T. Ogitsu, et al., IEEE Trans. Appl. Supercond. 15 (2005) 1175-1178.
[28] T. Okamura, et al., Applied Superconductivity, IEEE Transactions on 19 (2009) 1125 -1130.
[29] T. Ogitsu, et al., Applied Superconductivity, IEEE Transactions on 19 (2009) 1081 -1086.
[30] K. Sasaki, et al., Applied Superconductivity, IEEE Transactions on 20 (2010) 242 -245.
[31] T. Nakamoto, et al., Applied Superconductivity, IEEE Transactions on 20 (2010) 208 -213.
[32] Toshiba Electron Tubes and Devices Co.,Ltd, 2008. http://www. toshiba-tetd.co.jp/eng/index.htm.
[33] T. Nakadaira, et al., AIP Conf. Proc. 981 (2008) 290-292.
[34] S. van der Meer (1961). CERN-61-07.
[35] R. B. Palmer (1965). Presented at Informal Conference on Experimen- tal Neutrino Physics, CERN, Geneva, Switzerland, 20-22 Jan 1965 (C. Franzinetti, (Ed.), CERN-65-32, pp. 141-146).
[36] K. Matsuoka, et al., Nucl. Instrum. Meth. A623 (2010) 385-387.

[37] K. Matsuoka, et al., Nucl. Instrum. Meth. A624 (2010) 591-600.
[38] T. Higuchi, H. Fujii, M. Ikeno, Y. Igarashi, E. Inoue, et al. (2003) TUGT004.
[39] H. G. Berns, R. J. Wilkes, FADC board for T2K beam monitors, http: //neutrino.phys.washington.edu/ berns/T2K/ADCCARD/adc2_status.html, http://neutrino.phys.washington.edu/ berns/T2K/ADCCARD/docs/UWFADC-technote.pdf, 2008.
[40] S. Ritt, P. Amaudruz, K. Olchanski, MIDAS (Maximum Integration Data Acquisition System), 2001. http://midas.psi.ch.
[41] D. Renker, E. Lorenz, JINST 4 (2009) P04004.
[42] M. Yokoyama, et al., Nucl. Instrum. Meth. A610 (2009) 128-130.
[43] M. Yokoyama, et al., Nucl. Instrum. Meth. A622 (2010) 567-573. Nucl.Instrum.Meth.A (2011). Preprint: arXiv 1101.1996.
[44] A. Pla-Dalmau, Frascati Phys. Ser. 21 (2001) 513-522.
[45] A. Pla-Dalmau, A. Bross, V. Rykalin, B. Wood, Nuclear Science Sym- posium Conference Record 3 (2005) 1298-1300.
[46] I. Giomataris, et al., Nucl. Instrum. Meth. A560 (2006) 405-408.
[47] N. Abgrall, B. Andrieu, P. Baron, P. Bene, V. Berardi, et al., Nucl. In- strum. Meth. A637 (2011) 25-46.
[48] A. Izmaylov, et al., Nucl. Instrum. Meth. A623 (2010) 382-384.
[49] SMRD Group, The Side Muon Range Detector (SMRD) in the near de- tector complex of the T2K experiment, 2011. In preparation.
[50] L. Bellantoni, P. Rubinov, Bench test of first Trip-T prototypes, 2005. D0 note 4845 https://plone4.fnal.gov/P1/AFEIIUpgrade/ tript/.
[51] A. Vacheret, S. Greenwood, M. Noy, M. Raymond, A. Weber, in: Nu- clear Science Symposium Conference Record, 2007. NSS 寰 Ź07. IEEE, volume 3, pp. 1984-1991.
[52] M. Thorpe, et al., in: Proceedings of the 17th IEEE Real Time Confer- ence. To be published.
[53] T. H. Collaboration, High Performance Storage System (HPSS), 2010. http://hpss- collaboration.org.
[54] I. Bird, (ed.), et al. (2005). CERN-LHCC-2005-024.
[55] M. Shiozawa, et al., Phys.Rev.Lett. 81 (1998) 3319-3323.
[56] Y. Hayato, et al., Phys.Rev.Lett. 83 (1999) 1529-1533.
[57] H. Nishino, et al., Phys.Rev.Lett. 102 (2009) 141801.
[58] Y. Fukuda, et al., Phys.Rev.Lett. 81 (1998) 1562-1567.
[59] Y. Fukuda, et al., Phys.Rev.Lett. 82 (1999) 2430-2434.
[60] M. Ahn, et al., Phys.Rev. D74 (2006) 072003.
[61] Y. Ashie, et al., Phys.Rev. D71 (2005) 112005.
[62] J. Hosaka, et al., Phys.Rev. D74 (2006) 032002.
[63] Y. Itow, et al., The JHF-Kamioka neutrino project, 2001. ArXiv hep- ex/0106019.
[64] H. Nishino, et al., Nuclear Science Symposium Conference Record, 2007. NSS 寰 Ź07. IEEE 1 (2008) 127-132.
[65] S. Yamada, et al., 2009 16th IEEE-NPSS Real Time Conference Poceed- ings (2009) 201-205.
[66] H. Nishino, K. Awai, Y. Hayato, S. Nakayama, K. Okumura, et al., Nucl.Instrum.Meth. A610 (2009) 710-717.
[67] T. Uchida, M. Tanaka, Nuclear Science Symposium Conference Record, 2006. IEEE 3 (2006) 1411-1414.
[68] J. Kameda, and R. Wendell for the SK-LIB and T2K-SK groups, "Study on Super-K events and systematic errors relevant for the ν_μ disappearance analysis with T2K 3.23×10^{19} POT data" T2K-TN-034
[69] J.Albert, H. Kaji, S. Nakayama, S. Mine, and K.Okumura for the SK-LB and T2K-SK groups, "Study on SK ν_e candidates and systematic erros with T2K 3.23×10^{19}POT dta" T2K-TN-028
[70] "NEUT systematic studies for 2010a analysis" T2K-TN-032
[71] "NEUT Nuclear Effect (FSI)" T2K-TN-033

[72] "Beam inputs to the 2010a Oscillation Analysis" T2K-TN-040
[73] Y. Hayato, Acta Physica Polonica B Vol. 40, No. 9 (2009)
[74] K.Sakashita, 22/Apr/2010 T2K collaboration meeting
[75] M. Bass et al, T2K experiment TN-013.
[76] H. Maesaka, Ph.D. thesis, Kyoto University, 2005.
[77] A. Cervera-Villanueva et al., NIM A 534 (2004) 180-183
[78] D. Karlen, et al., NIM A 555 (2005) 80.
[79] T2K Internal note, FGD Reconstruction Overview
[80] T2K Internal note, ND280 Software Reference
[81] T2K Internal Tech note No.27

List of Figures

List of Tables